

A Study of Coherent Synchrotron Radiation: Intensity Enhancement of the Far-IR Spectrum by Exciting Single Bunch Instabilities

Yaw-Ren Eugene Tan
BSc (Hons)



School of Physics, Monash University
and
Australian Synchrotron

January 15, 2013

Contents

Contents	i
List of Figures	iii
Summary	vii
Copyright Notice	x
Disclosure	xi
Acknowledgements	xii
1 Introduction	1
1.1 Coherent Synchrotron Radiation (CSR)	1
1.2 CSR from Short Electron Bunches	5
1.3 Coherent Far-IR Synchrotron Radiation	8
1.4 Low Alpha Operation	9
1.5 Stable and Bursting Emission of CSR	12
2 Bunch Length Manipulation using α_c	15
2.1 Longitudinal Dynamics	15
2.2 Negative Dispersion Method of Reducing α_0	23
2.3 Results of Low- α Studies at 3.0 GeV	28
2.4 Summary	38
3 Bunch Length Measurements and Charge Dependent Effects	41
3.1 Current Dependent Bunch Lengthening	45
3.2 Enhancement of the Radiation in the Far-IR Spectrum	50
3.3 Far-IR High Resolution Beamline	53
4 Time Structure of CSR Bursts at 3 GeV	57
4.1 Temporal Profile Analysis	60
4.2 Beam Current Dependent Burst Frequencies	69
4.3 α_1 Dependent Burst Frequencies	71
4.4 Summary	75
5 Optimising Bursts of CSR for the IR Beamline	77

5.1	Absorption Spectra for N ₂ O	83
5.2	Optimising Bursts of CSR with Lower α_0 Values	84
5.3	Summary	86
6	Discussion and Future Directions	89
	Appendices	93
A	Synchrotron Light Sources with Low-α Configurations	95
B	Storage Ring Beam Diagnostics	97
B.1	Beam Position Monitor (BPM)	97
B.2	Stripline BPM and a Real-time Spectrum Analyser	97
B.3	Streak Camera: Chromatic Aberration	98
C	Spurious Sidebands of Two Pre-amplifiers	101
D	Conference Paper	103
	Bibliography	107

List of Figures

1.1	Schematic of the layout of the Storage Ring magnets.	2
1.2	Definition of the curvilinear coordinate system.	3
1.3	Unit cell lattice functions.	4
1.4	Coherence enhancement as a function of λ .	6
1.5	Dipole radiation spectrum with coherence calculations.	7
1.6	Wakefields from passing electrons in a storage ring vacuum chamber.	10
2.1	An energy surface plot in phase space of the Hamiltonian describing the longitudinal dynamics.	21
2.2	Constraints on α_1 .	23
2.3	Storage ring lattice functions for user and low alpha operation.	24
2.4	Scan of parameter space (η_x, η'_x) to minimise the integral $\oint \kappa \eta_x(s) ds$ for the dipole.	25
2.5	Model derived settings for the quadrupoles and sextupoles to reduce the momentum compaction factor, while maintaining a constant chromaticity.	27
2.6	Comparing measured and predicted bunch lengths and synchrotron frequencies.	29
2.7	Beam orbit stability problems.	31
2.8	Schematic showing the distribution and generation of RF power for the storage ring.	32
2.9	Comparison between different diagnostics showing the stability of the RF system.	33
2.10	Fitting for ν_s using spectrum analyser data and a Gaussian function. $\alpha_{0,1}$ is calculated using the measured values of ν_s .	35
2.11	Comparison between BPM and spectrum analyser measurement of f_s .	36
2.12	Dependence of α_1 on the sextupoles.	37
3.1	Components of a streak camera.	42
3.2	Delay block for streak camera calibration.	43
3.3	Calibration of the streak camera.	43

3.4	Streak camera data set collected to calculate the bunch length after calibration.	44
3.5	The real impedance, R , of the storage ring is calculated using measurements of current dependent phase shift.	48
3.6	Fitting the solutions of the Haissinski equation to calculate the inductance, L , of the storage ring. The solutions also show the threshold currents for the microwave instability.	49
3.7	Non-equilibrium solution to the Haissinski equation showing that the distribution does not converge. This occurs when the current threshold is exceeded for a given set of values of σ_t^0 , R and L in Equation 3.1.	49
3.8	Stable emission of CSR observed with a modest enhancement of a factor of 6 above the incoherent radiation.	50
3.9	Bursts of CSR are observed and the enhancement to the radiation spectrum is shown. The power is shown to increase as I^2 .	52
3.10	Observation of the sawtooth pattern from the IR beamline's bolometer. The pattern is observed to become increasingly irregular with increasing beam currents.	53
3.11	Schematic of a Fourier Transform spectrometer.	54
3.12	Schematic of a bolometer	55
3.13	Simulation of the output from a bolometer for a periodic oscillation of the input signal.	56
4.1	Set-up of the 100 GHz detector with an amplifier and oscilloscope.	57
4.2	Bursts of CSR shown with different time scales using a diode detector. Convolution of the data from the diode detector with an exponential response function simulates the output of the bolometer.	58
4.3	Temporal and spectral data shown to compare the CSR generated with single and multiple bunches. A significant increase in noise is observed with multiple bunches.	60
4.4	Plots using the diode detector's data to show that the bursts from multiple bunches are uncorrelated.	61
4.5	Time domain profile of a burst of CSR measured using the IR detector. An FFT shows the frequency profile of the small oscillations observed in a burst of CSR.	61
4.6	Vlasov-Fock-Planck simulation by Warnock [1].	62
4.7	Simulation of the filaments as it propagates in phase space at the synchrotron frequency. The gain factor, $g(\lambda)$, is calculated as a function of time to simulate the signal generated by a diode detector.	64

4.8	Simulation of the time evolution of coupled longitudinal modes causing high frequency oscillations in the observed enhancement. The simulation is compared to measured data.	65
4.9	Spectrum showing the excited longitudinal modes as a function of beam current.	66
4.10	(a) Temporal profile of bursts of CSR as a function of beam current showing the phase relationship between the oscillatory perturbations and overall burst profile. (b) Corresponding spectral plot showing the coupling of multiple modes at higher currents.	67
4.11	(a) Coherent motion of groups of electrons within the larger bunch of electrons. (b) Measured bursts of CSR plotted in normalised time, τ_s , for three different configurations shows similar characteristics; the initial burst of CSR occurs at $\tau_s = 0.25$ followed by a second smaller burst at $\tau_s \approx 0.9$.	68
4.12	Initial measurements with a real time spectrum analyser showing that the burst frequency is current dependent.	70
4.13	Comparison of the temporal profile of the burst of CSR and the burst frequency as a function of the beam current. The results display three distinct burst regimes.	71
4.14	Surface plot of the Hamiltonian equation that describes longitudinal dynamics. The asymmetry in the contours, which represent the same energy values, shows how the longitudinal head-tail instability is excited.	72
4.15	Burst frequencies as a function of the measured α_1 values for a given α_0 .	73
4.16	Plots showing that an increasing asymmetry leads to stronger head-tail instabilities, driving larger synchrotron oscillation amplitudes. As a consequence of a finite aperture in the storage ring the the electron beam current decays, since it is limited by the horizontal aperture.	74
4.17	Comparison of the burst frequency with beam current for three different values of α_1 . (a) $\alpha_1 = 8.0$, (b) $\alpha_1 = 0.2$ and (c) $\alpha_1 = -15.6$.	75
5.1	The profile of the burst changes with current. The results show a step change in the profile as the burst frequency couples to the synchrotron frequency.	78
5.2	Growth and decay rates, and intensities as a function of beam current, calculated from profile measurements taken during an injection.	79

5.3	Plots of the growth rate, decay rate and the SNR show that they are not correlated with α_1 . These are based on measurements at two different chromaticities.	80
5.4	SNR plotted as a function of the burst frequency. Measurements were also made on the IR beamline showing that a maximum in the SNR occurs at a burst frequency of 1800 Hz.	80
5.5	The spectral plot as a function of the beam current was measured on the IR beamline. A comparison is also made with the spectrum for synchrotron radiation during normal operation.	81
5.6	Spectral intensity at 12.4 cm^{-1} plotted as a function of beam current, which shows a peak at 10.2 mA.	82
5.7	The spectrum obtained with bursts of CSR, with and without N_2O . A comparison is made between the measured and known absorption lines for N_2O .	83
5.8	Increase in the burst frequency with single bunch current at lower α_0 values.	85
5.9	Burst frequency as a function of current from the spectrum analyser for $\alpha_0 = 0.46 \times 10^{-3}$ and $\eta_x = -0.75 \text{ m}$.	85
5.10	SNR calculated using the diode detector at $\alpha_0 = 0.46 \times 10^{-3}$ ($\eta_x = -0.75$).	86
B.1	Schematic showing the setup of the BPM and acquisition system used to measure synchrotron oscillations.	97
B.2	Schematic showing the setup of the spectrum analyser used to measure synchrotron oscillations.	98
B.3	Schematic showing the effect of chromatic aberrations on bunch length measurements.	99
C.1	Spurious sidebands generated by two different pre-amplifiers.	101

Summary

The storage ring at the Australian Synchrotron Light Source (ASLS) is an intense source of radiation that is used in applications such as spectroscopy and imaging. The source of the radiation comes from individual electrons that are grouped in bunches and confined in the storage ring. The observed radiation is usually temporally incoherent and the radiation power scales linearly with the number of electrons, N . If all the electrons have a longitudinal distribution of σ_z , the degree of temporal coherence of the emitted radiation increases and the power of the radiation will scale as N^2 for radiated wavelengths, λ , that are longer than $2\pi\sigma_z$. Using this property of coherent synchrotron radiation (CSR), the intensity of the observed radiation at wavelengths longer than λ can be increased by a factor of N above that of the incoherent radiation. With typical values of N around 10^9 , the potential enhancement of the radiation power is significant.

This property of CSR is used to enhance the radiation in the Far-IR¹ spectrum between the wavelengths of 0.3 mm (1 THz) and 3 mm (100 GHz). This region of the radiation spectrum is used by the Far-IR beamline at the ASLS for absorption spectroscopy. The increase in the radiation power will benefit the beamline by increasing the signal-to-noise ratio of the beamline's detector, thereby enabling the measurement of spectra for weakly absorbing materials and providing the capacity to measure spectra at longer wavelengths.

To generate CSR, the bunch length in the storage ring is shortened by reducing the momentum compaction factor, α_c , using the negative dispersion technique. When α_c is reduced by a factor of 100, the storage ring becomes sensitive to perturbations introduced by the accelerator subsystems (e.g., RF system, magnet power supplies and stray electromagnetic fields). An investigation of the various accelerator subsystems showed that the strongest perturbation is at the mains AC frequency of 50 Hz and is caused by currents conducted through the metallic elements of the storage ring. These perturbations limit the shortest achievable bunch length to 1 ps at an electron energy of 3 GeV. A bunch length of 1 ps is not short enough to enhance the radiation power at wavelengths less than 0.3 mm (1 THz). A reduction in the electron beam energy is required to achieve shorter bunch lengths.

¹Far Infrared.

An alternative method for generating CSR is to excite a longitudinal single bunch instability. The instability that modulates the charge density can be utilised to create periodic bursts of CSR. The onset of the instability creates quasi-periodic bursts of CSR. For CSR to be used as a source of IR radiation, the frequency and the intensity of the bursts of radiation must be constant. Any fluctuation in the frequency or intensity reduces the signal-to-noise ratio (SNR) of any measurements using the CSR. In this thesis a method is developed for optimising the SNR using a microwave diode detector.

A microwave diode detector with a fast response time of 1 ns is used to characterise the temporal profile of the CSR bursts. The measurements show a temporal profile with growth and damping rates of 20 kHz which far exceed the natural damping rate expected for the storage ring. Moreover, the results show small oscillations that are believed to be the result of the filamentation of the electron bunch. The observed features of the growth rate, decay rate and small oscillations closely resemble the behaviour seen in numerical simulations by Venturini and Warnock [2], which show a CSR driven microbunching instability. This model provides a framework for describing the process leading to bursts of CSR.

The microwave diode detector is also used to measure the temporal profile's dependence on N . The data collected was used to calculate the change in the SNR to find the optimal working current where the SNR is maximised. The results show that the SNR depends on the burst frequency; in particular when a harmonic of the burst frequency is the same as the characteristic longitudinal oscillation frequency (synchrotron frequency). Measurements were also conducted on the beamline, and the results agree with the observations made using the diode detector. These observations were used to define a low alpha lattice configuration to generate CSR. The CSR created from this configuration was used to measure the absorption spectrum of a sample of N_2O with a spectral resolution of 0.025 cm^{-1} (750 MHz). For these measurements a Bruker IFS125HR spectrometer was utilised on the IR beamline. This is a challenging measurement as the scan takes 15 minutes to complete, during which the intensity of the source must remain constant. Any fluctuation in the intensity will introduce noise into the spectrum. The results of 20 scans show good agreement between our measurements and previously documented absorption lines for N_2O . The outcome shows that the quasi-periodic bursts of CSR can be used to extend the utility of the IR beamline into the Far-IR spectrum.

In summary we have used a diode detector to characterise the burst of CSR at the onset of the microwave instability. We have shown that the measurements with a microwave diode detector are in agreement with numerical simulations carried out for this form of instability. A method has also been

developed to create a low alpha operational mode that generates bursts of CSR optimised for the IR beamline.

Copyright Notice

Under the Copyright Act 1968, this thesis must be used only under the normal conditions of scholarly fair dealing. In particular no results or conclusions should be extracted from it, nor should it be copied or closely paraphrased in whole or in part without the written consent of the author. Proper written acknowledgement should be made for any assistance obtained from this thesis.

I certify that I have made all reasonable efforts to secure copyright permissions for third-party content included in this thesis and have not knowingly added copyright content to my work without the owner's permission.

Disclosure

This thesis contains no material which has been accepted for the award of any other degree or diploma in any university or other institution. To the best of my knowledge the thesis contains no material previously published or written by another person, except where due reference is made in the text of the thesis.

Yaw-Ren Eugene Tan

Michael J. Morgan

Greg LeBlanc

Acknowledgements

I would like to acknowledge the fantastic support of the people on the IR beamline. Without the support from the people from the beamline I could not have pursued this course of research. In particular I would like to thank Dominique Appadoo for advocating the benefits of CSR for the beamline and for spending many hours with me collecting data. I would also like to thank Danielle Martin, Ruth Plathe and Mark Tobin on the IR beamline for their support as well as their patience with the CSR project. I would also like to thank Adam Walsh for designing, fabricating and installing the movable mirror on the IR beamline.

I have to express my gratitude to the Australian Synchrotron for giving me this opportunity to pursue my personal research while working full time. Specifically I need to thank my group leader Greg LeBlanc for the support he has given me so that I have the time and resources to conduct my research.

There has also been fantastic support from those that I work with at the Australian Synchrotron. Mark Boland for the constant reminder to push ahead and finish the thesis. David Zhu for helping with my questions on synchrotron radiation. Rohan Dowd, Kent Wootton and Simon Cunningham for volunteering a significant portion of their time to help proof read my thesis.

Last and certainly not least I am extremely grateful to Michael Morgan for his untiring support. I have to admit that although he was probably not the supervisor that I wanted, he was the supervisor that I needed. Where I was lazy he would pull me up. Where I was careless he would push me to be meticulous.

Through the course of this research I also had the love and support of my family, especially when things were looking down.

Introduction

This thesis reports on work carried out to create a mode of operation for the ASLS that enhances the intensity of the radiation in the Far-IR spectrum beyond what is currently available for users on the IR beamline. The research focuses on using single bunch instabilities as the method of forming density modulations that create bursts of coherent synchrotron radiation (CSR), which give the desired enhancement of the radiation intensity. The key is the ability to control the parameters of the storage ring, such that the bursts of CSR are periodic in time and have constant intensity. We shall begin by giving a brief overview of CSR and how it is generated at the ASLS.

1.1 Coherent Synchrotron Radiation (CSR)

Synchrotron radiation refers to electromagnetic radiation that is generated by the transverse acceleration of relativistic charged particles moving in a magnetic field. This form of radiation was first observed at a prototype synchrotron particle accelerator¹ [3], hence its name. In the years after the discovery, the use of synchrotron radiation as a source for spectroscopy, diffraction and imaging has grown significantly. First generation synchrotron radiation sources extracted the radiation parasitically from synchrotron accelerators that were used as colliders. Second and third generation sources, commonly called light sources, were dedicated facilities created for the sole purpose of generating synchrotron radiation for scientific research. The properties of the radiation that make it unique are a broad photon spectrum ranging from $\lambda = 1$ mm down to $\lambda = 1$ Å, and a spectral brilliance² that is orders of magnitude above conventional laboratory sources, such as x-ray tubes.

¹Around the same time man-made sources were discovered, astrophysical sources were also found to generate synchrotron radiation.

²Brilliance refers to spectral brilliance and is defined as the number of photons per second per rad² per 0.1%BW where BW (bandwidth) is $\Delta\omega/\omega$.

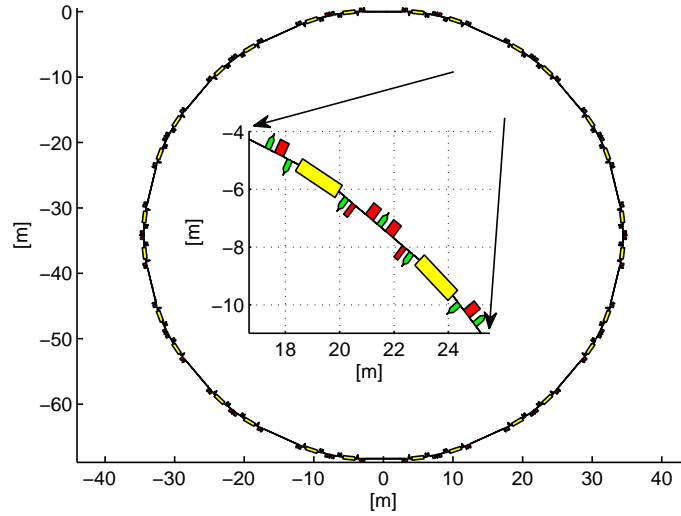


Figure 1.1: Top down view of the storage ring at the ASLS with dipoles (yellow rectangular elements), quadrupoles (red rectangular elements) and sextupoles (pentagons). The inset shows a single sector of magnets (of which there are 14) that make up the storage ring. The electrons travel in straight lines until they are bent by the vertical magnetic field of the dipole magnets.

The Australian Synchrotron Light Source (ASLS), where the work reported in this thesis was conducted, is a third generation light source and we shall briefly introduce some of its features [4]. The ASLS uses a linear accelerator and booster synchrotron to accelerate electrons to a kinetic energy of 3 GeV³. These electrons are accumulated and stored in a specially designed “storage ring” that confines the motion of the electrons in a circular path on the horizontal plane using electromagnets. To ensure a long lifetime in the storage ring, the electrons are kept in an ultra-high vacuum within stainless steel chambers threaded through electromagnets. The main electromagnets (dipoles) that create vertical magnetic fields ensure that the electrons are on a circular path by creating a radial Lorentz force. It is the centripetal acceleration due to the Lorentz force (as observed in the laboratory frame) that is responsible for the generation of synchrotron radiation. The arrangement of the dipoles, and other magnets such as quadrupoles for focusing the electron beam⁴, is called the lattice design. At the ASLS the lattice is based on a Chasman-Green [5] unit cell replicated 14 times to form a 14-fold symmetric ring, as shown in Figure 1.1. The Chasman-Green lattice is an optimised design based on second generation light sources with the emphasis on long straight sections between unit cells for insertion devices and RF cavities.

³Gigaelectron volt.

⁴The quadrupoles are analogous to concave and convex lenses in optics.

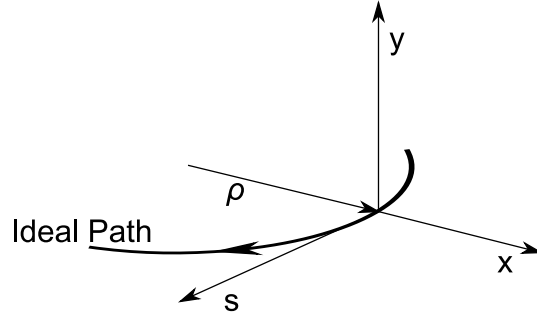


Figure 1.2: Curvilinear coordinate system with axes x (radially outwards), y (vertically up) and s that is collinear with the ideal electron path. ρ is the bending radius of the electron traversing the magnetic field of a dipole magnet.

The properties that describe the behaviour of particles in the storage ring, such as the beam size, are given by lattice functions and are defined in a curvilinear coordinate system x , y , and s as shown in Figure 1.2. These lattice functions come from solutions to the equations of motion for particles in the storage ring. The details of the derivation are not relevant to this brief overview and the reader is referred to Reference [6]. For the ASLS the lattice functions are shown in Figure 1.3, where $\beta_{x,y}(s)$ is a position dependent scaling factor that is a measure of the beam size and $\eta_x(s)$ is the horizontal dispersion giving the change in the horizontal position as a function of energy perturbations. Vertical dispersion is zero everywhere because the deflection of the ideal electron is only in the horizontal plane. Therefore a change in the energy will only result in a change in the horizontal position (finite dispersion) and not in the vertical direction (zero dispersion). These lattice functions can be used to describe the beam size, σ , according to

$$\sigma_u(s) = \sqrt{\beta_u(s)\epsilon_u + \eta_u(s)^2\delta^2}, \quad (1.1)$$

where $u = x, y$ are the transverse coordinates perpendicular to the direction of motion of the electron beam, $\delta = \Delta p/p$ is the relative longitudinal momentum spread and ϵ_u is the equilibrium transverse emittance⁵.

In addition to the magnets that guide and confine the electron beam, the storage ring is designed to keep the energy, E_0 , constant and any losses in energy through the emission of synchrotron radiation are compensated by using radio frequency (RF) cavities. The electric fields in these cavities oscillate at a frequency of 499.667 MHz and create accelerating fields for half of the cycle and decelerating fields for the other half. As there is a net

⁵Emittance is a measure of the area of the horizontal and vertical phase space with conjugate pairs, (x, p_x) and (y, p_y) , where $p_{x,y}$ is the momentum in the x and y direction, respectively. For example, the area is $\pi\epsilon_x = \pi\sigma_x\sigma_{p_x}$.

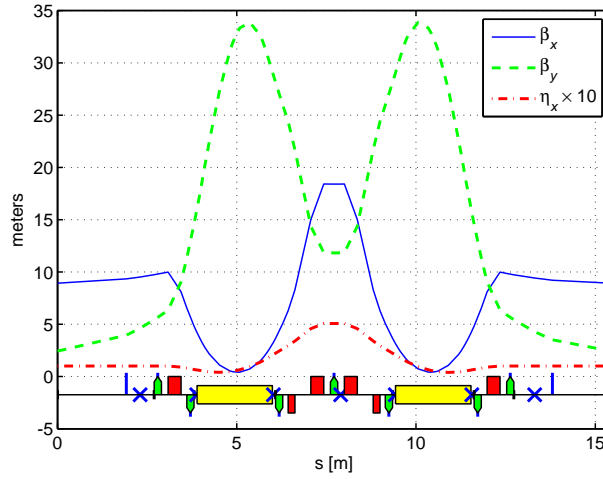


Figure 1.3: Lattice functions for a unit cell are shown along with the arrangement of the magnets at the bottom of the plot. Dipoles (long yellow rectangles), Quadrupoles (short red rectangles), Sextupoles (short green pentagons) and correctors (blue vertical lines). Beam position monitors are marked with crosses.

loss in energy from the emission of synchrotron radiation, acceleration is required to restore the energy lost to keep the energy, E_0 , constant. The electrons remain at a particular phase of the RF cycle, called the synchronous phase, so that the accelerating fields gives the electrons just enough energy to compensate for the energy lost to synchrotron radiation. This results in the electrons forming discrete bunches that are spaced one RF period (2 ns) apart and depending on the circumference of the storage ring, there will be an integer number of bunches. The gradient of the accelerating field provides longitudinal focusing so that particles that experience a perturbation will experience a longitudinal restoring force to keep the particles on the synchronous phase. The damping effect arising from the energy loss to synchrotron radiation ensures that particles scattering off residual gas molecules in the vacuum chamber will oscillate about and converge towards the synchronous phase. The characteristic frequency of the oscillation about the synchronous phase is called the synchrotron frequency. A more detailed mathematical description of the dynamics is given in Chapter 2.

The ASLS shares similarities with many other third generation light sources. For the next generation of light sources (fourth generation), the temporal coherence of the synchrotron radiation is exploited to improve the brightness beyond what is achievable at third generation light sources. The temporal coherence of the the emission of radiation from a group of electrons means the electromagnetic waves constructively interfere, resulting in a photon flux which is proportional to the square of the number of electrons,

$\dot{N}_{\text{ph}} \propto N_e^{-2}$. This is in contrast to incoherent radiation, where the photon flux is linearly proportional to the number of electrons, i.e. $\dot{N}_{\text{ph}} \propto N_e$. This is the principle behind free electron lasers (FELs), which have a potential peak brightness as much as 10^9 times greater than storage ring sources [7–9]. Such an enhancement of the peak brightness is attractive for experiments with small sample sizes (e.g., individual molecules), or in the study of atomic or molecular processes on time-scales of less than 1 ps.

Exploiting the benefits of CSR is also possible with a storage ring. At the ASLS the electron density can be manipulated by operating in a particular mode, such that the radiation is temporally coherent over a limited spectral range in the Far-IR. In what follows we will discuss how the coherence of the radiation depends on the charge distribution of the electron bunch. Further, we will describe the Low Alpha technique used to manipulate that distribution. Finally, we will briefly discuss the two modes of operation that are used at light sources to generate CSR.

1.2 CSR from Short Electron Bunches

The temporal coherence of the emitted electromagnetic wave for a given wavelength, λ , means the radiation from the individual sources are in phase. If z is the longitudinal coordinate relative to the centre of mass of a bunch of electrons in the storage ring, then a longitudinal distribution with $\sigma_z \ll \lambda$ implies that radiation with wavelength, λ , would be in phase and temporally coherent. This also means that the coherence is a function of the distribution of the electrons.

To find the relationship between coherence and the charge distribution, we define the electric field of the radiation as proportional to $\exp i\left(\frac{2\pi}{\lambda}z + \omega t\right)$. The total power, $P(\lambda)$, emitted by the N electrons in a single group at wavelength, λ , is given by [10]:

$$\begin{aligned} P(\lambda) &= p(\lambda) \sum_{m,n}^N e^{+i\left(\frac{2\pi}{\lambda}z_m + \omega t\right)} e^{-i\left(\frac{2\pi}{\lambda}z_n + \omega t\right)} \\ &= p(\lambda) [N + N(N-1)g(\lambda)], \end{aligned} \quad (1.2)$$

where $p(\lambda)$ is the power emitted by a single electron and $g(\lambda)$ is a form factor defined as

$$g(\lambda) = \left| \int_{-\infty}^{+\infty} n(z) e^{i\frac{2\pi}{\lambda}z} dz \right|^2. \quad (1.3)$$

Here $n(z)$ is the normalised charge density distribution function⁶. The first part of Equation 1.2 refers to the incoherent contribution that scales as N ,

⁶Normalisation requires that $\int_{-\infty}^{+\infty} n(z) dz = 1$.

while the coherent contribution scales as $N(N-1)g(\lambda)$, where $g(\lambda)$ is a measure of the coherence at wavelength, λ , for an arbitrary charge distribution, $n(z)$. When $N \gg 1$, $P(\lambda)$ is enhanced by a factor of $Ng(\lambda)$. With typical populations around $N = 10^9$, even small values of $g(\lambda)$ can enhance the power by many orders of magnitude above the incoherent radiation.

It is useful to note that the coherence function $g(\lambda)$ is essentially a Fourier transform of $n(z)$. Therefore the frequency components that form the shape of the distribution determine the frequencies that will radiate coherently. For example, if the charge distribution is Gaussian, $n(z) = \exp(-z^2/2\sigma_z^2)/(\sigma_z \sqrt{2\pi})$, a Fourier transform will also be Gaussian, whence Equation 1.3 adopts the form [11]:

$$g(\lambda) = \exp\left(\frac{-4\pi^2\sigma_z^2}{\lambda^2}\right). \quad (1.4)$$

To illustrate the expected enhancement for different wavelengths, a plot of the factor $Ng(\lambda)$ is shown in Figure 1.4 for 2×10^9 electrons for different Gaussian distributions. Due to the large value of N , the power at a wavelength

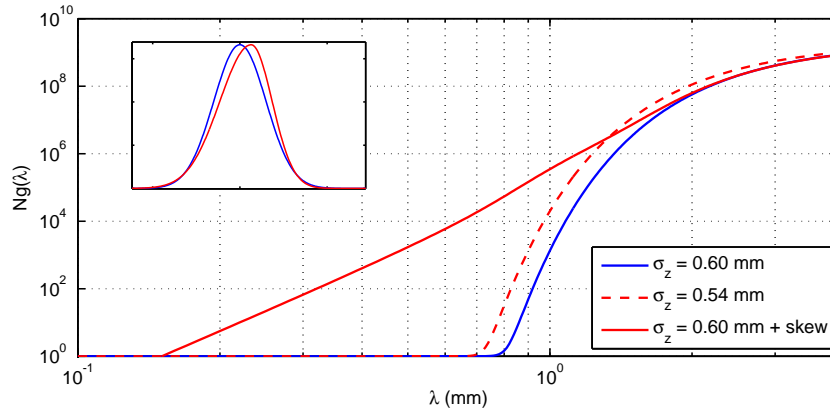


Figure 1.4: Comparison of the gain expected for 2×10^9 electrons in a Gaussian distribution with $\sigma_z = 0.60$ mm and $\sigma_z = 0.54$ mm. This shows that a 10% change in the bunch length can affect the enhancement by a factor of 10. Enhancements at shorter wavelengths (i.e. higher frequencies) can occur with a skewed Gaussian distribution (see inset) as its spectral content has higher frequency components compared to an unskewed Gaussian.

of $\lambda = 1.1$ mm (0.5 THz) can be enhanced by as much as 10^4 when $\sigma_z = 0.6$ mm. Conversely the large value of N also means a greater sensitivity to the bunch length as seen in Figure 1.4 when comparing a Gaussian bunch with $\sigma_z = 0.6$ mm and $\sigma_z = 0.54$ mm. A reduction of the bunch length by 10% can increase the enhancement by a factor of 10. To achieve coherence at shorter wavelengths, either the bunch length has to be shorter, or the distribution needs to contain higher frequency components. An example simulated in Figure 1.4 (inset) is a skewed Gaussian distribution with a steeper rising

(falling) edge. Simulations show that with a skewed distribution the power at a wavelength of $\lambda = 0.65$ mm can be enhanced by a factor of 10^4 , compared to $\lambda = 1.1$ mm with an unskewed Gaussian distribution. Using Equation 1.4 we can define $\lambda_{coh} = 2\pi\sigma_z$, so that wavelengths longer than λ_{coh} are considered coherent.

This enhancement of the radiation power is not normally observed in storage rings due to the shielding effects of the metallic vacuum chamber. The metallic chamber forms a waveguide-like structure for the emitted electromagnetic (EM) waves with a defined cut-off wavelength for propagation within the vacuum chamber [10, 12]. For a rectangular vacuum chamber, where the width is larger than the height, the cut-off wavelength is given by [13, 14]

$$\lambda_c \approx 2b^{3/2}\rho^{-1/2}, \quad (1.5)$$

where b is the vertical full height of the chamber and ρ is the bending radius of the dipole magnet. For the ASLS $\lambda_c = 2(0.032)^{3/2}(7.7)^{-1/2} = 4.1$ mm. This is the longest wavelength that can be supported and propagated by the vacuum chamber. This limit is plotted in Figure 1.5 against the dipole radiation

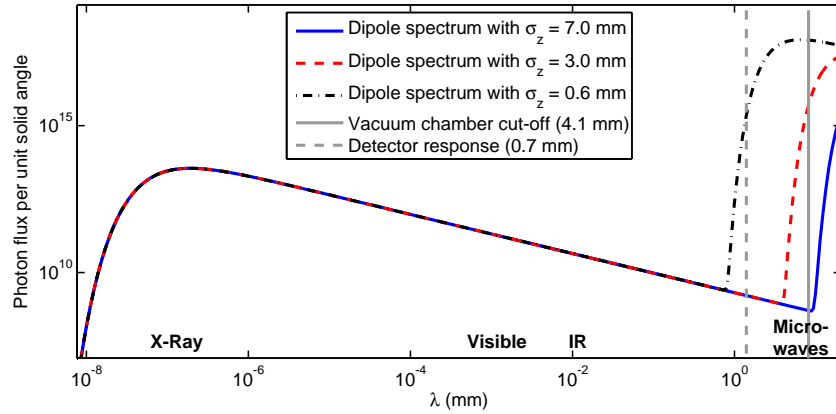


Figure 1.5: Dipole radiation spectrum calculated with the enhancement effect shown for the nominal bunch lengths $\sigma_z = 7$ mm, $\sigma_z = 3.0$ mm and at $\sigma_z = 0.6$ mm. The vacuum chamber threshold (4.1 mm) must be greater than the response of the detector (0.7 mm). We assume 2×10^9 electrons.

spectrum with CSR enhancement for the nominal bunch length of $\sigma_z = 7.0$ mm, $\sigma_z = 3.0$ mm and for a shorter bunch with $\sigma_z = 0.6$ mm. The chamber cut-off at 4.1 mm shows why at nominal bunch lengths CSR is not produced. The response of the detector itself has to be taken into consideration as well. Although CSR is enhancing the longer wavelengths of the spectrum when the bunch length is 3.0 mm, the detector cannot measure the enhancement. To take advantage of the increased intensity of CSR, σ_z needs to be set such that $\lambda_{coh} < \lambda_c$ and within the response of the detector.

As Figure 1.5 shows, the advantage of the increased intensity from CSR in the Far-Infrared (IR) and microwave spectrum (millimetre waves) is very significant. The enhancement in this spectral range will increase the sensitivity and reduce measurement times for users that exploit radiation in the Far-IR spectrum.

1.3 Coherent Far-IR Synchrotron Radiation

The use of storage rings as an IR source was greatly influenced by the analysis of Duncan and Williams [15, 16], who showed that despite similar or larger photon flux from thermal sources, the small source size and collimated nature of synchrotron radiation meant that it is a brighter source [17]. Such a source is ideally suited to applications such as IR micro-spectroscopy for surface science [17], as well as time resolved experiments that investigate the properties of superconductors [18]. Experimental stations, commonly referred to as beamlines, that utilise the IR spectrum are now found at many third generation light sources [17].

In IR science there is a region of the electromagnetic spectrum between microwaves and IR (0.1 to 30 THz), that is difficult to generate and is commonly referred to as the THz gap. The most common source of radiation in this spectral range is a Mercury lamp in the form of black body radiation. However, the integrated power in the THz spectrum is of the order of nanowatts. The generation and application of THz radiation is an active area of research, finding new applications in materials science and biology [19,20]. There are now various laboratory instruments that exploit THz radiation by using the technique of THz Time Domain Spectroscopy (THz-TDS); these use femtosecond laser pulses to produce ultra-short electromagnetic (EM) waves on a semiconductor emitter (or crystal) to generate THz radiation [21]. This method is not dissimilar to what is achieved with short electron bunches in a storage ring, except that the charge density for a storage ring is greater. THz-TDS techniques can generate an average power in the order of mW in narrow bandwidths that is tunable from 0.1 to 3.0 THz. There are also semiconductor based sources, such as GUNN and IMPATT diodes [21], that can generate radiation with power on the order of mW in a relatively broad bandwidth up to 1 THz. For high powered sources there are THz Free Electron Lasers (FELs), such as FELIX and the Electron Recirculation Linac (ERL) facility at the Jefferson Laboratory [22], which can generate average power on the order of 100 W [23].

The idea of using electron storage rings as a source of THz radiation was suggested by Duncan in 1983 [15]. Measurements by Yarwood *et al.* [24]

and Schweizer *et al.* [25] verified that the incoherent radiation in the THz spectrum at a storage ring light source was superior to the standard Mercury lamp source used in most laboratories. In 2003 at the Berlin Electron Storage Synchrotron (BESSY) an improvement in the radiation was achieved by using short electron bunches in a storage ring to increase the coherence in the THz spectrum. An average power of 1 mW was detected in the spectral region spanning 0.3 to 1.6 THz [26]; this represents a factor of 10^6 more than the incoherent radiation [27]. The most recent measurement at a light source came out of the Metrology Light Source (MLS), which demonstrated that an average power of 60 mW and peak powers of 35 W can be achieved [28]. Such enhancements with coherent Far-IR radiation were realised by reconfiguring the parameters of the storage ring to operate with a low alpha, where the bunch length can be decreased by a factor of 10. By operating with a low alpha, existing synchrotrons designed for high energy photons, can be configured to increase the emission of photons in the Far-IR spectrum.

Light sources such as BESSY, ANKA, MLS, Diamond, Soleil and Elettra, have dedicated time for researchers to use coherent Far-IR synchrotron radiation. Some of the operating parameters of these light sources are listed in Appendix A. To produce THz radiation for many users it has been proposed to build dedicated storage ring sources, such as CIRCLE [29], where 10 W can be generated in a broadband spectrum spanning 0.1 to 2 THz.

1.4 Low Alpha Operation

The low alpha method refers to minimising the momentum compaction factor, α_c , to reduce bunch lengths. The momentum compaction factor is a measure of the change in the longitudinal path length (relative to an ideal particle) as a function of energy deviation from the ideal particle. It is defined by

$$\alpha_c = \frac{\Delta L_0/L_0}{\Delta p/p}, \quad (1.6)$$

where L_0 is the distance travelled by an ideal particle in one revolution of the storage ring and p is the momentum of the ideal particle. The bunch length will therefore be a function of the equilibrium energy spread and α_c . The idea of controlling and reducing the electron bunch length was proposed by Bruck [30] for electron-positron colliders in order to increase the luminosity⁷. The application to a storage ring was initially attempted at BESSY in 1985 [31], and showed the practical application of this technique. A few years later in 1989 the first observation of CSR from short electron bunches

⁷Luminosity is a measure of the interaction rate between two colliding beams per unit cross section (in units of particles/m²s)

was observed at the Tohoku 300 MeV Linac [32], confirming the principles described in Section 1.2 in which short electron bunches radiate coherently with intensities many orders of magnitude greater than the incoherent radiation. Detailed theoretical investigations to understand the dynamics of low alpha operation in storage rings started in 1991. These studies showed that it was possible to generate short x-ray pulses for time resolved beam line experiments (incoherent radiation) and to generate coherent THz radiation [33–35]. In 1993 at the Ultraviolet Synchrotron Orbital Radiation Facility (UVSOR) and Super-ACO in 1996 [36–38], the Low Alpha technique was applied to reduce the bunch length and confirm the generation of CSR in storage rings. Since then many other synchrotron light sources have been able to generate CSR [26, 39–44], including preliminary work at the ASLS by this author [45] (see Appendix D).

For the storage ring to be an intense source of radiation, the charge per electron bunch should be maximised. However, there is an upper limit, as charge dependent longitudinal instabilities have to be considered. An electron travelling relativistically within a metallic vacuum chamber will have electric fields that extend radially outwards towards the chamber wall. This is accompanied by a ring of mirror charges that travel with the electrons. Due to the finite resistance of the chamber and changing geometry of the chamber walls, the mirror charges can generate trailing electromagnetic fields that act back on the electrons. These fields are known as wakefields and are illustrated in Figure 1.6. The longitudinal component of the wakefields

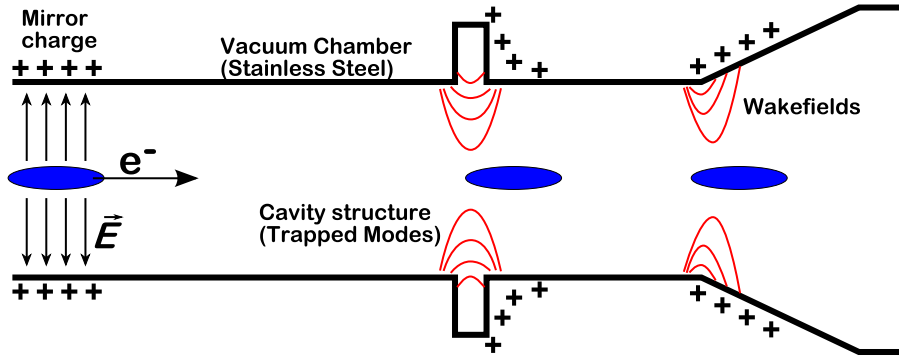


Figure 1.6: Relativistic electrons will only have radial electric fields, \vec{E} , with corresponding mirror charges on the chamber wall. As the mirror charges encounter changes in the longitudinal geometry of the chamber, wakefields are generated that have an effect on the electron bunch that created them. In some cases, cavity-like structures are encountered and the resonant mode of the cavity can be excited leading to long lasting oscillating fields called trapped modes.

created by an electron can be described by a wake function, $W^{\parallel}(t)$, measured

in units of $\text{V C}^{-1} \text{ s}^{-1}$, where the convention is $t < 0$ for particles at the front of the bunch. The Fourier transform of the wake function in the frequency domain is called the impedance and is given by $Z^\parallel(\omega) = \mathcal{F}(W^\parallel(t))(\omega)$. Wakefields that last longer than the RF period of 2 ns can result in a bunch of electrons affecting trailing bunches of electrons, leading to coupled bunch longitudinal motion. If the motion is positively reinforced, sustained coupled motion will give rise to a longitudinal instability. For wakefields that are short lived, affecting only the electron bunch that created them, single bunch longitudinal instabilities can arise. In this thesis the focus will be on the effects of single bunch longitudinal instabilities and how it generates CSR.

The commonly observed effect of the short range self-interaction is an elongation of the bunch length with increasing charge, called the potential well distortion effect (PWD). The equilibrium solution to this non-linear problem was given by Haissinski in 1973 [46], who showed analytically how equilibrium distribution is perturbed by the wakefields. As the charge increases, the wakefields become stronger and eventually a threshold is reached where no equilibrium solutions are found.

This limit is known as the microwave instability threshold, named for the microwave signals generated when the threshold is exceeded [47]. First observed in proton synchrotrons, the instability is associated with a rapidly increasing bunch length not attributable to PWD [48]. In electron synchrotrons, where radiation effects are important, the instability has been observed as the sawtooth instability [49], where the emission of microwaves occur quasi-periodically. The threshold at which this instability occurs is usually calculated from the Boussard criterion for the stability of bunched beams [47]:

$$\frac{Z^\parallel(\omega)}{n} \leq F' \frac{E_0 |\eta_c| \gamma \sigma_t}{\sqrt{2\pi} I_b T_0} \delta_{\text{FWHM}}^2, \quad (1.7)$$

where $\frac{Z^\parallel(\omega)}{n}$ is the longitudinal impedance normalised to $n = 2\pi/\sigma_t \omega_{\text{rev}}$, ω_{rev} is the revolution frequency, E_0 is the electron energy in units of electron volts (eV), η_c is the phase slip⁸, γ is the relativistic gamma factor, σ_t is the bunch length in units of seconds, δ_{FWHM} is the full width at half maximum of the relative momentum spread, I_b is the total bunch current in ampere, T_0 is the revolution period, and F' is a form factor determined by the bunch distribution.

Using Equation 1.7, Boussard showed that knowing the charge distribution of the electron bunch is critical in determining the instability threshold. The criterion also shows that with a decreasing bunch length (reduction in

⁸Defined later in Equation 2.5 as $\eta_c = \gamma^{-2} - \alpha_c$.

η_c), there is a reduction in the threshold current, I_b , at which the instability occurs, as the impedance $\frac{Z^{\parallel}(\omega)}{n}$ does not change. Therefore with the short bunches required to generate CSR, the maximum current in a single bunch is limited by the instability threshold that is dependent on the environment of the electron beam. Exceeding the threshold also generates CSR, but in this scenario the CSR is generated in quasi-periodic bursts. This phenomenon has been observed at many light sources when operating with high current short bunches [50–54].

A description of the microwave instability was given by Sacherer in 1977 [55] in terms of longitudinal modes along the charge distribution that are excited by wakefields. This was used by Oide, Bane, Chao and Mosnier [56–59] to describe the periodic lengthening and relaxation of the bunch that results in quasi-periodic bursts of CSR. However, the model requires a high frequency resonator as a driving force that excites the mode and does not give a good explanation of what the source might be. Taking a different approach, Stupakov and Heifets [60] postulated that the instability is driven by CSR rather than vacuum chamber induced wakefields. This approach proposes that small random density modulations in the bunch distribution generate CSR that, like wakefields, is self interacting and modulates the bunch density to form microbunches. As the microbunches grow so does the intensity of the CSR, leading to an exponential growth of the instability, before Landau damping causes the growth to reverse. The analytic model of Stupakov and Heifets [60] only describes the initial conditions giving equations for the wavenumber of the fastest growing instability. To model the non-linear dynamics as the instability grows, the Vlasov-Focke-Planck (VFP) equation is used [61–63]. In Chapter 4 we present results that support the VFP simulations in Reference [62].

1.5 Stable and Bursting Emission of CSR

The stable emission of CSR relies on the principles outlined in Section 1.2, in which the bunch length in the storage ring is reduced to $\sigma_z \approx 0.3$ mm. To ensure that the electron bunch is stable, the charge needs to be below the single bunch instability threshold. When this is achieved the bunch density spectrum that determines the coherence factor, $g(\lambda)$, in Equation 1.3 dictates the spectral range of the coherence. A successful example of this stable mode was demonstrated at BESSY II [26], where at $\sigma_z = 1$ mm, enhancements of up to 10^4 were achieved for wavelengths as short as $\lambda = 0.25$ mm (1.2 THz or 40 cm^{-1}). Theoretically a Gaussian distributed bunch of $\sigma_z = 1$ mm should not show enhancements at wavelengths shorter than $\lambda = 0.50$ mm (0.6 THz

or 20 cm^{-1}). The observed enhancement at shorter wavelengths has been shown to be the result of the deformation of the Gaussian distribution from the PWD [64, 65] (see also Figure 1.4). To achieve this, α_c needs to be reduced by a factor of 100 and the control of higher order components in $\Delta p/p$ are required for beam stability. The significant reduction in α_c also makes the storage ring sensitive to perturbations due to various accelerator subsystems, such as the magnets and RF systems [40, 66]. The challenges of reducing the bunch lengths in storage rings is discussed in Chapter 2.

When the threshold of the electron beam current for the microwave instability is exceeded, the emission of CSR occurs in bursts. The bursts are initially quasi-periodic, eventually becoming stochastic at higher currents [51, 53, 67]. To utilise bursts of CSR on a beamline, the longitudinal instability needs to be characterised and this is the focus of Chapter 3, 4 and 5.

In Chapter 3 we discuss bunch length measurements, which characterise the wakefield structure of the vacuum chamber for different machine configurations. The description of the wakefield will then be used to model the expected instability threshold and the current dependence of the bursts of CSR. The bursts are also characterised using the IR beamline's detectors, showing the intensity, spectral range and stability of the generated CSR. Chapter 4 relates the observed bursts of CSR with a model, which uses measurements of the time structure of the bursts and parameters, such as the beam current and momentum compaction factor. Analysis of the time structure data of the bursts gives an estimate of which configuration of the storage ring is optimal for the IR beamline. Chapter 5 presents results of experiments conducted on the IR beamline, which demonstrate the enhancement of the intensity at long wavelengths and confirms the stability of operation. The working configuration is then used to collect high resolution absorption spectra of N_2O as a proof of principle application. Finally, in Chapter 6 a summary of what has been learnt and future research directions are presented.

Bunch Length Manipulation using α_c

The momentum compaction factor, α_c , gives the relationship between the change in the path length, L_0 , as a function of the particle's momentum, p . The relationship to the bunch length and how higher orders of α_c affect the longitudinal stability will be discussed in Section 2.1. After introducing the theory relevant to this thesis, Section 2.2 introduces the negative dispersion technique to control α_c for the ASLS lattice. The practical application of controlling α_c is highlighted in Section 2.3, where we show that the successful reduction in the bunch length has associated problems with the positional stability of the electron beam.

2.1 Longitudinal Dynamics

The longitudinal dynamics and bunch length in a storage ring are determined by the interaction of the electrons with the RF fields in a metallic cavity structure. The effective cavity voltage experienced by an electron is defined by¹

$$V = V_0 \sin(\psi) = V_0 \sin(\omega_0 t - k_0 s), \quad (2.1)$$

where V_0 is the peak cavity voltage, ψ is the phase in the frequency cycle, ω_0 is the RF frequency and k_0 is the RF wavenumber. The change in the energy of the particle, E , is then given by

$$\Delta E = qV(\psi) - U(E), \quad (2.2)$$

where $U(E)$ is the energy lost by the particle to synchrotron radiation and q is the electron charge. In a storage ring the energy imparted by the RF system equals the energy lost to synchrotron radiation. Therefore $\Delta E_0 = 0$ and $qV(\psi_s) = U_0$ for particles with the ideal energy E_0 . The phase at which

¹The definition $\psi = \omega_0 t - k_0 s$ is used rather than $\psi = k_0 s - \omega_0 t$. This maintains the conventional definition of Equation 2.3.

this occurs is called the synchronous phase. There are two definitions of the synchronous phase given by:

$$\psi_s = \pi - \sin^{-1}(U_0/qV_0) \quad \text{for } \eta_c < 0 \quad (2.3)$$

$$\psi_s = \sin^{-1}(U_0/qV_0) \quad \text{for } \eta_c > 0, \quad (2.4)$$

where η_c is called the phase slip and is defined as

$$\eta_c = \gamma^{-2} - \alpha_c, \quad (2.5)$$

where γ is the relativistic gamma factor and α_c is the momentum compaction factor. During normal operation of the ASLS storage ring, $\eta_c < 0$, and is constrained by the requirement that $\eta_c q [dV/d\psi]_{\psi_s} > 0$. The phase slip can also be expressed as the change in the revolution period as a function of energy, so that:

$$\frac{\Delta T_0}{T_0} = \eta_c \frac{\Delta p}{p}, \quad (2.6)$$

where T_0 is the revolution period.

Electrons with the ideal energy will be at a constant phase at every revolution period T_0 ; therefore the time derivative $\dot{\psi}_s = 0$. To study the evolution of ψ about ψ_s for small changes in particle momentum, Δp , a variation of the phase term in Equation 2.1 is used, i.e.,

$$\begin{aligned} \Delta(\dot{\psi}_s) &= -\Delta(kc\beta - \omega) \\ &= -ck\frac{\partial\beta}{\partial p}\Delta p - c\beta\frac{\partial k}{\partial p}\Delta p, \end{aligned} \quad (2.7)$$

where $\beta = v/c$ and ω do not change with time. The momentum defined as $p = mc\beta\gamma$ can be rearranged to give²

$$\frac{\partial\beta}{\partial p} = \frac{\beta}{p\gamma^2}, \quad (2.8)$$

and the equation $k = 2\pi h/L_0$ can be rearranged to give

$$\frac{\partial k}{\partial p} = \frac{\partial k}{\partial L_0} \frac{\partial L_0}{\partial p} = -\frac{k}{L_0} \frac{\partial L_0}{\partial p}, \quad (2.9)$$

where h is the harmonic number and L_0 is the storage ring circumference. Equations 2.8 and 2.9 can be used to simplify Equation 2.7, i.e.,

$$\begin{aligned} \Delta(\dot{\psi}_s) &= -\frac{ck\beta}{\gamma^2} \frac{\Delta p}{p} + ck\beta \frac{p}{L_0} \frac{\partial L_0}{\partial p} \frac{\Delta p}{p} \\ &= -ck\beta (\gamma^{-2} - \alpha_c) \frac{\Delta p}{p} \\ &= -ck\beta \eta_c \frac{\Delta p}{p}. \end{aligned} \quad (2.10)$$

²The derivative $dp/d\beta = mc\gamma^3 = p\gamma^2/\beta$.

Equation 2.10 exhibits the phase focusing effect that ensures that particles with the same energy arrive in phase after travelling a distance L_0 . Differentiating Equation 2.10 with respect to time and assuming that β , k and p change slowly with time, compared to the change in ψ , we arrive at the following approximation:

$$\ddot{\psi}_s + ck\beta\eta_c \frac{d}{dt} \frac{\Delta p}{p} = 0. \quad (2.11)$$

Equation 2.11 gives the equation of motion of the synchronous phase ψ_s in terms of the change in the electron beam momentum, p .

To recast Equation 2.11 in terms of V and U_0 , the change in the energy with time is determined by differentiating Equation 2.2 with respect to time giving:

$$\begin{aligned} \frac{d}{dt} \Delta E(\psi) &= \frac{1}{T_0} [qV(\psi) - U(E)] \\ &\approx \frac{1}{T_0} \left[qV(\psi_s) + q \frac{dV}{d\psi} \Big|_{\psi_s} (\psi - \psi_s) - U(E_0) - \frac{dU}{dE} \Big|_{E_0} \Delta E \right] \\ &\approx \frac{1}{T_0} \left[q \frac{dV}{d\psi} \Big|_{\psi_s} (\psi - \psi_s) - \frac{dU}{dE} \Big|_{E_0} \Delta E \right], \end{aligned} \quad (2.12)$$

where a first order Taylor expansion about the synchronous phase, ψ_s , is applied and the condition $qV(\psi_s) + U(E_0) = 0$ is used. The smallest relevant time interval for the ideal particle is one revolution period, T_0 , as the observation point is at one point in the storage ring. Using $\Delta E = \beta c \Delta p$ and Equation 2.10, Equation 2.12 can be rearranged to give:

$$\frac{d}{dt} \frac{\Delta p}{p} = \frac{1}{T_0 \beta c} \left(\frac{q}{p} \frac{dV}{d\psi} \Big|_{\psi_s} \phi + \frac{1}{k\eta_c} \frac{dU}{dE} \Big|_{E_0} \dot{\phi} \right), \quad (2.13)$$

where $\phi = \psi - \psi_s$ and $\dot{\phi} = \dot{\psi}$. Substituting Equation 2.13 into Equation 2.11 gives

$$\ddot{\phi} + \frac{\beta ck\eta_c q}{E_0 T_0} \frac{dV}{d\psi} \Big|_{\psi_s} \phi + \frac{1}{T_0} \frac{dU}{dE} \Big|_{E_0} \dot{\phi} = 0. \quad (2.14)$$

Equation 2.14 describes damped harmonic oscillations generated by small energy perturbations in the longitudinal direction. The characteristic frequency, known as the synchrotron frequency Ω , is given by:

$$\Omega^2 = \frac{\beta ck\eta_c q}{E_0 T_0} \frac{dV}{d\psi} \Big|_{\psi_s}. \quad (2.15)$$

The damping term in Equation 2.14 is governed by dU/dE . This term is dominated by the longitudinal damping introduced as a consequence of synchrotron radiation. At the ASLS the radiation damping rate is 340 Hz. The remainder of this section will principally be concerned with Ω and the effect of radiation damping will be revisited in Section 4.3 when analysing

the measured growth rates of the single bunch instabilities that lead to bursts of CSR.

The equations of motion discussed above refer to a single particle. However in a storage ring the electrons are grouped in discrete bunches. Within each bunch there is a Gaussian distributed energy spread due to the statistical nature of the emission of synchrotron radiation from the electrons. There are analytic equations that can be used to calculate the equilibrium energy spread, $\sigma_E = \sigma_E(\rho, \theta, \eta_{x,y}, E_0)$, where $\eta_{x,y}(s)$ is the transverse dispersion function, $\theta(s)$ is the local bending angle (angular kick) and ρ is the bending radius. For a derivation of σ_E refer to Reference [68]. The one sigma bunch length (in units of time) is defined as

$$\sigma_t = \frac{|\eta_c|}{\Omega} \left(\frac{\sigma_E}{E_0} \right) = \Omega \frac{T_0 E_0}{\omega q \, dV/d\psi} \left(\frac{\sigma_E}{E_0} \right), \quad (2.16)$$

where σ_E/E_0 is the relative equilibrium energy spread. The right hand side of Equation 2.16 shows a linear relationship between the bunch length and the synchrotron frequency. This is useful as Ω is easy to measure and can be used to determine the equilibrium bunch length. Another useful relationship obtained by combining Equations 2.15 and 2.16 is

$$\sigma_t = \sqrt{\frac{T_0 \eta_c E_0}{\beta \omega q \, dV/d\psi}}. \quad (2.17)$$

Since $\sigma_t \propto \sqrt{\eta_c}$, a reduction of σ_t by a factor of 10 requires a reduction of η_c by 100.

With the bunch length defined by Equations 2.16 and 2.17, σ_t can be reduced in a number of ways; namely, by increasing the voltage gradient in the cavities $dV/d\psi$, decreasing σ_E , decreasing E_0 or decreasing η_c . Increasing $dV/d\psi$ requires increasing V_0 and the power delivered by the RF system. Unless designed to do so, significant increases in the output power above what is required during normal operation is not possible. Decreasing σ_E by a significant amount is also generally not possible for a fixed E_0 , as σ_E is dominated by the ratio θ/ρ , which is defined by the number and length of the dipole magnets. A change in σ_E would require redesigning the entire lattice, therefore σ_E is a constant. The two available options are to decrease E_0 or decrease η_c . An analysis of Equation 2.16 shows that $\sigma_t \propto E_0^{3/2}$, thus decreasing E_0 by a factor of 0.5 reduces the bunch length by a factor of 0.35 for the same peak cavity voltage. To get a factor of 10 reduction in bunch length requires the beam energy to drop by a factor of 0.2, i.e., from 3 GeV to 600 MeV.

Although reducing the energy to 600 MeV for low alpha studies is technically possible on the ASLS storage ring, it was not investigated. A conscious

choice was made to focus efforts on understanding how to utilise the bursts from instabilities as this is an area that is not well understood. If bursts of CSR can be utilised, then the enhancement can exceed what is achievable through stable emission. As discussed in Chapter 4, this method of operation will require regular re-injections to maintain the beam current. At present the ASLS injector provides electrons at 3 GeV, where any adjustment to inject at energies less than 3 GeV has not been successful to date. Therefore we chose to investigate the generation of CSR through single bunch instabilities at 3 GeV. In Chapter 6 we will discuss how a lower energy ring can be used.

The second method of reducing the bunch length is to reduce η_c by manipulating the α_c parameter. To be able to manipulate α_c requires a better understanding of the origin and dependence of α_c on the storage ring magnets. In Equation 1.6, α_c is defined as linear in $\Delta p/p$. The higher order dependence of α_c on the momentum can be described by expanding Equation 1.6 to higher orders [69], giving

$$\frac{\Delta L}{L_0} = \xi + \alpha_0 \delta + \alpha_1 \delta^2 + O(\delta^3), \quad (2.18)$$

where $\delta = \Delta p/p$; the momentum independent term, ξ , is defined as

$$\xi = \frac{1}{4} (\epsilon_x \langle \gamma_x \rangle + \epsilon_y \langle \gamma_y \rangle + \epsilon_x \langle \kappa^2 \beta_x \rangle) + \frac{1}{2} (\langle x_{co}'^2 \rangle + \langle y_{co}'^2 \rangle + \langle \kappa^2 x_{co}^2 \rangle), \quad (2.19)$$

where $\epsilon_{x,y}$ is the horizontal and vertical equilibrium emittance, $\gamma_{x,y}$ is the betatron gamma function defined as $\gamma_{x,y}(s) = [1 + \alpha_{x,y}^2(s)]/\beta_{x,y}(s)$, where $\alpha_{x,y}(s) = -\beta'_{x,y}(s)/2$, $\kappa = 1/\rho$ is the horizontal bending curvature, $\beta_{x,y}$ are the betatron functions and x_{co}/y_{co} are the transverse positions relative to the ideal path. The primes denote derivatives with respect to s . Due to the emission of synchrotron radiation there is a non-zero equilibrium distribution of position and momenta for the electrons in a bunch. Depending on the lattice, these particles will have a path length that is longer than L_0 . This is encapsulated in the first half of Equation 2.19. The second half deals with magnet misalignments and field errors in the magnets, which cause the equilibrium orbit of the centre of mass of the bunch of particles to take a path different to the ideal orbit. The momentum dependent contributions to Equation 2.18 are defined as:

$$\alpha_0 = \oint \kappa \eta_0 ds = \langle \kappa \eta_0 \rangle, \quad (2.20)$$

$$\alpha_1 = \oint \kappa \eta_1 + \frac{1}{2} \kappa^2 \eta_0^2 + \frac{1}{2} \eta_0' ds = \langle \kappa \eta_1 \rangle + \frac{1}{2} \langle \kappa^2 \eta_0^2 \rangle + \frac{1}{2} \langle \eta_0'^2 \rangle, \quad (2.21)$$

where $\eta = \eta_x$ is the horizontal dispersion function. The dispersion function is defined such that the horizontal position, x , of an individual particle is given by

$$x = x_{co} + x_\beta + \eta_0 \delta + \eta_1 \delta^2, \quad (2.22)$$

where x_{co} is the horizontal closed orbit position of the particle around the storage ring and x_β is the betatron oscillation (perturbation to the horizontal orbit about x_{co}). The vertical dispersion is considered to be negligible because dispersion is predominately in the horizontal plane in which the electron beam is deflected to form a circular path. Vertical dispersion is only generated through misalignments introducing deflections in the vertical direction or transverse coupling, where horizontal dispersion is coupled into the vertical plane from rotated quadrupole magnets. These are less than 1% of the horizontal dispersion at the ASLS.

The manipulation of α_0 and α_1 is achieved through changing the dispersion function η and its non-linear components. To second order, the dispersion function is determined by the differential equations:

$$\eta_0'' + (\kappa + k)\eta_0 = +\kappa \quad (2.23)$$

$$\begin{aligned} \eta_1'' + (\kappa + k)\eta_1 = & -\kappa - \frac{1}{2}m\eta_0^2 + (\kappa^3 + 2\kappa k)\eta_0^2 + \frac{1}{2}\kappa\eta_0'^2 \\ & + \kappa'\eta_0\eta_0' + (2\kappa^2 + k)\eta_0, \end{aligned} \quad (2.24)$$

where k is the quadrupole magnet strength and m is the sextupole magnet strength. In general an analytic solution is not possible due to the discrete nature of the magnets and the dependence on s (i.e., $\kappa = \kappa(s)$, $k = k(s)$, $m = m(s)$). Nonetheless Equations 2.20 to 2.24 show that α_0 is dependent on η_0 , which is determined by the dipole (κ) and quadrupole (k) magnets. α_1 is dependent on both η_0 and η_1 , which is determined by the dipole, quadrupole and sextupole (m) magnets. Given the dipole contribution is fixed, the change in α_0 will come from changing quadrupoles, while α_1 will come from changing sextupoles.

To understand the importance of α_0 and α_1 on the stability of the system, the Hamiltonian that describes the longitudinal dynamics is evaluated. The Hamiltonian is given by,

$$\begin{aligned} \mathcal{H}(\phi, \delta) = & -\frac{\Omega^2}{\cos(\psi_s)} (\cos(\psi_s + \phi) - \cos(\psi_s) + \phi \sin(\psi_s)) \\ & - \omega \left(\frac{\eta_c}{2} \delta^2 - \xi \delta - \frac{\alpha_1}{3} \delta^3 \right), \end{aligned} \quad (2.25)$$

where the conjugate pairs are (ϕ, δ) and the phase slip has been re-defined as $\eta_c = 1/\gamma^2 - \alpha_0$. Figure 2.1 shows a plot of the solution to Equation 2.25 for small values of η_c . The stable fixed points are at cusps while the unstable fixed points are at saddle points. The δ fixed points correspond to solutions satisfying $\dot{\psi} = \frac{\partial \mathcal{H}}{\partial \delta} = 0$, i.e.,

$$\delta_{fp} = \frac{\eta_c \pm \sqrt{\eta_c^2 - 4\xi\alpha_1}}{2\alpha_1} \approx \frac{\eta_c}{2\alpha_1} \mp \left(\frac{\eta_c}{2\alpha_1} - \frac{\xi}{\eta_c} \right), \quad (2.26)$$

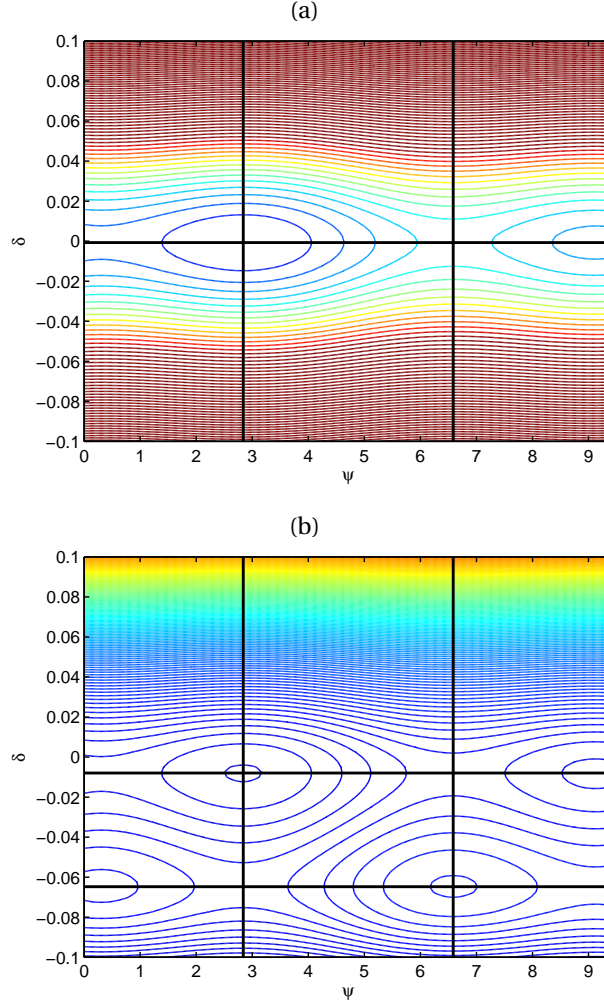


Figure 2.1: Phase space of the system described by the Hamiltonian in Equation 2.25 showing the fixed points for $\xi = 1.5 \times 10^{-6}$, $\alpha_1 = 2.9 \times 10^{-3}$ and $\alpha_0 = 2.11 \times 10^{-3}$ (a) and for $\alpha_0 = 2.11 \times 10^{-4}$ (b). The upper horizontal line in the bottom plot corresponds to the negative solution of Equation 2.26, while the lower horizontal line is the positive solution. The vertical lines are the two fixed points at $\pi - \psi_s$ and $3\pi - \psi_s$. The colour scale represents the total energy of the system, $\mathcal{H}(\phi, \delta)$, and has been kept the same in the two plots and shows a steep local minimum indicating strong longitudinal focusing in (a), compared to a smaller momentum compaction factor in (b).

where the approximation on the right is valid for $\eta_c < 0$. The momentum acceptance can be defined as the separation between the stable and unstable fixed points at $\pi - \psi_s$ and is approximated by $\eta_c/\alpha_1 - 2\xi/\eta_c$. In general the value of ξ does not change by very much. Therefore to reduce the bunch length via η_c , α_1 must be changed to maintain the momentum acceptance in the storage ring. This is essential to maximise the lifetime of the electrons in

the storage ring and to maintain efficiency when adding electrons to the ring from the injection system. Figure 2.1 shows the contours indicating the total energy of the system given by the Hamiltonian, $\mathcal{H}(\phi, \delta)$, for constant α_1 . In general, for constant α_1 , longer bunches and larger values of η_c have a larger momentum acceptance compared to shorter bunches and smaller values of η_c . Figure 2.1 also shows a shift in the equilibrium energy due to a finite value of ξ and a decreasing α_0 .

To determine how α_1 can be controlled, Equation 2.26 is rewritten, thereby allowing the momentum acceptance to be plotted, i.e., the difference in the two δ_{fp} , as shown in Figure 2.2. The horizontal axis shows the reduction factor relative to $\eta_c = -2.11 \times 10^{-3}$ during normal operations at the ASLS. It is reasonable to assume that ξ from Equation 2.19 is mainly determined by the horizontal emittance, ϵ_x , if the closed orbit components are between 10^{-5} to 10^{-6} and the emittance coupling³ is $< 10\%$. For a reduction by a factor of 3 and 100, $\epsilon_x = 100$ nm rad and $\epsilon_x = 190$ nm rad, respectively. Using $\epsilon_x = 100$, $\xi \approx \epsilon_x \langle \gamma_x \rangle \approx 100 \times 10^{-9} \times 3 \approx 10^{-7}$ has been used to calculate the values of $\alpha_{0,1}$ required to keep a reasonable energy acceptance of $\Delta\delta_{fp} \approx 2\%$.

In Section 1.2 we noted that to have a significant enhancement in the far-IR spectrum the bunch length needs to decrease by a factor of 10 relative to the nominal operating regime. From Equation 2.17 this implies a reduction of η_c by a factor of 100. Figure 2.2 shows that α_1 would need to be reduced to a value $< 0.7 \times 10^{-3}$ in order to maintain a modest aperture of 2%.

The longitudinal dynamics and the stable fixed points have been previously examined in References [33, 34, 70] as a function of decreasing η_c . The change in dynamics with decreasing η_c is referred to as a change from the RF bucket to the alpha bucket regime. This regime is so named due to the distinct alpha-like pattern of the phase space plots. The existence of the two stable fixed points (alpha buckets) was first shown experimentally at the National Synchrotron Light Source (NSLS) [71]. Consequently it is possible to double the number of bunches in the storage ring with energies separated by η_c/α_1 and $(\pi - 2\phi_s)/\omega$. A potential application of doubling the number of bunches is the simultaneous generation of “two-colour” photons through a single undulator from electrons with two different energies. Another potential application is to double the number of bunches in a collider to increase the luminosity. However, Heifets [72] showed that the low current thresholds for instabilities, such as the head-tail and sawtooth instability, was too severe a limitation for practical use in colliders and light sources.

In this section we have discussed the longitudinal dynamics of the storage

³For a horizontally planar storage ring with negligible vertical dispersion, the vertical emittance, ϵ_y , is determined by the horizontal emittance coupled into the vertical plane, i.e., $\epsilon_y = c_{emitt} \epsilon_x$.

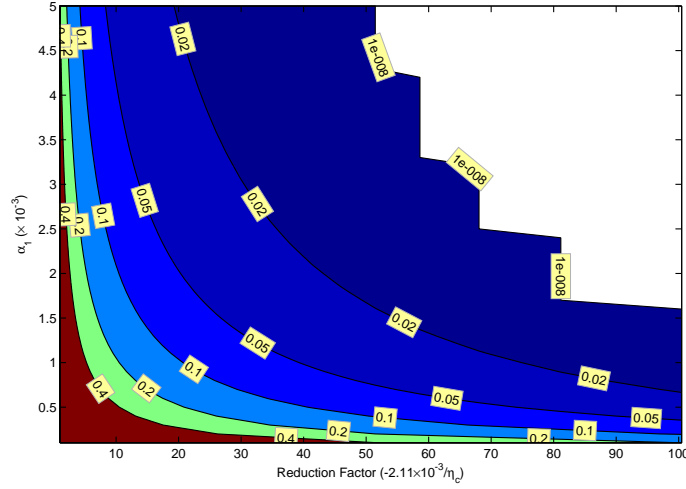


Figure 2.2: Constraints on α_1 to maintain different momentum apertures, $\Delta\delta_{fp}$, for a given $\xi = 1 \times 10^{-7}$. Where the momentum aperture is zero (white areas) there are no solutions and this is an unstable operating point. The horizontal axis shows the reduction factor (relative to $\eta_c = -2.11 \times 10^{-3}$).

ring and have shown that the bunch length can be controlled by manipulating α_0 though quadrupole magnets. The momentum acceptance can be controlled by manipulating α_1 using sextupole magnets. In the next section we outline a method for controlling α_0 and α_1 at the nominal ASLS beam energy of 3 GeV.

2.2 Negative Dispersion Method of Reducing α_0

The ASLS storage ring has three families of quadrupoles to control the two transverse tunes, ν_x and ν_y , and the dispersion, η_x . As noted in the previous section $\alpha_0 = \oint \kappa \eta_x(s) ds$ and to minimise α_0 for a fixed value of the dipole strength, κ , the integral of $\eta_x(s)$ in the dipole should approach zero. For a Chasman-Green type lattice one method of reducing α_0 is to have a negative dispersion in one half of the dipole and positive dispersion in the second half of the dipole. The dispersion function which minimises α_0 is shown in Figure 2.3. This is called the negative dispersion approach.

There are two complications that result from this method. The first is that the large absolute amplitude of the dispersion results in an increased sensitivity to energy or path length changes. From the definitions in Equations 2.18 and 2.22, the change in the horizontal position to first order is given by $\Delta x = \frac{\eta_x \Delta L}{\alpha_0 L}$, where one can consider $\Delta L/L$ as a perturbation term. As a consequence the beam stability, Δx , decreases for the same degree of perturbation as η_x gets larger and α_0 approaches zero. The second issue is the

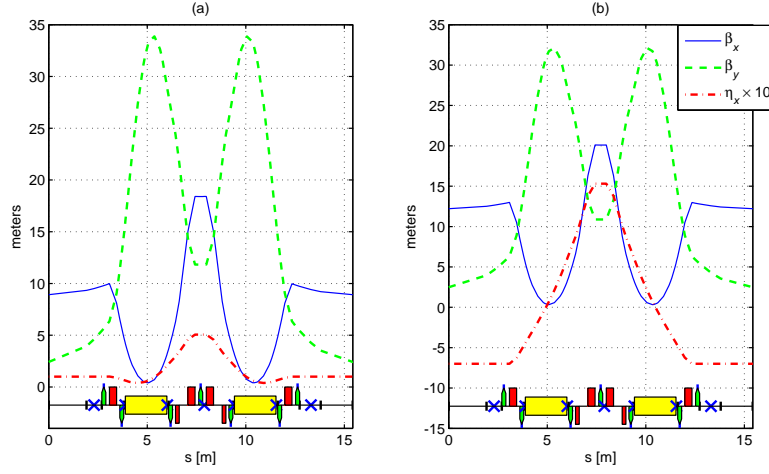


Figure 2.3: One double-bend cell of which there are 14 that make up the storage ring. The elements plotted below the figure are the two dipoles (yellow long rectangles), quadrupoles (red short rectangles), sextupoles (green pentagons), BPMs (crosses) and correctors (vertical blue lines). The standard lattice for user operation (a) and an intermediate low- α lattice for these studies (b) is shown. This method of controlling α_0 ensures that the dispersion integral for the dipole magnet approaches zero.

increased horizontal emittance driven by the larger absolute amplitude of the dispersion function at the dipole. The increased horizontal emittance results in larger horizontal source sizes and decreased brilliance of the source. Unfortunately the reduction in the beam stability and brilliance directly affects the quality of the measurements for users who require short x-ray pulses for time resolved experiments. Users operating in the Far-IR spectrum are less sensitive to changes in the transverse emittance.

An alternative to using negative dispersion is employed at the Diamond light source. This alternative method reduces the momentum compaction factor while maintaining an equivalent emittance, which results in a lattice that is less sensitive to perturbations [44]. The method takes advantage of conditions where the integral of the dispersion parameter is zero, with small values of η_x . These conditions are shown Figure 2.4, where the initial conditions are such that $\eta_x > 0$ and importantly $\eta'_x < 0$. The results were calculated by propagating the dispersion function through a model of the ASLS dipole⁴. In the current arrangement of the magnets with a single strong focusing quadrupole downstream of the dipole, these conditions do not seem possible. A minimisation routine was used to find combinations of

⁴The simulation software used is the Accelerator Toolbox developed in the Matlab environment [73]. This utilises a Forrest-Ruth 4th order symplectic integrator to track the trajectory of particles with a given model [74].

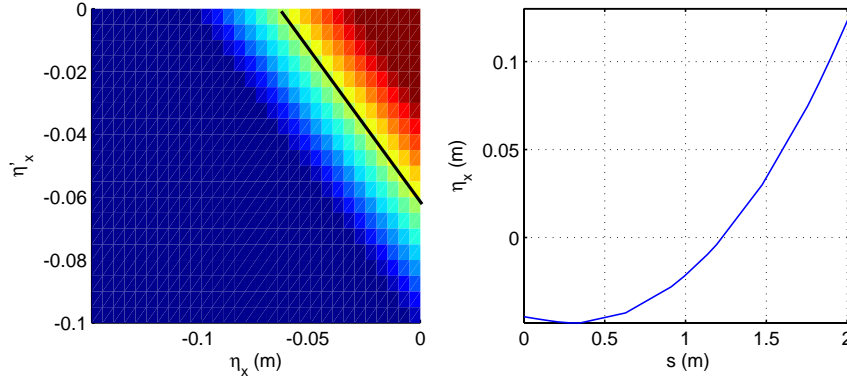


Figure 2.4: Different values of η_x and η'_x (prime denotes the derivative along s), was tracked through a model of the ASLS dipole. The left figure shows a surface plot of $\oint \kappa \eta_x(s) ds$, with the black line indicating where the integral is zero. The right plot shows a typical evolution of the dispersion function for which the integral is zero.

strengths of the quadrupoles that minimise the dispersion and emittance at the same time. Under the conditions that only the magnetic strengths are parameters, no solutions were found. If other parameters, such as the location and type of quadrupole magnets were included it might be possible to find a solution for the ASLS lattice in which a low emittance is maintained. These additional parameters were not considered, since it was not possible to implement this approach due to operational constraints at the ASLS. This strategy will be discussed further in Chapter 6.

In the absence of a low emittance, low alpha lattice, the negative dispersion method was used to reduced α_c . The configuration has been modelled and the parameters are shown in Table 2.1. A plot of the lattice function is shown in Figure 2.3. From here onwards, η_x , shall refer to the value of the dispersion function at the centre of the straight sections on either side of the group of magnets that form a sector.

The control and calibration of the storage ring's dispersion parameter were carried out in two steps. The first step uses a storage ring simulation to predict the changes to the strengths of the quadrupole and sextupole magnets to modify the dispersion while maintaining the transverse tunes and chromaticity. The second step is the standardisation of the magnets at a given dispersion so that it is possible to return to that particular operating parameter repeatably.

In the first step, the strengths of the quadrupoles and sextupoles were calculated using an ideal model and are shown in Figure 2.5. These strengths keep the tunes and chromaticity constant while changing the dispersion to

Table 2.1: Lattice parameters for two configurations, with $\eta_x = 0.1$ m and $\eta_x = -0.75$ m, showing a moderate decrease in the bunch length. The parameters for half the nominal beam energy is also shown to highlight the reduction in bunch length when the energy is decreased.

Parameter	$\eta_x = 0.1$ m	$\eta_x = -0.75$ m	$\eta_x = -0.75$ m
E_0	3.0134 GeV		1.5067 GeV
f	499.66859 MHz		
V_0	3 MV		
h	360		
ν_x/ν_y	13.29 / 5.216		
$U(E_0)$	908 keV		57 keV
δ_{E_0}	1.02×10^{-3}	0.94×10^{-3}	0.47×10^{-3}
ϵ_x	10.3 nm	141.5 nm	35.4 nm
α_0	2.11×10^{-3}	0.468×10^{-3}	0.476×10^{-3}
f_s	14.86 kHz	7.058 kHz	10.223 kHz
$\sigma_{t,z}$	23.0 ps / 6.9 mm	10.1 ps / 3.0 mm	3.5 ps / 1.0 mm

reduce α_0 . The tunes are defined as:

$$\nu_{x,y} = \frac{1}{2\pi} \oint \frac{1}{\beta_{x,y}(s)} ds, \quad (2.27)$$

where the chromaticity is given by $\xi_{x,y} = \Delta\nu_{x,y}/\delta$. These changes were applied as relative changes to the currents driving the magnets assuming that a fractional change in the current equates to the same fractional change in the magnetic field. This is generally true in the linear region of the B-H curve that describes the relationship between the magnetic field and magnetisation force from the current coils. However, one of the families (QFA) just starts to saturate and is no longer in the linear region of the B-H curve. Following the above predictions and scaling the currents in the magnets resulted in tune and chromaticity shifts that made the stored beam unstable. The correction of the tunes uses a tune-dispersion response Jacobian, where the two tunes and dispersion are the observables and the three quadrupole families are the parameters. The Jacobian is given by $\left[\frac{\partial T_i}{\partial k_i^{mag}} \right]$, where $T = [\nu_x, \nu_y, \eta_x]$ and $k^{mag} = [k_{QFA}, k_{QDA}, k_{QFB}]$ ⁵. For the ASLS this is a square and invertible matrix, which is used to control the two tunes and η_x . Although a tune-dispersion response can be measured, in practice, a simulation derived response is sufficiently accurate.

Changing the dispersion also affects the chromaticity, $\xi_{x,y}$, defined as:

$$\xi_{x,y} = \pm \frac{1}{4\pi} \oint \beta_{x,y}(s) (m(s)\eta_x(s) - k(s)) ds, \quad (2.28)$$

⁵“QFA”, “QDA” and “QFB” are three unique families (groups) of quadrupoles in the storage ring at the ASLS.

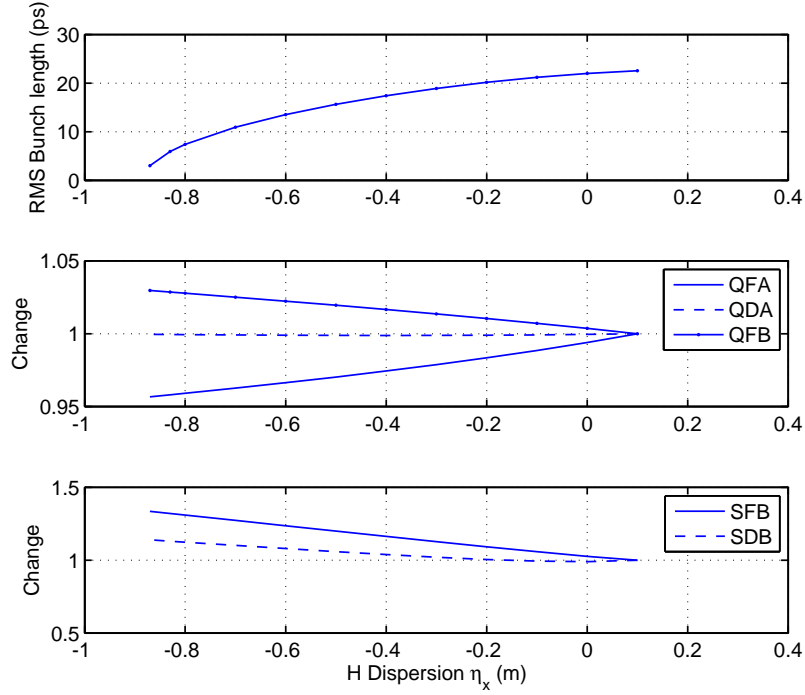


Figure 2.5: The predicted change in the quadrupoles and sextupoles needed to change η_x and reduce the bunch length while keeping the chromaticity at 1.4 (Horizontal) and 6.3 (Vertical). The SFA and SDA families were kept at a strength of $m^{SFA}=15.6 \text{ m}^{-3}$ and $m^{SFA}=-16.6 \text{ m}^{-3}$, respectively. The SFB and SDB families are used to control the chromaticity. The maximum predicted increases were 4% in the quadrupoles and around 40% for the sextupoles.

where $m(s)$ is the strength of the sextupole magnet and $k(s)$ the strength of the quadrupole magnet⁶; the positive value is used for x and the negative value for y . Control of the chromaticity is also important in maintaining beam stability in storage rings [75]. The control of the chromaticity is achieved by using a model to predict the settings required for the sextupoles. Verification of these settings is determined through direct measurements of the chromaticity.

After scaling the quadrupoles to a desired value of η_x , it is necessary to standardise the configuration so that each time it is reinstated the lattice functions are known. In this step the standardisation of the storage ring is done using the Linear Optics from Closed Orbits (LOCO) method [76]. The

⁶Magnet strengths are defined as $k = \frac{1}{B\rho} \frac{d}{dx} B_y [\text{m}^{-2}]$ and $m = \frac{1}{B\rho} \frac{1}{2!} \frac{d^2}{dx^2} B_y [\text{m}^{-3}]$, where $B\rho = 3.3356 \times 10^{-9} \sqrt{E_0^2 - E_e^2} [\text{Tm}]$ is called the beam rigidity constant and E_e is the rest mass of the electron in eV.

LOCO method assumes that a measured orbit response matrix⁷ can be used to create a model that reflects the linear properties of the actual storage ring. In the first step, where families of magnets were adjusted equally as a group, small differences in the strengths of the individual magnets result in a small deviation away from the ideal and breaks the 14-fold symmetry of the lattice design. LOCO is used to calibrate a model to the actual machine using measured orbit response matrices, so that the lattice functions can be extracted and corrections can be calculated to bring the machine closer to the ideal lattice design.

The standardised lower α configuration is used as a known configuration point from which the quadrupoles can be further scaled to change σ_t . In the following sections we will focus on the observations made of the bunch length as η_x is decreased and highlight issues with orbit stability as σ_t is reduced by a factor of 10.

2.3 Results of Low- α Studies at 3.0 GeV

The predicted quadrupole and sextupole strengths shown in Figure 2.5 were used to reduce the bunch length for a beam energy of 3 GeV, while keeping the tunes and chromaticity constant. During the experiment the tunes, chromaticity, synchrotron tune (f_s) and bunch length (σ_t) were measured. It was observed that despite the predictions of the simulations, the tunes would drift as the quadrupoles were changed to reduce the bunch length. Small corrections were made whenever the tunes deviated more than 0.02 from $\nu_x = 0.29$ and $\nu_y = 0.216$. The measurements of f_s and σ_t in Figure 2.6(a) show reasonable agreement with simulations. The change in the gradient below $\eta_x = -0.9$ m occurs because the momentum compaction factor has crossed zero and adopts a negative value.

The measured bunch length in Figure 2.6(b) is slightly longer when compared with the bunch length derived from the model. This is expected because the model does not include any charge dependent effects that elongate (or compresses) the bunch length. The bunch length with charge dependent effects removed is often referred to as the zero current bunch length. The factors that cause a longer bunch length to be measured are chromatic effects in the input optics of the streak camera [77], charge dependent effects, such as the potential wall distortion (PWD) [37, 78], and single bunch instabilities. The details on how the bunch length is measured and the factors that affect it will be discussed in Chapter 3.

⁷An orbit response matrix is a Jacobian matrix of the closed orbit (at the beam position monitors around the storage ring) as a function of the strength of the individual steering magnets.

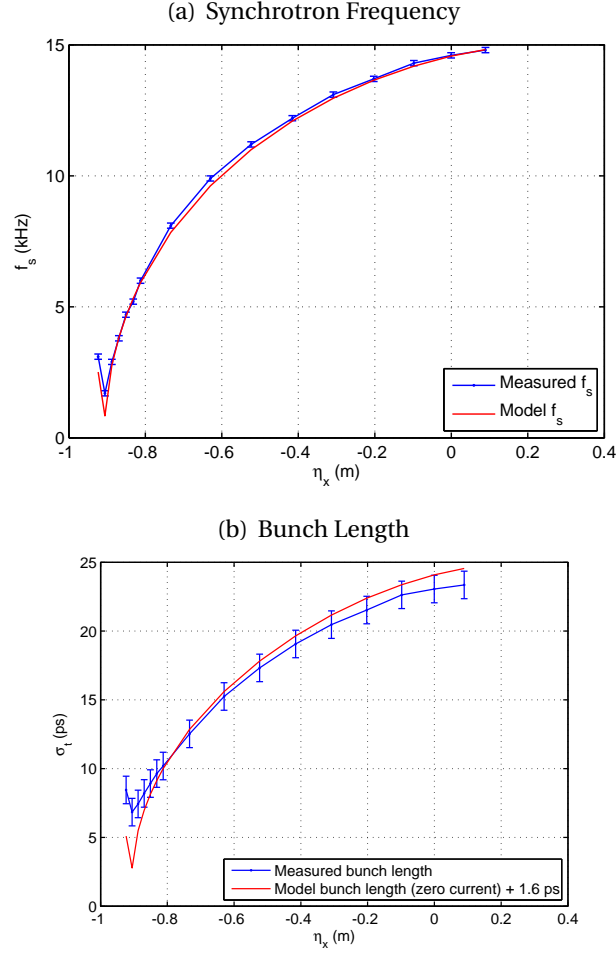


Figure 2.6: The measured synchrotron frequency, f_s , and bunch length, σ_t , is compared to model predictions. In (a) there is reasonable agreement between the measurements and the model predictions. In (b) the zero current bunch length from the model includes an offset of 1.6 ps to account for chromatic effects in the optics of the streak camera.

Measurements shows that at longer bunch lengths there is a linear relationship between σ_t and f_s , as implied by Equation 2.16. The model predicted gradient was 1.55 ps/kHz, while the measured gradient for bunch lengths greater than 12 ps was 1.64 ps/kHz. The difference of 6% is significant, but the origin of this discrepancy is unclear. It was intended to conduct a more careful study with lower charge per bunch to minimise current dependent distortions; however, the streak camera used for bunch length measurements failed and this measurement could not be repeated. For shorter bunches the relationship is no longer linear and current dependent bunch lengthening starts to occur.

Although the true bunch length is current dependent, f_s can be used

to determine the zero current bunch length, provided certain parameters are known. When scaling the quadrupoles to manipulate α_0 , a calibration cycle using LOCO is usually required to determine the true dispersion of the machine and hence the true value of α_0 . However, as suggested by Equation 2.15 an alternative to determining α_0 is possible by noting that f_s is proportional to $1/E_0$, U_0 , V and α_0 . Knowing E_0 , U_0 and V then gives a direct relation between f_s and α_0 . The energy loss, U_0 , can be calculated from the simulation of the storage ring, and to a good approximation is $f_s \propto U_0^{1/4}$. E_0 and V can be measured from the nominal operating configuration, where η_x has been calibrated using LOCO to be 0.1 m. Using the nominal configuration, the measurements gave $f_s = 14.848$ kHz, $E_0 = 3.0134$ GeV and $\alpha_0 = 2.11 \times 10^{-3}$ (the latter two measurements were made implementing the spin depolarisation method at the ASLS [79]). This gives an effective cavity voltage of $V = 2.9937$ MV that is applied to the electron beam. When scaling the quadrupoles to manipulate α_0 , the values of E_0 , U_0 and V do not change and therefore f_s can be used as a measure of α_0 in the storage ring.

As the bunch length is reduced to <10 ps the position stability decreased and oscillations in the horizontal closed orbit of greater than $350 \mu\text{m}$ were observed at the smallest bunch lengths. The use of synchrotron radiation for Far-IR spectroscopy requires a source with a constant intensity for periods of up to 20 minutes for high resolution scans. Therefore an investigation was conducted into the source of the perturbation on the beam orbit.

2.3.1 Beam Orbit Stability

Decreasing the momentum compaction factor increases the sensitivity to perturbations in the accelerator system [66]. With a smaller momentum compaction factor, changes in the path length give rise to changes in the relative momentum, δ . The perturbations that change the path length can come from magnetic fields or modulations in the RF frequency or phase. Such changes in the momentum translate into transverse motion due to the horizontal dispersion function, $\eta_x(s)$ (the vertical plane dispersion, $\eta_y(s)$, is only a few percent of the horizontal component).

This effect was clearly observed at $f_s = 1.2 \pm 0.3$ kHz corresponding to $\alpha_0 = 1.8 \times 10^{-5}$, or a factor 117 smaller than the nominal value. At this bunch length, large peak-to-peak oscillations in the horizontal closed orbit were observed with the BPMs. These orbit deviations occur with a 50 Hz period as shown in Figure 2.7. The horizontal dispersion function is evident in the observed orbit deviation in the storage ring. This suggests that this perturbation is causing the energy of the beam to oscillate at a frequency of 50 Hz (mains frequency). At $\alpha_0 = 1.8 \times 10^{-5}$, a 1 Hz change in the RF frequency

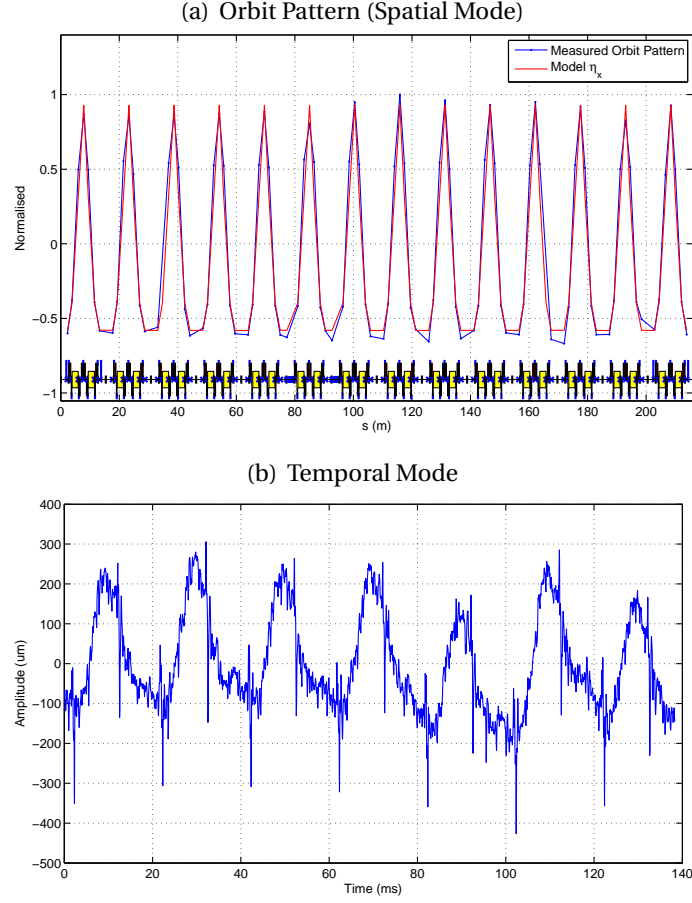


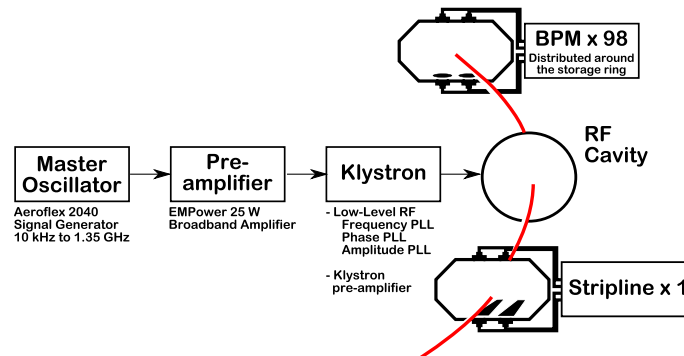
Figure 2.7: The beam position is sampled at 21 kHz at every location where there are BPMs in the storage ring. 3000 samples of the beam position from all the BPMs are used to create a 2D matrix. The principal eigenvectors of the 2D matrix is calculated using Singular Value Decomposition. (a) The dominant pattern (eigenvector along the BPM direction of the matrix) created by the oscillating beam around the storage ring. This pattern matches the dispersion orbit of the beam when there is a deviation in energy. (b) The dominant temporal mode (eigenvector along the temporal direction of the matrix) about which the pattern in (a) oscillates.

will cause a change in the horizontal orbit of $196 \mu\text{m}$ according to

$$\Delta x = \eta_x \frac{\Delta f}{\eta_c f_{rf}}. \quad (2.29)$$

Therefore a measured peak-to-peak horizontal orbit deviation of $350 \mu\text{m}$ gives a possible peak-to-peak RF frequency change of 1.8 Hz at a rate of 50 Hz. This corresponds to a fractional energy change of $\delta_E = (\Delta f / f) / \alpha_0 = 2.0 \times 10^{-4}$. Changes to the beam energy can arise from changes in the path length due to increasing or decreasing integrated vertical magnetic fields. Numerous measurements were made of the dipole power supply, which showed that the

Investigation into sources of the perturbation considered the RF system. A schematic of the layout of the RF system is shown in Figure 2.8. In Figure



2.9 the top two traces show the spectral components taken from BPM data in the horizontal plane for two operational modes. The low alpha mode at $f_s = 5.2$ kHz shows the beam motion with many different frequencies, which correlate with BPM and stripline measurements taken during normal operation at $f_s = 14.8$ kHz. The measurements in Figure 2.9 indicate that the noise on the beam is present during normal operation. Transitioning to low alpha makes the noise more pronounced on the electron beam. A clear correlation is observed when the spectra from the BPMs and stripline (top three traces in Figure 2.9) are compared with the spectrum from voltage probes in the RF cavities (bottom red line in Figure 2.9). This indicates the RF system makes a significant contribution to the noise observed on the beam.

Further investigation showed that an amplifier between the Klystrons and the master oscillator is the source of the noise. The measured spurious frequencies from the pre-amplifier is evident as side-bands on the RF frequency at a level of -85 dBc⁸. A test of two different amplifier units showed sidebands at slightly different frequencies, but at approximately the same

⁸dBc is a scale relative to the amplitude of the centre frequency measured in dB. The EMPower 25W pre-amplifier with spurious sidebands at -85 dBc is within its specification (less than -70 dBc). Working in collaboration with the engineers it was possible to reduce these sidebands to a level below the noise floor of < 95 dBc. This modification was implemented after the experiments reported in this thesis.

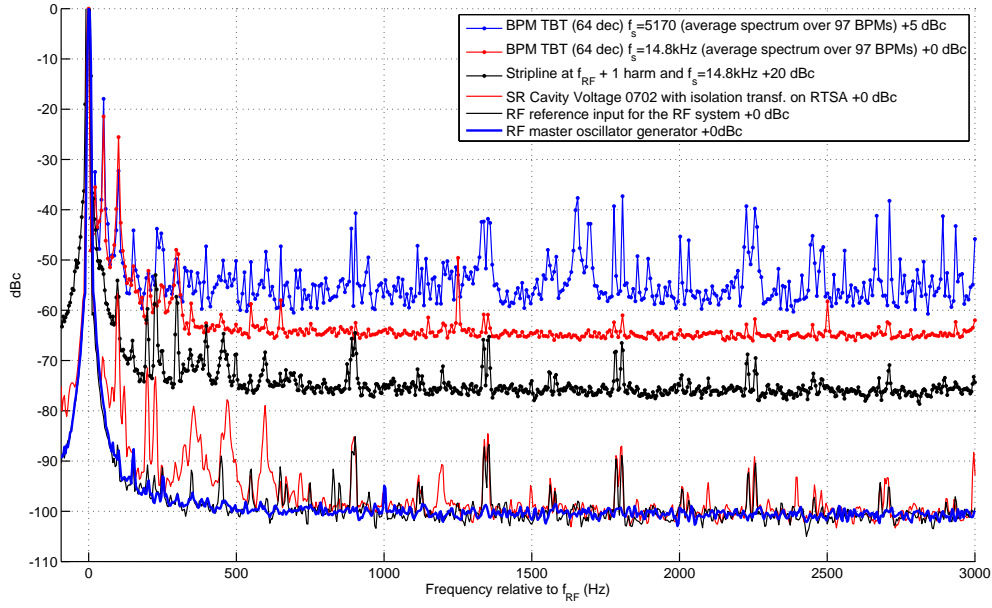


Figure 2.9: At smaller values of α_0 many peaks are observed in the spectrum which arise from noise in the RF system. A comparison with measurements made during normal operations ($f_s = 14.8$ kHz) shows similar spectral components in the beam motion. The components were observed on the stripline BPMs both at the RF harmonic of 500 MHz and at the first revolution sideband. The measurement of the RF cavity voltage also exhibits similar spectral components.

amplitude. Changing the amplifier is still an option if shifting the sidebands is necessary; however, since the pre-amplifier is a critical sub-system for the facility, careful testing is required before replacing it.

The spectrum from the cavity voltage measurements indicates that the RF system itself also contributed to the noise. Again most of the spurious frequencies have values less than -70 dBc, with the exception at 100 Hz, which has an amplitude of -55 dBc. Identifying the actual element in the RF system that generates the noise is non-trivial and was considered to be an unacceptably high risk to normal operations at the ASLS. However, the information gathered here has clarified the sources of noise previously observed at the ASLS.

After removing the spectral components generated by the RF system from the spectrum measured with the stripline and BPMs, the 50 Hz and 300 Hz frequencies are still unaccounted for. The 50 Hz noise is likely caused by stray electromagnetic fields from circulating currents in the metallic elements in the storage ring. Investigations by colleagues at the ASLS now leads us to conjecture that the source of the 50 Hz noise is a 16 kV 3-phase AC mains feed that is used by the RF system and dipole power supply. These

cables run along trays on the roof of the storage ring tunnel and are not shielded. Measurements show that the cable trays are coupling to the AC lines and generate 50 Hz currents as high as 9 A. These currents may also flow along much of the metallic structures in the storage ring tunnel generating electromagnetic fields that perturb the beam. The source of the 300 Hz, which is a couple of orders of magnitude smaller than the 50 Hz, is most likely due to the power supplies themselves. Trials are ongoing to manage the 50 Hz noise; however, at the time of writing of this thesis this is unresolved.

Our investigation has highlighted many sources of noise and in the case of the 50 Hz component there is little that can be done, apart from implementing a feedback system to actively correct the orbit. It was fortunate that later experiments with the IR beamline showed that as long as the frequencies are well defined and fixed, the noise it introduces in the data can be managed. Ultimately to improve the global stability, an orbit feedback system is required. Such a system is currently being designed at the ASLS by the author; however, this is not the focus of the current thesis and is yet to be completed.

As discussed previously, controlling α_1 is as important as controlling α_0 . Under certain conditions, involving large α_1 values, synchrotron oscillations on the order of millimetres are observed. As shall be shown in Chapter 4 these large oscillations are a result of longitudinal head-tail instabilities. The measurement and control of $\alpha_{0,1}$ is discussed in the following section.

2.3.2 Measuring α_0 and α_1

It has been shown in the previous section that maintaining the momentum acceptance⁹ in the storage ring requires the control of α_1 when α_0 is reduced. If the momentum acceptance is not maintained, the lifetime¹⁰ of the electron beam in the storage ring decreases. Upon rearranging Equation 2.16 and substituting $\eta_c^2 = \alpha_0^2 + 4\alpha_1 \frac{\Delta L}{L}$ and $\frac{\Delta L}{L} = -\frac{\Delta f}{f}$, the following linear relationship is obtained:

$$\nu_s^4 = a + b \frac{\Delta f}{f}, \quad (2.30)$$

where $\nu_s = f_s / f_{rev}$ is the synchrotron tune and f_{rev} is the revolution frequency. The constant and gradient terms are used to derive α_0 and α_1 as follows:

$$\alpha_0 = \sqrt{a} \frac{2\pi E_0}{hqV_0 \cos \psi_s} \quad (2.31)$$

$$\alpha_1 = -\frac{b}{4} \left(\frac{2\pi E_0}{hqV_0 \cos \psi_s} \right)^2. \quad (2.32)$$

⁹The momentum acceptance is the largest value of δ that an electron can have in the storage ring. Particles with larger values are unstable and cannot be retained in the storage ring.

¹⁰The lifetime is defined as $I(t) = I_0 \exp(-t/\tau_b)$, where τ_b is the lifetime of the electron beam. Longer lifetimes are desirable in storage ring light sources.

The values of α_0 and α_1 are calculated by measuring the change in v_s as a function of $\Delta f/f$, together with calibrated values for V_0 , E_0 and ψ_s determined from simulations. The synchrotron frequency is measured by performing a spectral analysis on the transverse motion of the electron bunch.

The spectrum analyser used for these measurements is a Tektronix Real-Time Spectrum Analyser (RSA3308A) with a bandwidth from DC to 8 GHz. The measurements are shown in Figure 2.10. A signal from a single stripline BPM (a 15 cm long copper strip in the vacuum chamber) was used in the same transverse orientation as that of the button BPMs. The long copper strip gives a stronger signal compared to the small round button-like probe. A simple schematic of the experimental arrangement is shown in Appendix B.2.

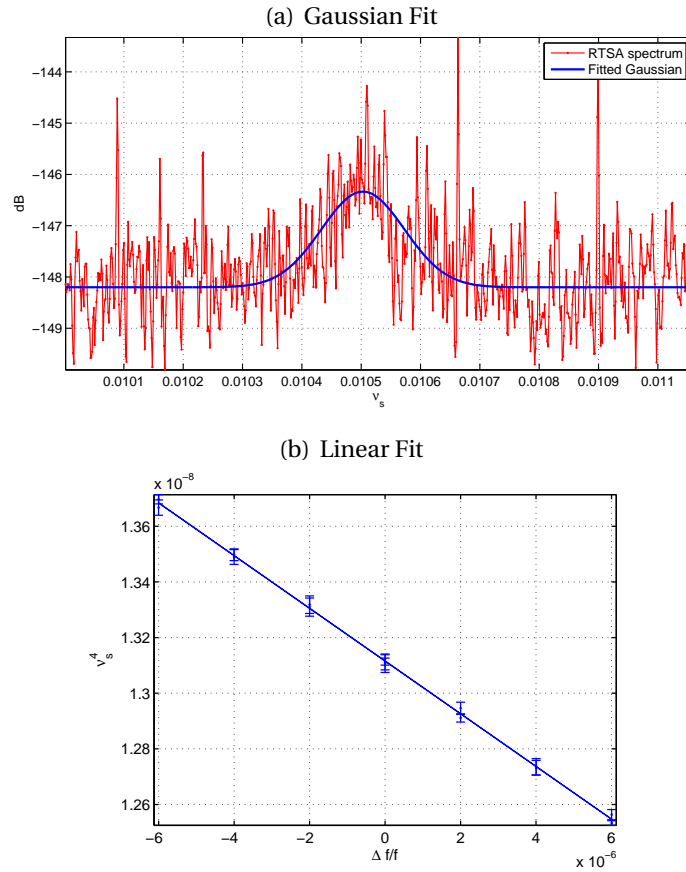


Figure 2.10: (a) The averaged data from the RSA (red line) and the Gaussian fitted profile (blue line). (b) Change in v_s^4 as a function of $\Delta f/f$ with the associated error bars given by $4v_s^3\sigma_{v_s}$, where σ_{v_s} is the standard deviation calculated from five separate RTSA measurements. The linear fit gives two coefficients that relate directly to $\alpha_{0,1}$.

Another way of measuring the synchrotron frequency is via the BPM

electronics that are used to monitor the transverse position of the electron beam. A schematic of this arrangement is shown in Appendix B.1. It is able to sample the beam position at the revolution frequency of 1.389 MHz and output data at 21.867 kHz. As the phase information at a BPM is not available, the resulting bandwidth for this data is 10.844 kHz, with a nominal resolution of 7.2 Hz for 3000 samples. Measurements taken with the BPM and the spectrum analyser connected to a stripline BPM are shown in Figure 2.11. Both data sets show similar features, especially in the vicinity of the synchrotron frequency at 5.3 kHz. The sampling frequency of the BPM is locked to the

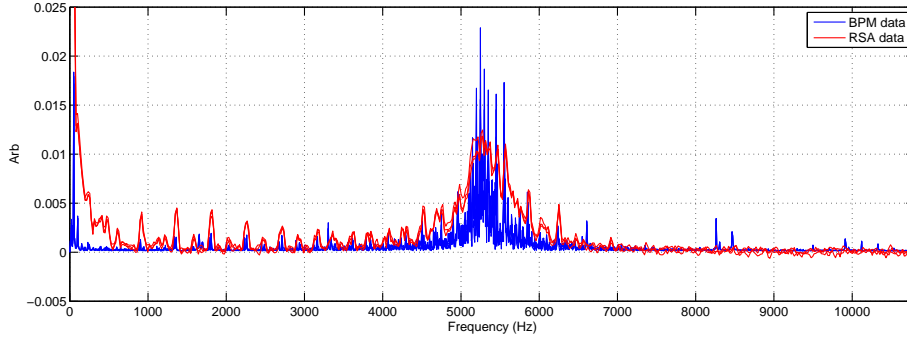


Figure 2.11: FFT of turn-by-turn data decimated by 64 samples and averaged over 97 individual BPMs is compared with measurements taken on a RSA connected to a single stripline. Three different data sets were taken using both methods. All the spectral plots have been normalised. Both exhibit similar features as a function of f_s , including noise from the RF system at 900 Hz, 1300 Hz and 1800 Hz. This gives confidence in using the BPM for measurements of $\alpha_{0,1}$ when $f_s < 10$ kHz.

revolution frequency of the storage ring, bringing any sidebands at the RF frequency down to baseband (DC). Therefore as the RF frequency is changed, the same data can be measured and used to determine the synchrotron frequency for different RF frequencies - as required when measuring α_1 . Data acquired using the BPM is three times faster than data acquisition with the spectrum analyser, due to overheads in the data collection of the latter instrument.

Five spectra were collected and averaged to estimate the uncertainty in the measurement of the synchrotron frequency. The spectral data showing the synchrotron frequency from the RSA is broad and noisy (see Figure 2.10(a)). Therefore, a simple peak search does not give an accurate measurement of the synchrotron frequency. To determine this frequency, the data from the RSA was fitted with a Gaussian function using the width, centre-of-mass, amplitude and amplitude offset as parameters. The centre-of-mass parameter is then used as the measured synchrotron frequency. To get α_1 , the synchrotron frequency was measured for different f_{rf} . Using least squares, a

line was fitted to $v_s^4 = (f_s/f_{rev})^4$ versus $\Delta f/f$, where the coefficients are related to $\alpha_{0,1}$ using Equation 2.32. The standard error in the least squares fit is used as the uncertainty for $\alpha_{0,1}$.

2.3.3 Measured and Modelled $\alpha_{0,1}$

Although measuring $\alpha_{0,1}$ is straightforward it would still be useful to be able to make predictions of these parameters based on the settings of the sextupoles from a simulation of the storage ring. Simulated values of $\alpha_{0,1}$ were derived through numerical tracking of particles using the Accelerator Toolbox [73]. The tracking algorithm uses the particle's position and momentum $(x, p_x, y, p_y, \delta, ct)$, relative to the ideal path, where p refers to the momentum, δ and t are the relative energy and time deviation from the ideal path, and c is the vacuum speed of light. The starting point is a closed orbit solution for the lattice with $\delta = 0$, giving $(x^0, p_x^0, y^0, p_y^0, 0, 0)$. Adopting $(x^0, p_x^0, y^0, p_y^0, \delta^0, 0)$ for some $\delta^0 > 0$ and tracking the particle's trajectory after a single revolution of the storage ring gives $(x^1, p_x^1, y^1, p_y^1, \delta^1, ct^1)$. The momentum compaction factor is therefore $\alpha_c = \frac{\Delta L}{\delta L} = \frac{c\Delta t}{\delta L}$. By comparing $c\Delta t$ for different δ -values it is possible to numerically determine $\alpha_c(\delta)$. Fitting the polynomial coefficients to first order allows the simulated values of $\alpha_{0,1}$ to be calculated. To verify if the storage ring simulation is accurate, measurements of $\alpha_{0,1}$ were made for different configurations of sextupoles and dispersions.

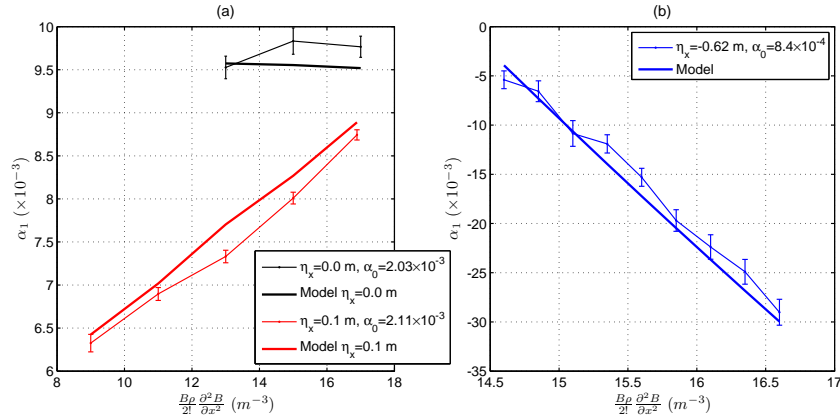


Figure 2.12: The change in α_1 as a function of the sextupole settings for different α_0 , determined by measuring the change in Δf_s with $\Delta f/f$. The data is split into plots (a) and (b) for convenience. There are four families of sextupoles, one of which was varied; two other sextupoles were adjusted to keep the chromaticity constant at $\xi_x = 2$ and $\xi_y = 4$, and the fourth family was kept constant.

Figure 2.12 shows the linear dependence of α_1 on a sextupole in the long straight section (referred to as SFA). For Figure 2.12(a) the discrepancy is

caused by magnetic hysteresis in the sextupoles, where the same magnetisation force from a current coil results in different magnetic fields. For these measurements the order in which the data were collected corresponds to sextupole strengths¹¹ of 11.0 m^{-3} , 9.0 m^{-3} , 13.0 m^{-3} , 15.0 m^{-3} , followed by 16.9 m^{-3} . When the current was increased to measure 13.0 m^{-3} , 15.0 m^{-3} and 16.9 m^{-3} , the actual strength of the sextupole is weaker than expected due to the coercivity of the magnet. If the data at 13.0 m^{-3} , 15.0 m^{-3} and 16.9 m^{-3} are shifted to lower values to reflect the effect of the magnetic hysteresis, a better fit with the model would have been possible. This is also observed in Figure 2.12(b).

These results show that hysteresis in the sextupole magnets can contribute an error of $\Delta\alpha_1 = 0.5 \times 10^{-3}$. Therefore to ensure that the low alpha configurations have well defined values of α_1 , standardisation of the sextupoles¹² is necessary [80]. Although simulations can be used to estimate the sextupole settings for a desired α_1 , measurements are still required to determine the actual value.

2.4 Summary

This chapter has reviewed the salient equations needed to understand longitudinal beam dynamics. From these equations it is clear that a reduction in the bunch length can only come from decreasing E_0 or α_0 . In this thesis we will only investigate the low alpha mode of operation. The analysis of the longitudinal dynamics showed the importance of minimising α_1 , since α_0 is decreased for very small bunches [81]. To achieve small bunch lengths the negative dispersion method was introduced and issues of stability were highlighted using experimental studies. Unfortunately our investigations showed that there is little that can be done to ameliorate beam stability. The method used to measure and set α_1 was also introduced and experimental data were acquired to demonstrate the efficacy of the technique, while highlighting the importance of standardising the magnets to ensure that the operational modes of the storage ring are reproducible.

The experiments so far have used simulations of the storage ring to explore how the bunch length can be optimised. In reality, the longitudinal distribution of the electrons will change due to charge dependent effects. In Chapter 3 the dependence of the bunch length and onset of the instabilities

¹¹The strength is defined as $\frac{1}{B\rho} \frac{1}{2!} \frac{\partial^2 B_y}{\partial x^2}$. The strength is changed by altering the current in the coils of the magnet.

¹²This requires the magnets to be cycled from the minimum to maximum values a few times before settling on the desired operating current. By following this procedure it is possible to accurately reproduce the desired magnetic field.

with increasing charge will be investigated. In Chapter 3 we will also show how CSR is generated in quasi-periodic bursts when the instabilities occur. In Chapter 4 an analysis of the CSR will show that a large non-zero value of α_1 maximises the intensity of bursts of CSR. This contrasts with the requirement of minimising α_1 when using short bunches (1 ps and under) to generate a constant source of CSR.

Bunch Length Measurements and Charge Dependent Effects

During normal operations the charge distribution of the electron bunch at the ASLS has $\sigma_t = 23$ ps. In low alpha operation this can be reduced to a few picoseconds. One method of determining the charge distribution is to measure the duration of the synchrotron radiation as the electrons pass by using a streak camera. A streak camera is used to measure the temporal profile of short optical pulses by converting the optical signal into electrons via a photocathode. The electrons are accelerated through a streak tube onto a micro-channel plate (MCP) that amplifies the electron signal. The back end of the MCP is attached to a phosphorescent screen to convert the electrons into photons to be imaged by a cooled CCD camera. To get the temporal information, the electrons travelling through the streak tube are swept in one direction very quickly so that the temporal distribution is “smeared” along one of the transverse axes. A schematic of the operation of the streak camera is shown in Figure 3.1. A secondary sweep can also be used to map the change in the temporal structure over different time scales. The streak camera used in the Optical Diagnostic Beamline (ODB) is an Optronis Optoscope SC-10 with a 250 MHz synchroscan module and a temporal resolution of 2 ps. This module takes the RF frequency and divides it by two so that it is synchronous to the bunch structure in the storage ring. A secondary sweep, with fast sweep rates (660 ps/mm up to 100 ns/mm) and slow sweep rates (100 ns/mm to 5 ms/mm) is also available. The synchroscan unit is a resonantly tuned circuit so that the electric field of a pair of plates oscillates at 250 MHz (half the RF frequency). In a single period, the fields will sweep two bunches onto the screen and by appropriate delays of this sweep it is possible to “smear” the odd bunches on the top part of the screen, while the even bunches are “smeared” along the bottom of the screen. The plots captured by the streak camera represent time along both axes.

The first step in measuring the bunch length with a streak camera is to determine the calibration factor that converts the transverse screen pixel

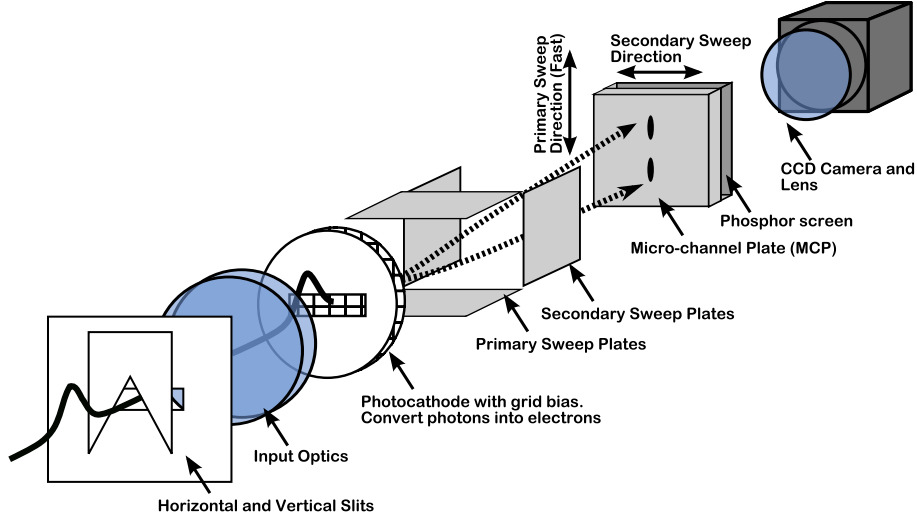


Figure 3.1: The streak camera converts the photon pulses into electrons on the photocathode and uses an electric field to sweep the pulses of electrons onto a microchannel plate (MCP) with a phosphor screen readout. This process translates the temporal distribution into a vertical distribution along the MCP, which then generates an image on the phosphor screen that is captured using a CCD camera.

dimension into time. The calibration of the synchroscan sweep rate was carried out using a ps pulsed laser, triggered by an external signal at 1kHz, which was synchronised to the master oscillator. This trigger is generated from the timing system and is an integer fraction of the RF frequency used in the storage ring, which is set at $f = 499.6738$ MHz. The pulse passes through a delay block consisting of a 19.9 ± 0.1 mm (BK7 with $n_r = 1.5187$ at 550 nm) beam splitter cube with two mirrors, so that part of the optical pulse is split and delayed by a fixed amount determined by the size of the beam splitter cube. Figure 3.2 shows the design and function of the delay block. The expected time delay between the primary and delayed pulse is $2 \times 19.9 \text{ mm} \times 1.5187/c = 201.6 \pm 1.0$ ps.

The calibration of the delay block was achieved by adding a delay¹ in the flight path from the laser to the streak camera. By tracking the peaks of the two pulses over 3 different intervals it is possible to calculate the total additional flight path required, so that the delayed pulse overlaps with the initial position of the primary pulse on the screen of the streak camera. Using this method the measured delay between the pulses was found to be $199.0 \text{ ps} \pm 7.2 \text{ ps}$ (3.6%). Given the known delay between the pulses the internal delay on the camera was changed to move the pair of pulses across the screen.

¹The micrometer stage used to adjust the delay can add up to 32 mm (106.7 ps) to the flight path.

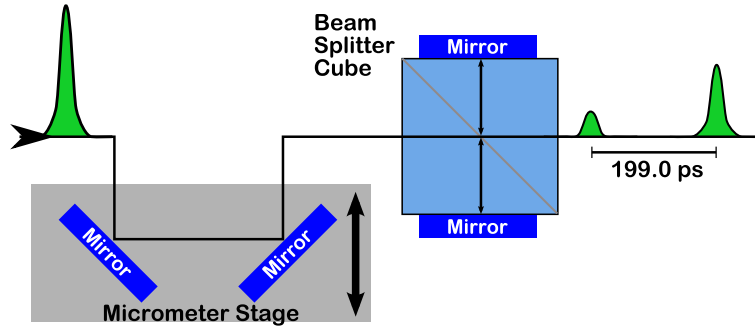


Figure 3.2: The delay block consists of a 50-50 90° beam splitter cube (BK7 $n_r = 1.5187$ at 550 nm) sandwiched between two mirrors. The primary pulse travels through the beam splitter followed by an internally reflected pulse that is expected to be delayed by $(2 \times 19.9\text{mm} \times 1.5187)/c = 201.6$ ps. The micrometer stage is used to measure the delay between the two pulses and was found to be $199\text{ ps} \pm 7.2\text{ ps}$ (3.6%).

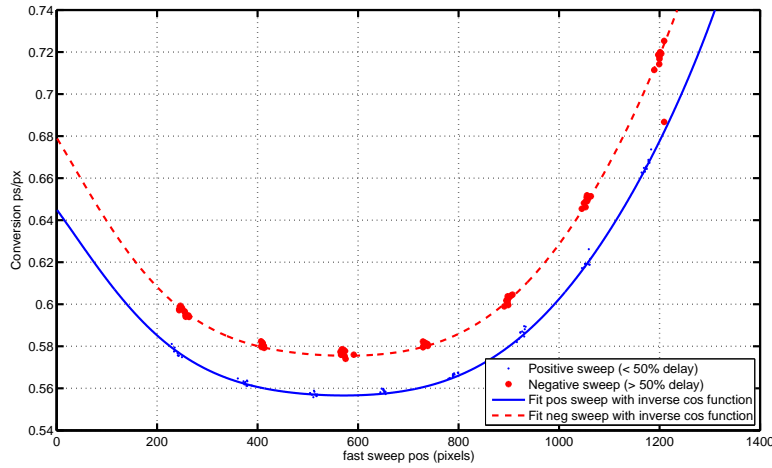


Figure 3.3: Calibration of the streak camera along the fast axis with a sweep rate of 50 ps/mm. An outlier at 1200 pixels was not used in the fit.

The distance between the pulses, measured in pixels, can be converted to a calibration factor of ps/pixel for a particular location on the screen. In Figure 3.3 the calibration was carried out with the following settings: sweep rate was set to 50 ps/mm, the intensifier was set to 700 V and the secondary sweep was set to 100 ns/mm. The fitted calibration curve for a sweep rate of 50 ps/mm has an RMS uncertainty of 0.2%. Therefore, the major contribution to the uncertainty is the calibration of the delay block (3.6%). It is important to note that there is a difference in the calibration factors between the positively and negatively swept bunches. This means that the positive sweep speed is different to the negative sweep speed. To apply the correct calibration

factor, the sweep direction needs to be known during the measurement. A calibration curve for a sweep rate of 25 ps/mm was also measured.

To confirm the calibration, measurements of the bunch length for the standard storage ring configuration were made. The streak camera was set to a sweep rate of 25 ps/mm (primary), 100 ns/mm (secondary) and a gain of 700 V. A plot of one of the data sets is shown in Figure 3.4, where the long oblong is an electron bunch train for one revolution around the ring. Only 300 of 360 bunches were filled, consequently there are gaps observed in Figure 3.4. The data was integrated between the vertical black lines between 570 and 600 pixels. To determine the sweep direction the internal delay

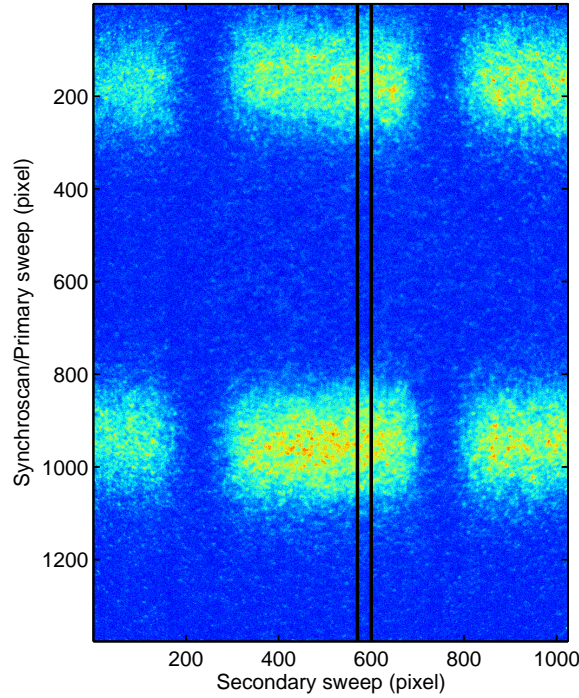


Figure 3.4: Data set showing the electron bunch train for each revolution (600 pixels on the horizontal axis). The upper row of bunches was collected on the negative sweep showing odd numbered bunches and the lower row of bunches was collected on the positive sweep showing even numbered bunches. In this measurement only 300 of the 360 possible bunches are filled, leading to gaps at pixel number 200 and 750 on the horizontal axis. The gaps indicate the location of the 60 unfilled bunches. Knowing which sweep corresponds to which row is important as there is a 3% difference in the conversion factor as shown in Figure 3.3.

was changed and the direction in which the bunches moved on the screen was recorded. If the bunches move along the pixel axis (towards the top of

the image) then the bunch was captured on the positive sweep. If it moves anti-parallel to the pixel axis then it is captured on the negative sweep.

In addition to applying the calibration factor, the use of refractive lenses in the input optics has been shown to introduce chromatic effects that increase the measured bunch length [77]. A discussion of how this aberration contributes to the bunch length measurement can be found in Appendix B.3. To calculate the effect of this aberration, two measurements were taken - with and without a 10 nm laser line bandpass filter around 510 nm. The results of a fit with 20 samples show a measured bunch length of 25.4 ± 0.3 ps without the bandpass filter and 23.8 ± 0.7 ps with the filter. The chromatic aberration therefore increases the measured bunch length by 1.6 ps. The increase in the uncertainty arises from the significant reduction in the intensity due to the bandpass filter. As long as the spectral content of the incoming photons and the optical elements remain the same, the chromatic effect will smear the measured bunch length by an additional 1.6 ps.

Having calibrated and accounted for the contribution from chromatic aberrations, current dependent bunch lengthening [82] needs to be considered when comparing measured and simulated bunch lengths. At the ASLS storage ring with 3 MV cavities and an electron energy of 3 GeV, the simulated bunch length is 22.9 ps. When bunch lengthening effects, such as the potential well distortion, are considered, a single bunch with a current of 0.64 mA will grow to a bunch length of 23.25 ps. The prediction from simulations compares well with the measured value of $\sigma_t^{meas} = 23.8 \pm 0.7$ ps for a single bunch with a current of 0.64 mA. The source of the potential well distortion is discussed in the next section.

3.1 Current Dependent Bunch Lengthening

The discussion of longitudinal dynamics did not take into account particles that couple to and distort the fields in the RF cavities. This results in a distortion of the charge distribution in a self consistent way and is called the potential well distortion effect [37, 78]. The longitudinal charge distribution is determined in part by the fields of the RF cavity. A change to the charge distribution will perturb the RF field and this in turn affects the charge distribution. Therefore the problem of determining the equilibrium charge distribution will include a self-interaction term via the RF field. A solution to the problem is given by the Haissinski equation [46], written in the form [82]:

$$n(t) = K \exp \left(-\frac{t^2}{2\sigma_0^2} + \frac{1}{V'\sigma_0^2} \int_0^t V_{ind}(t') dt' \right), \quad (3.1)$$

where $n(t)$ is the normalised charge distribution function, K is a normalisation constant, σ_0 is the zero current equilibrium bunch length in the presence of a fixed potential, $V' = -(\omega/c)V \cos \psi_s$ is the voltage gradient at ψ_s and the induced voltage is given by:

$$V_{ind}(t) = \int_0^\infty W^\parallel(t')n(t-t')dt', \quad (3.2)$$

where W^\parallel is a longitudinal wakefield determined by the geometry of the vacuum chamber profile in the ring (in units of $\text{VC}^{-1}\text{s}^{-1}$). By convention, $t \leq 0$ is the head of the charge distribution. The wake function is a measure of the induced voltage seen by trailing particles at a distance t' away from the generating particle with unit charge. Depending on the environment of the electrons, the fields generated by the passage of the electrons will be different. The wake function is an average effect over a single revolution in the storage ring. For highly relativistic electrons Equation 3.2 is a single-sided convolution, because the wakefield in “front” of the electrons is zero.

There are different models that can be used to approximate the wake function. In our analysis a simple broadband impedance model has been chosen, where the wake potential, V_{ind} , is modelled by:

$$V_{ind}(t) = -cq [Rn(t) + cLn'(t)]. \quad (3.3)$$

Here a prime denotes differentiation with respect to s , q is the total charge in a single bunch, R is the real component of the ring impedance and L is the ring inductance. This impedance model was chosen because there is a clear distinction between purely resistive and inductive components. The resistive component results in a net energy loss for the electron beam due to the wakefields, while the inductive component contributes to a symmetric broadening of the charge distribution. Two different measurement techniques are used to fit R and L separately, thereby producing a better estimate of the impedance of the storage ring.

Equation 3.1 can be solved by a Newton iterative method, where an initial distribution, $n_i(t)$, is used to get the next iterate $n_{i+1}(t)$. The solution is found when $n_i(t)$ converges to an equilibrium solution, i.e., $\Delta n(t) \rightarrow 0$.

The real resistance, R , results in an energy loss given by²:

$$\Delta E = k^\parallel q, \quad (3.4)$$

where

$$k^\parallel = \frac{1}{2\pi} \int_{-\infty}^{+\infty} |N(\omega)|^2 \text{Re}Z^\parallel(\omega) d\omega \quad (3.5)$$

² ΔE is measured in units of eV.

is the loss factor, $N(\omega)$ is the Fourier transform of $n(t)$ and Z^{\parallel} is the longitudinal complex impedance. The energy of the electron beam in a storage ring is changed by using electric fields generated in RF cavities and is equal in value to the change in the cavity voltage ΔV when measured in units of eV, i.e., $\Delta E = \Delta V$. Using $\Delta V = V_0 \cos(\psi_s) \Delta\psi$, Equation 3.4 can be rearranged to give:

$$\Delta\psi = \omega \Delta\tau = \frac{k^{\parallel} q}{V_0 \cos(\psi_s)}, \quad (3.6)$$

where V_0 is the maximum cavity voltage, $\Delta\psi$ is the phase shift required to get ΔV , ω is the RF frequency and $\Delta\tau$ is a shift in time. Assuming a longitudinal Gaussian distribution of constant width, given by the zero current bunch length³ σ_t^0 , and a constant R , Equation 3.5 can be simplified to:

$$k^{\parallel} = \frac{R}{2 \sqrt{\pi} \sigma_t^0}. \quad (3.7)$$

Combining Equations 3.6 and 3.7 a relationship between R and $\Delta\tau$ is found, i.e.,

$$\Delta\tau = \frac{Rq}{\omega 2 \sqrt{\pi} \sigma_t^0 V_0 \cos(\psi_s)}. \quad (3.8)$$

Therefore the real resistance, R , can be determined by measuring $\Delta\tau$ for a single bunch with different q . This method follows Reference [82], where a group of low current single bunches is used as a reference phase. A single bunch is added to the storage ring and the phase shift is measured between the single bunch and the reference on a streak camera as a function of current. The results presented in Figure 3.5 show that for a given α_0 the local gradient is constant as the current in the single bunch is increased. Using Equation 3.8 and the fitted gradients in Figure 3.5, R can be derived and is shown in Table 3.1.

With measured values of R , the inductance, L , can be fitted by measuring the evolution of the bunch length with single bunch current using a streak camera. Figure 3.6 shows the bunch length measurements made with a streak camera at different values of α_0 . Fits based on the Haissinski equation were calculated by varying σ_t^0 and L until the evolution of the fitted sigma of the Haissinski distribution agreed with the measurements made with the streak camera. The resulting fits for σ_t^0 and L are shown in Table 3.1.

As the distribution is calculated for higher current densities a threshold is eventually reached, beyond which the solution to the Haissinski equation does not converge. Above this threshold the iterated distribution shows an

³ α_0 was changed in a simulation of the storage ring until the synchrotron frequency, f_s , agreed with the measured value. The zero current bunch length was then calculated using this simulated value.

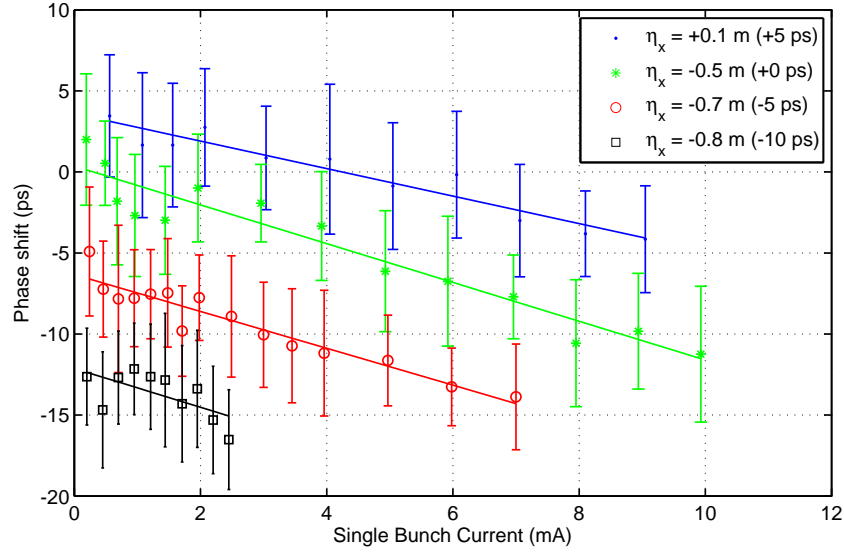


Figure 3.5: The phase shift of a single bunch, relative to low current bunches, was measured at different α_0 . The plots have been offset in order to observe differences in the gradients.

Table 3.1: Using measured R values, the Haissinski equation was solved to fit the inductance, L , and zero current bunch length, σ_t^0 . There is good agreement between the modelled bunch length σ_t^{model} and σ_t^0 . I_{th} is the current beyond which the Haissinski solutions do not converge. The asterisk denotes a predicted value of I_{th} for $\eta_x = -0.75$ m, where the R and L values are linearly extrapolated. Single bunch measurements show good agreement with these predicted values of I_{th} .

η_x	α_0 (10^{-3})	σ_t^{model} (ps)	σ_t^0 (ps)	R (Ω)	L (nH)	I_{th} (mA)
+0.10 m	2.11	23.1	22.8	866 ± 85	34.0	-
-0.50 m	1.15	16.2	15.8	856 ± 73	16.0	11.0
-0.70 m	0.62	11.6	11.7	582 ± 51	10.0	8.0
-0.75 m	0.48	10.1	-	510*	10.0*	4.8*
-0.80 m	0.33	8.3	8.4	439 ± 189	10.0	2.4

oscillating density profile as the equation is solved. An example of such an oscillating density profile is shown in Figure 3.7. When the density profile does not converge, this is an indication that the density distribution is susceptible to instabilities. Although modelling the ring impedance with just R and L in Equation 3.3 is simplistic, the use of measured data to fit the impedances captures sufficient information to predict when the charge distribution becomes susceptible to instabilities. Measurements of the instability threshold in the following chapters demonstrate the accuracy of this approach.

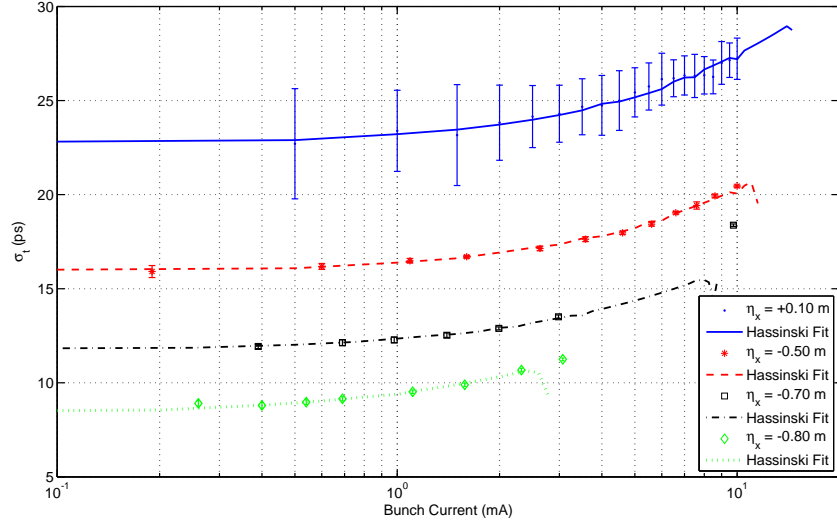


Figure 3.6: Line plots showing the bunch lengthening due to potential well distortions for different values of α_0 . The resistance was fixed at $R = 1600 \, \Omega$, and inductance, L , was fitted to the measured data. The error bars for $\eta_x = +0.1 \, \text{m}$ are larger because a band pass filter was used to remove chromatic aberrations, which also reduces the signal. In the other plots no filter was used and a value of $1.6 \, \text{ps}$ was subtracted from the measurements to account for the chromatic aberrations.

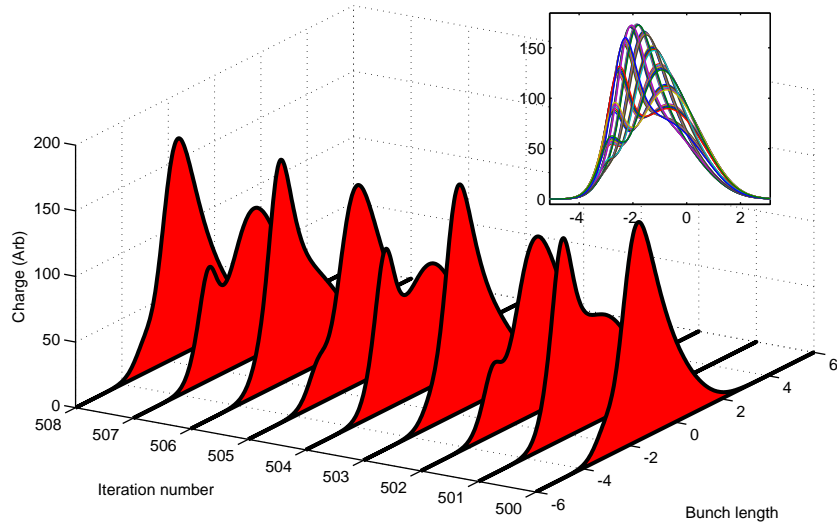


Figure 3.7: Non-equilibrium solution to the Haissinski equation showing that the distribution does not converge. This occurs when the current threshold is exceeded for a given set of values of σ_t^0 , R and L in Equation 3.1.

3.2 Enhancement of the Radiation in the Far-IR Spectrum

In the previous section we showed that it was possible to control α_0 to reduce the bunch length and observe charge dependent lengthening. To characterise the Far-IR spectrum and observe any enhancement in the photon flux, measurements were carried out on the High-Resolution Far-IR beamline (henceforth called the IR beamline). Electrons were stored in the storage ring configured for $\eta_x = -0.75$ m. Injecting into the storage ring at lower values of η_x decreased the capture efficiency due to a smaller momentum acceptance. When the desired beam current is stored, the injection system is turned off and η_x is manipulated to increase or decrease α_0 .

The IR beamline uses a Bruker IFS125HR instrument, which is an interferometric spectrometer with a $75\ \mu\text{m}$ multilayer beam splitter and a liquid helium cooled Si bolometer [83]. The spectral response of this particular setup is shown in Figure 3.8 in which the background measurement has a local maximum at $30\ \text{cm}^{-1}$. The source of the radiation exhibits a black body spectrum originating from the elements in the detector itself. The spectral response is characteristic of the type of beam splitter that is used in the instrument. As η_x was controlled to reduce α_0 , measurements of the synchrotron frequency were used to determine the expected zero current bunch length.

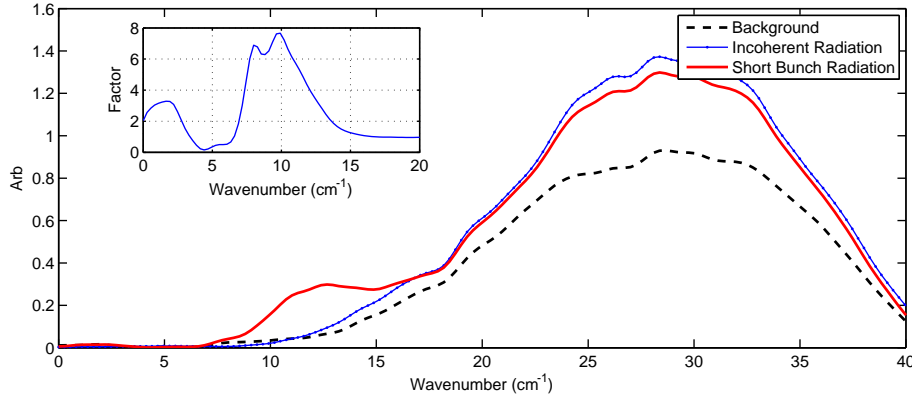


Figure 3.8: Response of the instrument is measured with the mirror retracted (no synchrotron radiation). The detector measures the black body radiation originating from the instrument itself. The blue envelope shows the signal with 15 mA of stored beam in 300 bunches under standard operating conditions before decreasing the bunch length. In short bunch operation we observe emission between $10\ \text{cm}^{-1}$ and $15\ \text{cm}^{-1}$. The increase is a factor of 6 above the incoherent component of the radiation (shown in the inset). The horizontal axis is in units of wavenumbers (cm^{-1}) and the vertical axis is the strength of the signal at the bolometer in arbitrary units.

No change in the spectra from the IR beamline was observed until $f_s \approx 1.3$ kHz was reached, or $\alpha_0 \approx 1.6 \times 10^{-5}$. Scaled against a nominal bunch length of 23 ps at 14.8 kHz the estimated zero current value is $\sigma_t \approx 2$ ps. The increase in intensity in Figure 3.8 is only a factor of 6 within the spectral range of 9 cm^{-1} to 10 cm^{-1} . Using Equation 1.2 the predicted bunch length that will give a factor of 6 increase in signal at 13 cm^{-1} is 1.8 ps, which is in agreement with the measured results. Further attempts to decrease the bunch length did not produce further enhancement.

This approach to reducing the bunch length may be limited by the large horizontal orbit deviations, generated by the line frequency noise and $|\alpha_1| > 0$. As shown in Section 2.3.1, at $f_s \approx 1.3$ kHz the estimated energy perturbation is $\delta \approx 2 \times 10^{-4}$. Control of α_1 was not maintained during the measurements and it increased to 0.013, which resulted in $\Delta\alpha_0 = 1.6 \pm 0.3 \times 10^{-5}$. To achieve $f_s = 0.9$ kHz and $\sigma_t \approx 1$ ps would have required $\Delta\eta_x = -0.003$ m to reduce α_0 to 0.6×10^{-5} . This value of α_0 is on the order of the observed perturbations. Even if α_1 was controlled to better than 1×10^{-3} , the required change in the dispersion ($\Delta\eta_x = 0.003$ m) necessitates control of the dispersion to 0.5%, which is at the limit of the calibration accuracy for the storage ring. Therefore it is unlikely that σ_t can be compressed to much less than 1 ps at the current ASLS energy of 3 GeV and cavity voltage of 3 MV. The other possibility is to reduce the ring energy from 3 GeV to 1 GeV, which for $\alpha_0 = 1.6 \times 10^{-5}$ can potentially reach $\sigma_t = 0.34$ ps with a cavity voltage of 3 MV.

Since there is no stable emission mode at 3 GeV, the investigation turned to using the burst mode of operation. To excite the single bunch instability and produce bursts of CSR, a single bunch with currents ranging from 1 mA to 10 mA is stored in the storage ring. In the following measurement the IR spectrum in the Far-IR was measured as the single bunch current accumulated from 5.5 mA to 9.2 mA. The measured synchrotron frequency of 5200 Hz corresponded to $\eta_x = -0.82$ m. The IR spectra measured at different single bunch currents are shown in Figure 3.9. In burst mode the enhancement was observed for frequencies between 10 cm^{-1} and 20 cm^{-1} , peaking at 13 cm^{-1} . The amplitude of the peak is proportional to I^2 , as expected for coherent emission with a current threshold of 3.7 mA. Measuring the intensity at $I > 9.2$ mA was not possible as the detector saturated even at the lowest gain settings. Figure 3.10 shows the corresponding interferogram with quasi-periodic bursts of coherent radiation creating a sawtooth-like pattern. The Fourier transform of the interferogram shown in Figure 3.9 gives the Far-IR spectrum. The sampling rate of the spectrometer is 20 kHz, giving only five data points with which to define the burst profile. To better delineate the burst profile the output from the bolometer was connected directly to an oscilloscope (see Figure 3.10). The observed profile is indicative of the

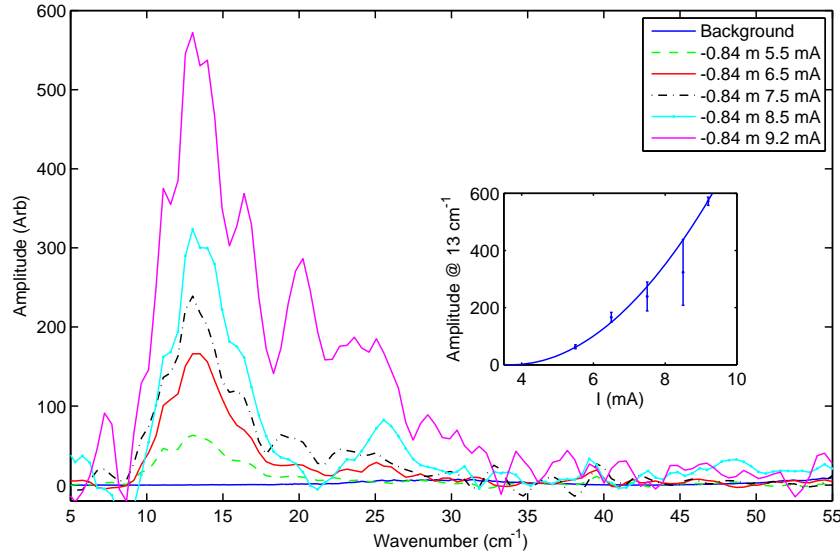


Figure 3.9: Signal measured between 10 cm^{-1} and 20 cm^{-1} for different single bunch currents. The peak is observed at 13 cm^{-1} . The background noise ($> 35\text{ cm}^{-1}$) was observed to increase with increasing current. The peak amplitude was observed to fluctuate by 10% of the mean value, necessitating averaging to minimise the effect of the fluctuations on the spectral measurements. The inset shows the amplitude at 13 cm^{-1} , which increases as the square of the single bunch current, I^2 (starting at 3.7 mA). The larger errors at 7.5 mA and 8.5 mA are a result of detector saturations because the gain had been set too high. This was not noticed at the time the data was taken. The resolution of the scan is 1 cm^{-1} .

sawtooth instability also seen at other storage rings [50, 51].

The interferogram also shows a slower modulation of the overall intensity as well as differences in the peak amplitudes at irregular intervals. The same irregularities in the peak amplitudes were observed on the oscilloscope. Therefore it is a real effect not related to the sampling rate of the spectrometer. The irregular fluctuations add spurious frequency peaks to the spectra and increase the overall measurement noise. Taking the peak amplitude and dividing by the standard deviation at 13 cm^{-1} allows us to calculate the signal-to-noise ratio (SNR). At 5.5 mA and 6.5 mA the SNR is 10, whilst at 9.2 mA it is 40^4 . During normal operation (without CSR), the SNR is 4 due to the very small signal amplitude. The best SNR during normal operation is 150 at the peak response of the detector. The increased flux from CSR has improved the SNR at 13 cm^{-1} . The higher the SNR the less averaging is required to resolve the absorption peaks in the spectra.

In order to improve the stability of the source for the IR beamline it is

⁴The SNR at 7.5 mA and 8.5 mA are not calculated since the detector saturates because the gain was set too high causing the signal to clip. Consequently, the amplitude of the calculated spectra exhibits large fluctuations.

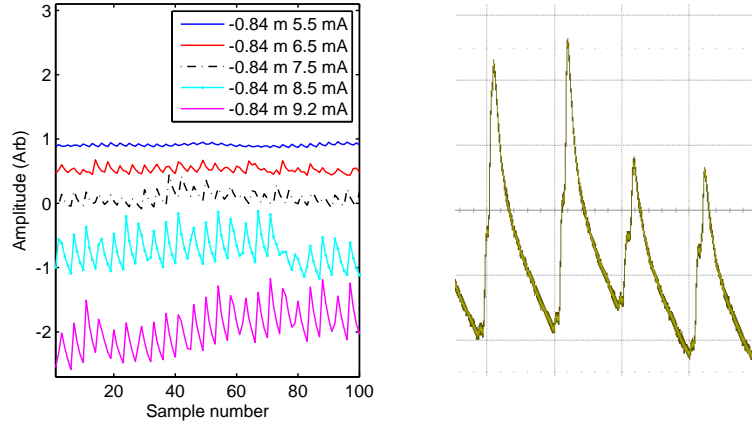


Figure 3.10: Sawtooth pattern in the interferogram from the spectrometer data (left). The signal from the detector was also displayed on an oscilloscope (right). The oscilloscope shows a 2 ms period for the bursts, with the intensity varying considerably between bursts. The observed decay is due to the response of the detector. The burst period is comparable to the detector response. This leads to the integration of the signal from the detector causing the output of the detector to fluctuate as a function of the burst intensity and frequency.

necessary to understand the mechanisms behind the bursts of CSR. Further, it is important to understand how the beamline works and the characteristics of the detector. The next section describes the IR beamline and the detector characteristics.

3.3 Far-IR High Resolution Beamline

The Far-IR High Resolution beamline uses a Bruker IFS-125 Fourier Transform (FT) IR Spectrometer. Where other spectrometers use a tunable narrow bandwidth radiation source to measure the absorption spectra of a material, Fourier transform spectroscopy uses a broadband source. A schematic of the instrument is shown in Figure 3.11. The spectrometer has a beam splitter that splits the radiation into two parts - towards a fixed mirror and a moving mirror. As the mirror moves the recombined intensity is given by:

$$I_{det}(\delta_x) \propto \int_{-\infty}^{+\infty} E^2(k) e^{ik\delta} dk, \quad (3.9)$$

where $I_{det}(\delta_x)$ is the measured intensity at the detector, $E(k)$ is the magnitude of the electric field, $k = 2\pi/\lambda$ is the wavenumber and $\delta_x = x_x - x_1$. $I_{det}(\delta_x)$ is measured by moving one of the mirrors to change δ and is the interferogram. By taking the Fourier transform of $I_{det}(\delta_x)$ it is possible to extract $E(k)$, which

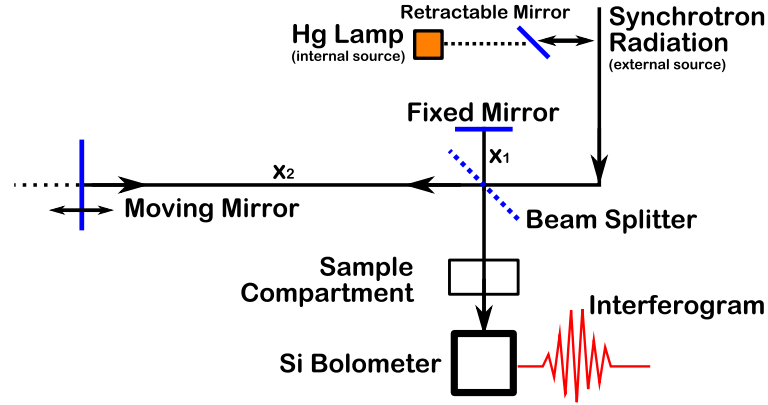


Figure 3.11: Schematic of a Fourier Transform spectrometer. The frequency range over which the spectrometer detects the signal depends on the optical properties of the beam splitter and the bolometer. As the scanning mirror moves, frequency dependent constructive and destructive interference occurs, which results in changes to the intensity at the bolometer. The intensity fluctuation as a function of the mirror position is the interferogram. The Fourier transform of the interferogram gives the frequency spectrum of the observed radiation. x_1 and x_2 are the distances between the beam splitter and the fixed and moving mirror, respectively.

is the spectrum of the radiation. The range of k depends on the optical properties of the beam splitter, i.e., the frequencies where different materials are transparent define the range of k . For Far-IR, Mylar (PET) films are used as beam splitters. Our beamline experiments are mostly carried out with a $75\ \mu\text{m}$ thick Mylar film as a beam splitter with a long wavelength cut-off at 1 mm. Some of the later experiments use a $125\ \mu\text{m}$ thick Mylar film with a longer cut-off approaching 2 mm.

FT measurements require a source of radiation with a constant intensity. Any perturbation in the source intensity during measurements will affect the interferogram. Since the Fourier transform of the interferogram gives the spectrum, a fixed frequency modulation of the source intensity will appear as a narrow peak in the spectrum, while a sudden spike in the source intensity will add features across many different frequencies.

The detector used to measure the intensity of the IR radiation is a bolometer, which is sensitive to very small temperature changes. When exposed to IR radiation the detector absorbs photons and the corresponding increase in the temperature changes the resistivity of the detector. By measuring the change in the resistivity, the incident photon power can be determined. A schematic of a bolometer is shown in Figure 3.12 [84]. To have the required sensitivity to detect small signals (down to nW) the detector is cooled to liquid Helium temperatures of 4.2 K. The response time of the detector is given by the detector time constant, $\tau_D = C_D/G_D$, where C_D is the heat capacity of

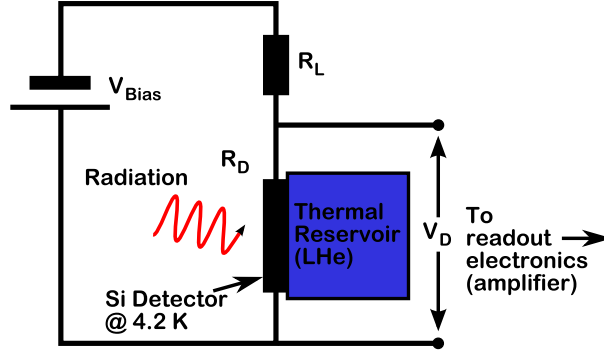


Figure 3.12: Schematic of a bolometer. The incident radiation causes a change in the temperature of the silicon substrate (detector). The detector is cooled in a 4.2 K liquid He bath. Temperature changes affect the detector resistance, R_D , and hence change V_D for a given bias voltage V_{bias} . The load resistor is denoted by R_L .

the detector and G_D is the thermal conductance of the detector. For weak signals, a larger τ_D is needed to increase the integration time.

The Far-IR beamline uses an IR Labs Hi-Res 4.2K bolometer operating with a Silicon detector cooled to 4.2 K. The detector is designed with a low thermal conductance of $0.3 \mu\text{W/K}$, a longer time constant of $\tau_D = 1/(2\pi 200) = 0.8 \text{ ms}$ (200 Hz low pass filter) and a sensitivity of $6 \times 10^5 \text{ V/W}$. To simulate the output of the detector to a modulating source we use:

$$I(t) = A(t)[1 + \sin(2\pi f(t))] \quad (3.10)$$

$$f(t) = f_{osc}[1 - 0.01 \sin(2\pi 40t)] \quad (3.11)$$

where $f(t)$ is the burst frequency (modulated by 1%), f_{osc} is the average of the burst frequency and $A(t)$ is the amplitude of the burst. The intensity function, $I(t)$ is then convolved with the decay profile of the detector, which is given by $g(t) = \exp(-2\pi 200t)$. The results for three different burst frequencies are shown in Figure 3.13. At $t = 30 \text{ ms}$ and $t = 70 \text{ ms}$ the amplitude of the bursts increases then decreases by 15%, respectively. The slower response of the detector tends to smooth oscillating signals to their average value. The results show that changes to the amplitude of the bursts will appear as jumps in the average intensity recorded by the detector. The plots show that the frequency modulation appears as a modulation of the intensity when the burst frequency exceeds the decay rate of the detector at 200 Hz. Therefore in those cases where the burst frequency is greater than 200 Hz, both changes in the intensity and burst frequency have to be minimised.

To determine the underlying burst of CSR that gives the sawtooth pattern in Figure 3.10, the temporal profile of the bursts needs to be measured. This requires an IR detector that has a response greater than 1 MHz to

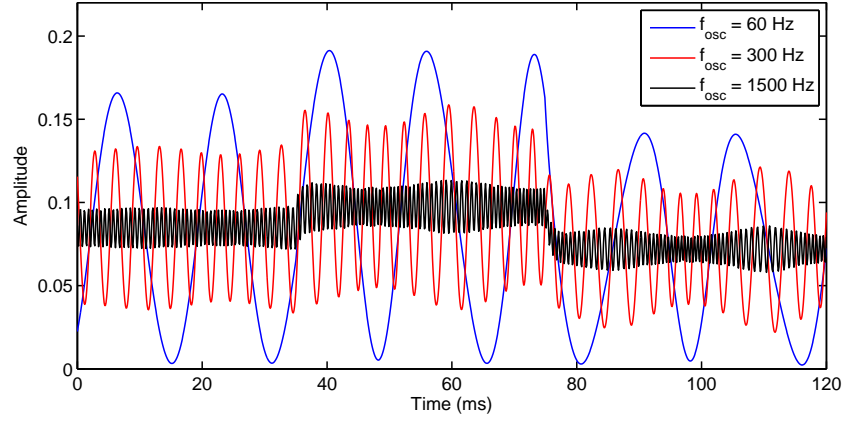


Figure 3.13: Simulation of the output from a bolometer for a periodic signal oscillation (oscillation frequency of f_{osc}). The simulation models both the frequency modulation of f_{osc} by 1% and jumps in the amplitude of the bursts by 15%. The bursts are convolved with the modelled response of the bolometer to calculate the expected output.

ensure that the bursts are sampled accurately. In the next chapter we present measurements of the temporal structure of the bursts and show how they evolve as a function of the storage ring parameters.

Time Structure of CSR Bursts at 3 GeV

To measure the temporal nature of the bursts, a detector with a faster response time than the bolometer is required. Room temperature solid state detectors for millimetre wavelength radiation ($<10 \text{ cm}^{-1}$) based on Schottky diodes are commercially available and are ideal for this application. The detector used in our experiments is a DET-10 from Millitech that has a spectral sensitivity of 2 V/W for frequencies $75\text{-}100 \text{ GHz}$ (2.5 cm^{-1} to 3.3 cm^{-1}). The detector is sensitive to changes in the microwave signal at frequencies up to one GHz when terminated with a 50Ω load. These detectors are used at the Diamond Light source [85] for similar applications. The set-up is shown in Figure 4.1, where a retractable mirror reflects the microwaves perpendicular to the normal optical path and out through a high density polyethylene (HDPE) window to the diode detector. With the mirror retracted the photons proceed along their original path to the interferometer and bolometer.

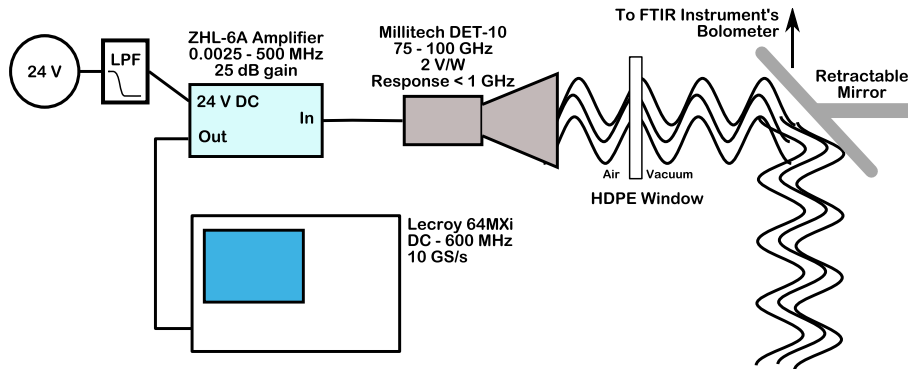


Figure 4.1: Set-up of the 100 GHz detector with an amplifier and oscilloscope.

The storage ring was set up with the measured tunes of 0.292 (Horizontal) and 0.225 (Vertical), chromaticity of 2 (H) and 9 (V) and the sextupoles magnets SFA and SDA set to the strengths of 12.2 m^{-3} and -14.0 m^{-3} , respectively. In this configuration the measured f_s was 8.6 kHz. Based on a simulation

of the storage ring, the predicted values are $\eta_x = -0.67$ m, $\alpha_0 = 0.71 \times 10^{-3}$ and $\alpha_1 = 12.0 \times 10^{-3}$. Figure 4.2 shows bursts of CSR when the single bunch current is 10.8 mA. In this instance the period between bursts is 0.9 ms and each burst at 100 GHz lasts about $150 \mu\text{s}$.

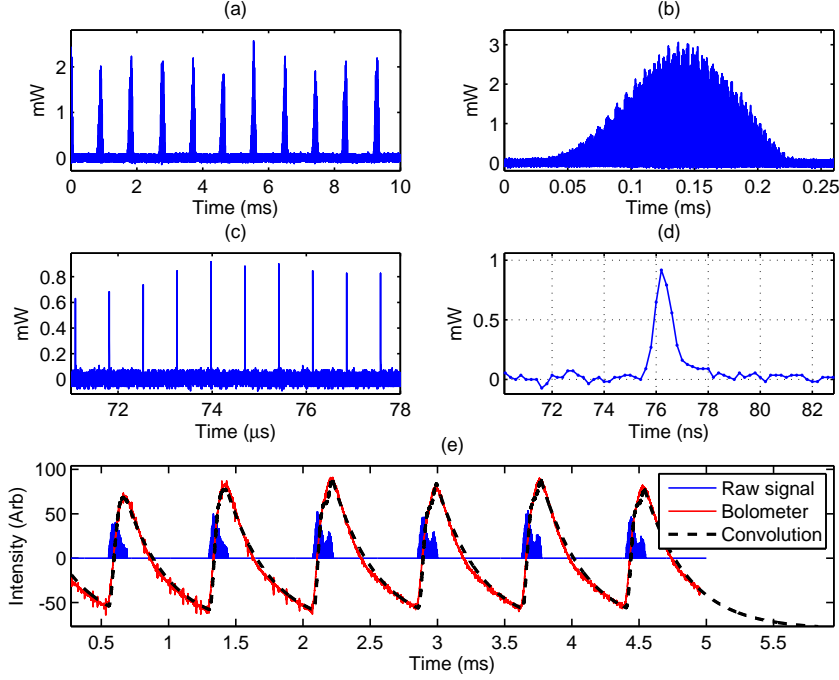


Figure 4.2: Bursts of CSR shown with different time scales. A diode detector with an output response of 1 GHz was used and the detector output was measured on a 600 MHz (10 GS/s) oscilloscope. The vertical axis shows the integrated power over a spectral range of 75 GHz to 100 GHz. Plots (a) and (b) show CSR bursts with a duration of around $150 \mu\text{s}$ and a periodicity of about 1 ms. (c) A CSR burst is made up of signals from a single bunch in the storage ring. (d) The signals have a FWHM of 1 ns, repeating at the revolution period of 720 ns. (e) Simulated response of the bolometer with an exponential decay function (0.75 ms decay time) convolved with the measured detector signal. The decay time is in good agreement with the expected bolometer decay time of 0.80 ms (see Figure 3.13). The results also show some structure at the leading edge due to the discrete nature of the signal, replicating features that were observed with the bolometer.

The rise and decay times of a CSR burst observed with the fast detector is different to those measured with the bolometer (see Figure 3.10). However, if the measured data from the fast detector is convolved with an exponential decay function to mimic the response of the bolometer, the result should simulate the expected output of the bolometer. The result of the convolution agrees well with the measured signal from the bolometer. Therefore the

differences in the outputs of the fast detector and the bolometer are due to the difference in response times. This comparison is shown in Figure 4.2(e). Furthermore the decay time of 0.75 ms used in the exponential function to mimic the response of the bolometer is also in good agreement with the expected bolometer decay time of 0.80 ms. When the period of the bursts, T_{burst} , is less than or equal to the response time of the bolometer, T_{bolo} , the bolometer does not have time to recover before the next signal arrives, resulting in integration of the signal. As discussed in Section 3.3, the integration of the signal means the output amplitude is now sensitive to both amplitude and frequency modulations of the radiation intensity. These modulations were found to be 15% and 1%, respectively. Based on the simulations in Section 3.3 we find that the noise is dominated by the amplitude modulation.

An experiment was carried out using multiple high current bunches in an attempt to smooth the intensity modulation and increase the total intensity. The bursts of IR from each electron bunch integrate and the intensity modulations are averaged. The burst frequency was observed to be slightly different between bunches. Thus the intensity will exhibit low frequency beating that introduces noise into the spectra collected on the IR beamline. Due to the beating between multiple bunches, the summed intensity observed by the detector shows larger non-periodic intensity variations. The results displayed in Figure 4.3(b) show the irregularity of the bursts with increasing number of bunches. Although the intensity of CSR is greater for multiple bunches, the noise also increases with more bunches. If it were possible to couple the adjacent bunches so that the bursts occur in phase, the observed intensity would increase without adding to the noise. Long lived wakefields, or trapped high frequency modes in the vacuum chamber structures may induce such a coupling between the bunches. Although such a process was measured at ANKA [86], the coupling between bunches was found to be weak.

If strong coupling between bunches can be achieved it is possible to increase the intensity by ensuring that the bursts are synchronised. The results in Figure 4.3(b) suggest that coupling with three bunches may be possible since the intensity appears to peak simultaneously leading to larger amplitudes. Additional measurements using the diode detector were analysed (see Figure 4.4) and the bursts between bunches was shown to be independent. If coupling is present, it is very weak. These results show that only a single bunch can be used at a time to generate CSR in the bursting regime when a bolometer with a slow response is used. If a detector with a faster response (≥ 1 MHz) is used, more than a single bunch may be used. In the remainder of this thesis only single bunches are investigated.

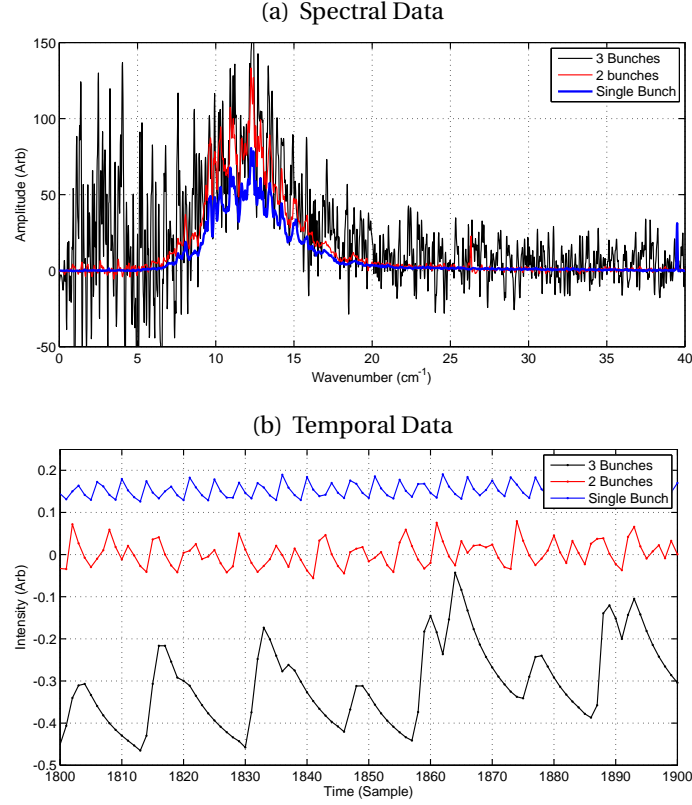


Figure 4.3: Spectral and temporal data is shown for single and multiple bunches. The spectral data show an increase in noise with increasing number of bunches. With a single bunch the spikes in the temporal data (spikes correspond to bursts of CSR) occur with a regular pattern. With two or more bunches the pattern of the spikes becomes irregular. The irregularity of the spikes indicate that the bursts from the individual bunches are uncorrelated.

4.1 Temporal Profile Analysis

Small oscillatory perturbations in the intensity during a single burst of CSR was observed in the data collected using the diode detector. Additional data were collected to observe if these perturbations were repeatable. For this experiment the storage ring was set up with the measured horizontal and vertical tunes of 0.292 and 0.219, horizontal and vertical chromaticity of 3 and 9, and with a synchrotron frequency of 8.2 kHz. The equivalent prediction from a lattice simulation gives $\eta_x = -0.69$ m, with sextupole magnet strengths of 12.2 m^{-3} (SFA) and -14.0 m^{-3} (SDA). The measured α_0 and α_1 values were 0.64×10^{-3} and 9.1×10^{-3} , respectively. The burst of CSR was measured with different sampling periods to ensure that the oscillatory perturbations are not an aliasing artefact. If the perturbations are caused by aliasing, a change in the sampling period will change the measured perturbation frequency.

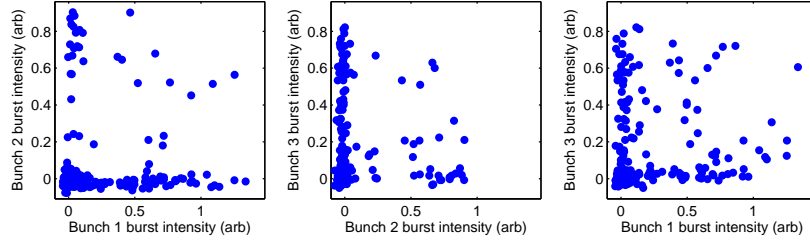


Figure 4.4: Diode detector output with three bunches in the storage ring spaced 2 buckets apart (4 ns). The acquisition is triggered by a timing signal synchronised with the revolution frequency of the circulating electron beam. If the bursts are highly coupled the data points will be clustered along the diagonal. Clustering along the axes indicates that the bursts are independent.

For a single electron bunch in the storage ring, the output from the diode detector is a single pulse with a width of around 1 ns. To ensure that the Nyquist criterion is met, the sampling period was kept below 0.5 ns. The spectral data from two data sets are shown in Figure 4.5 and exhibit the same spectral content with peaks at 130 kHz and 250 kHz. This result confirms that the modulations are genuine and repeatable.

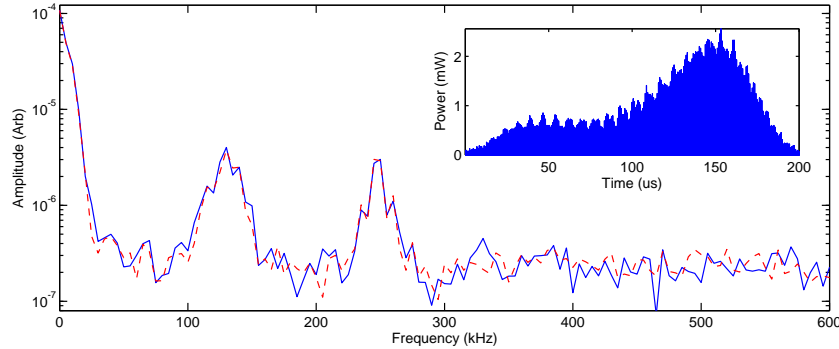


Figure 4.5: The power spectrum of the burst profile (inset shows the profile measured at 10.4 mA) at base band showing the frequency of the small oscillations. The sampling periods of the oscilloscope were 0.1 ns (blue) and 0.2 ms (red). The frequency peaks are 130 ± 5 kHz and 250 ± 5 kHz. These frequencies are observed as sidebands at the harmonics of the revolution frequency of 1.389 MHz up to ≈ 1 GHz (bandwidth of the detector). The synchrotron period is $1/8200$ Hz = $122 \mu\text{s}$.

A model that may explain the time structure of the bursts has been proposed by Stupakov and Heifets [87]. It is conjectured that CSR induced micro-bunching of the electron charge distribution results in the microwave instability. In this model the impedance is not dominated by wakefields from the vacuum chamber, rather it is determined by the impedance of the

emitted CSR [88]. This model was later improved upon by Cai [14, 89], by adding the effect of shielding from the vacuum chamber walls. In the latter model the threshold average current, I_b , is given by¹:

$$I_b = \left(\frac{6}{\pi}\right) \frac{\alpha_0 \gamma \delta^2 I_A}{a} \frac{c \sigma_t}{\sqrt{2\pi}}, \quad (4.1)$$

where $I_A = 17045$ A is the Alfvén current, a is the full gap of the vacuum chamber at the dipoles and I_b is the average single bunch current. Using ASLS values of $a = 0.032$ m and the measured bunch lengths in Figure 3.6, the threshold currents calculated from Equation 4.1, for $\eta_x = -0.70$ m and $\eta_x = -0.80$ m, are $I_b = 7.5$ mA and $I_b = 2.5$ mA, respectively. This is in broad agreement with the thresholds determined by solving the Haissinski equation at $I_{th} = 8.0$ mA and $I_{th} = 2.4$ mA. However, neither the Haissinski equation nor the CSR induced microbunching model describe the behaviour above the threshold, where the process becomes non-linear [90].

To model the longitudinal behaviour above threshold, Warnock and Ellison [61] and Venturini [1, 62] have numerically solved the non-linear Vlasov-Focke-Planck equation. In particular the simulations in Reference [1, 63] showed that CSR wakefields create micro-bunches in the charge distribution. The plots used in Reference [1, 63] have been reproduced in Figure 4.6.

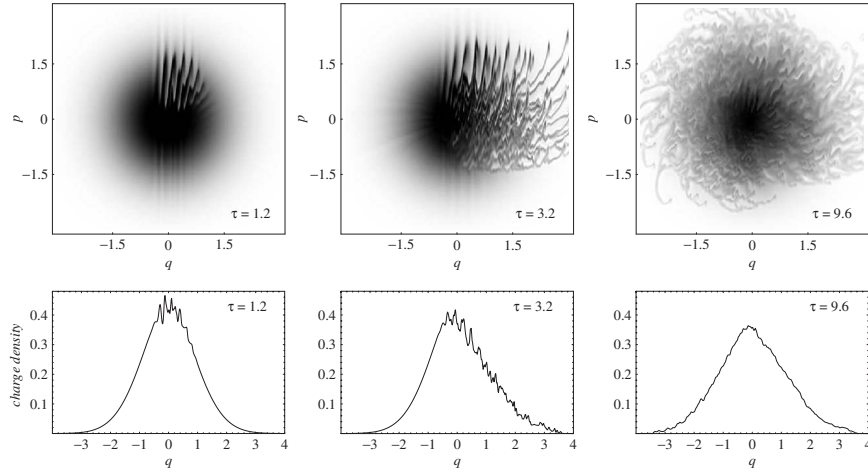


Figure 4.6: Simulation of CSR-induced microbunching. The Vlasov-Focke-Planck equation was used to model the longitudinal dynamics, with $p \equiv \delta$, $q \equiv \psi$ and $\tau = \omega_s t$. Courtesy of Warnock [1].

These simulations show a rapid onset of the micro-bunches over one quarter of a synchrotron period. After one and a half synchrotron periods,

¹This derivation assumes the bunch distribution is Gaussian and the relationship between the average current I_b and the peak current is given by $I = \sqrt{2\pi} \rho I_b / c \sigma_t$.

the micro-bunches disappear to form a relatively smooth distribution. The measured CSR burst profile in Figure 4.5 qualitatively agrees with the simulations in Reference [63] in terms of the growth and decay of the bursts. In addition, the formation and propagation of the filaments seen in the centre plot of Figure 4.6 may be the source of the small oscillations in the intensity.

A simple model is employed to simulate how the propagation of the filaments affect the observed CSR intensity. The boundary of the phase space distribution of particles is simulated by a circular ring of constant radius, r_0 . To mimic the filaments, the radius is modulated by a sinusoidal function $r(\phi, t) = r_0(1 + 0.01 \sin(n[\phi + \omega_s t]))$, where n is an integer number of periods and $\omega_s = 2\pi f_s$. The modulation creates bumps on the circular boundary function that are like teeth on a gear. These bumps rotate in phase space to simulate the propagation of the filaments in time. The position of these particles at the boundary are projected onto the real plane to get the longitudinal charge distribution. When the particles are projected onto the real plane, the rotation of the filaments in phase space is similar to two counter propagating waves. For a single frequency mode the charge distribution exhibits a standing wave oscillation at a frequency of $f_{osc} = nf_s$. This model is illustrated in Figure 4.7(a).

The diode detector has a sensitivity² of 2 V/W and cannot detect synchrotron radiation without the enhancement from coherence. Thus a modulation of the intensity measured by the detector is equivalent to a modulation in the enhancement gain factor. To replicate the expected modulation observed by the detector, the simulated charge distribution is used to calculate the gain factor³, $g(\lambda)$, as a function of time. The gain factor is calculated at three different wavelengths to illustrate the dependence of the measured intensity on the wavelength (see Figure 4.7(b)). The simulations show that the frequency of the intensity modulation does not depend on the wavelength.

The frequency spectrum of the simulated intensity is compared to the measured data in Figure 4.8. Although the first peak in the spectrum agrees with the data, the second peak does not. The second peak of the simulated data is a harmonic, occurring at exactly twice the frequency of the first peak. The measured data on the other hand has a second peak with a frequency that is less than the 2nd harmonic. In this simulation only a single longitudinal mode is excited. The intensity profile and the frequency spectrum show better agreement with the measured data if an adjacent mode is also excited. An illustration of what occurs when two modes are excited is shown in Figure 4.8(a). This simulation includes two excited modes and shows

²In comparison, the Si bolometer has a sensitivity of 6×10^5 V/W.

³The gain factor is given by: $g(\lambda) = \left| \int_{-\infty}^{+\infty} n(z) \exp i \frac{2\pi}{\lambda} z dz \right|^2$ (see Equation 1.3).

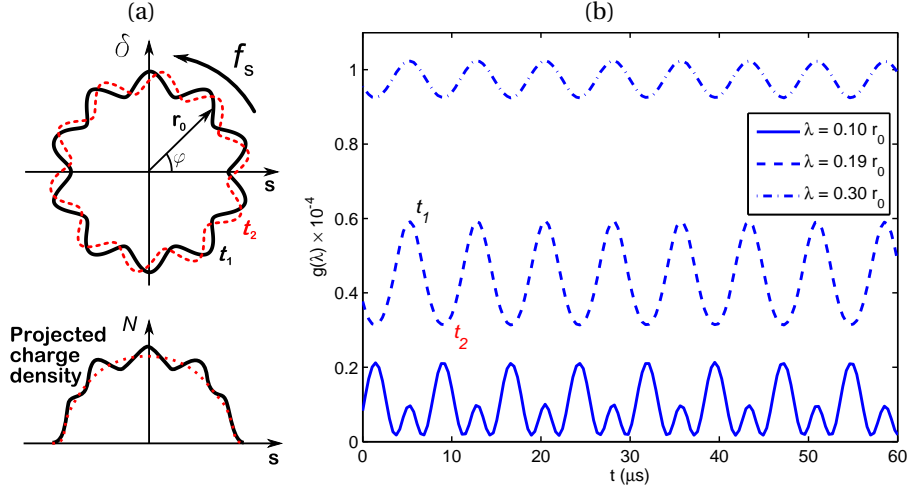


Figure 4.7: (a) Simulation of the filaments at the boundary and the projected charge density. The particles that form the filaments rotate in phase space at the synchrotron frequency, f_s , where the projected charge density displays standing wave oscillations at a frequency of $f_{osc} = n f_s$ where n is an integer number of the oscillations per synchrotron period. In this example $n = 16$. For even values of n the standing wave pattern in the charge density is symmetric about $s = 0$. For odd values of n , the standing wave is anti-symmetric. (b) Gain factor, $g(\lambda)$, calculated using the projected charge density from the simulation at three different wavelengths, λ . Depending on the wavelength the gain factor displays different temporal characteristics. However, the frequency stays the same and is not dependent on the wavelength.

non-sinusoidal modulations in the intensity as a result of the coupling between odd and even modes. Better agreement between the simulated and measured data indicates that at least two modes are excited.

The behaviour of the perturbation of the charge density, when excited by two modes, is described approximately by

$$\cos\left(\frac{n_1 + n_2}{2} [k_s s - \omega_s t]\right) \cos\left(\frac{n_1 - n_2}{2} [k_s s - \omega_s t]\right), \quad (4.2)$$

where $k_s = 2\pi/4r_0$ is the wavenumber of the perturbation, ω_s is the revolution frequency and $n_{1,2}$ is the mode number. At $t = 0$ the wavenumber of the perturbation about $s = 0$ is $k_{per} = k_s(n_1 + n_2)/2$ when $n_1 + n_2 \gg n_1 - n_2$. Defining the particles at the boundary ($r_0 = 3\sigma_t c$) the wavelength of the external perturbation is $\lambda_{per} = \frac{24\sigma_t c}{n_1 + n_2}$, and the wavelength is $\lambda = 0.57\sigma_t c$. Using the measured data in Figure 4.8, where $\sigma_t = 18$ ps, $n_1 = 15$ and $n_2 = 16$, the external perturbation is expected to be $\lambda_{per} = 4.2$ mm and the observation wavelength is $\lambda = 3.1$ mm (97 GHz). It is encouraging that the agreement between the simulated and measured results occurs at a wavelength corresponding to the peak response of the detector at 3.0 mm (99 GHz).

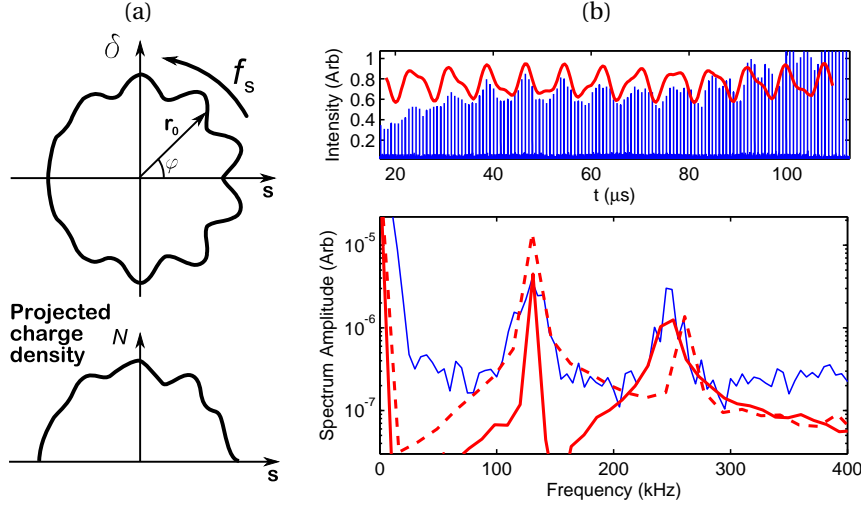


Figure 4.8: (a) Phase space simulation with coupled longitudinal modes ($n = 15$ and $n = 16$) showing the corresponding projected charge density. The phase space simulation shows qualitative agreement with the numerical simulations in Figure 4.6. (b) Simulations with a single longitudinal mode ($n = 16$; dashed red line) and coupled longitudinal modes ($n = 15$ and $n = 16$; solid red line). The spectrum of the simulated intensity using coupled longitudinal modes shows better agreement with the measured data (solid blue line). The modulation of the intensity for coupled modes is not sinusoidal and compares well with measured data from the diode detector. The synchrotron frequency is $f_s = 8200$ Hz and the simulated intensity was calculated at a wavelength of $0.19r_0$.

The calculated perturbation wavelength of 4.2 mm is close to the vacuum chamber cut-off $\lambda_c = 4.1$ mm⁴. The results suggest that the lowest excited mode corresponds to a perturbation that is at the vacuum chamber cut-off wavelength. To verify this observation, a measurement with a single bunch current of 9.3 mA at a synchrotron frequency of $f_s = 6450$ Hz⁵ was analysed. From the results we obtained $\lambda_{per} = 4.3$ mm \pm 0.2 mm, where $n_1 = 13$ and $n_2 = 14$, using an estimated bunch length of $\sigma_t = 16$ ps \pm 1 ps. These results suggest that the lowest observable longitudinal mode is limited by λ_c . Similar observations of the effects of vacuum chamber cut-off on CSR were also made at another light source [91].

One possible reason the lower modes are not observed is because the detector does not respond to radiation with wavelengths greater than 4 mm (75 GHz). A simulation of the filaments, using two modes below the lowest mode in the measured data, was carried out to test this conjecture. Spectral analysis of the simulated data clearly showed the lower modes with

⁴Emission of radiation is shielded by the vacuum chamber's conductive walls. The cut-off wavelength is given by: $\lambda_c = 2b^{3/2}\rho^{-1/2} = 2(0.032)^{3/2}(7.7)^{-1/2} = 4.1$ mm (see Equation 1.5).

⁵The horizontal dispersion was set to -0.80 m and $\alpha_0 = 0.33 \times 10^{-3}$.

perturbation wavelengths of $\lambda_{per} > 4$ mm. The oscillation in the gain was detectable at the wavelengths at which the detector is sensitive. Therefore the limitation imposed by the lowest mode is not due to the response of the detector. A detector with a different radiation response is required to verify our observations, and such experiments are the basis for future work.

In addition to exciting the two lowest modes, other modes were also observed. The analysis of modes at different beam currents showed that the number of excited modes are current dependent. The frequency spectrum was calculated by applying an FFT to a fitted envelope of the burst profile. An average of 20 samples was used to obtain the final spectrum, with the frequency axis of the spectrum normalised to the synchrotron frequency, i.e., $f_{osc}/f_s = f_n$. The results in Figure 4.9 show that increasing the current leads to

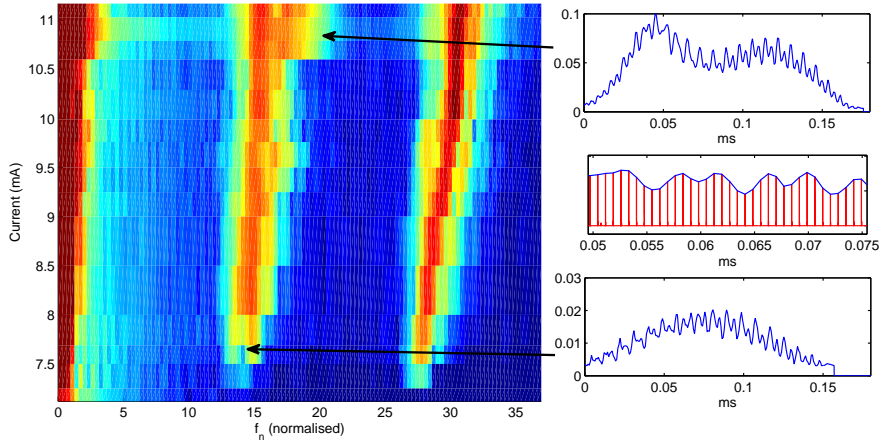


Figure 4.9: Power spectrum of the burst profile showing the excited longitudinal modes as a function of the current. The top and bottom plots on the right show the change in the overall burst profile with increasing current, while the middle plot shows how the envelope (blue) is calculated from the detector data after applying a threshold (red). Modes $n_1 = 14$ and $n_2 = 15$ are excited at 8 mA; modes $n_1 = 15$ and $n_2 = 16$ are excited at 10 mA. The synchrotron frequency is $f_s = 8050$ Hz.

an increase in the number of coupled modes. There is also a small increase in the lowest excited modes with current. This is to be expected if we assume that the lowest modes, n_1 and n_2 , are excited by an external perturbation of constant wavelength, $\lambda_{per} = \lambda_c$. The relationship, $\lambda_{per} = \frac{24\sigma_r c}{f_n}$, can be rearranged to give $f_n = \frac{24\sigma_r c}{\lambda_{per}}$. Therefore the increase in the bunch length with current will also lead to a linear increase in f_n with σ_r . Unfortunately the streak camera was still under repair and could not be used to measure the relationship between mode coupling and the bunch lengths.

Figure 4.9 shows the envelope function with the burst of CSR clearly

evident. The burst last for approximately one synchrotron period ($124 \mu s$) and small oscillatory perturbations are observed in the intensity. The data presented indicate that the perturbations are a result of the excitation of multiple longitudinal modes with wavelengths that are near the vacuum chamber cut-off, λ_c . This data also suggest that the perturbations are in phase with the peak of the burst. This is observed in Figure 4.10(a), where the temporal profile of the bursts are plotted as a function of beam current, with the peak intensity aligned relative to each other. In this figure the change

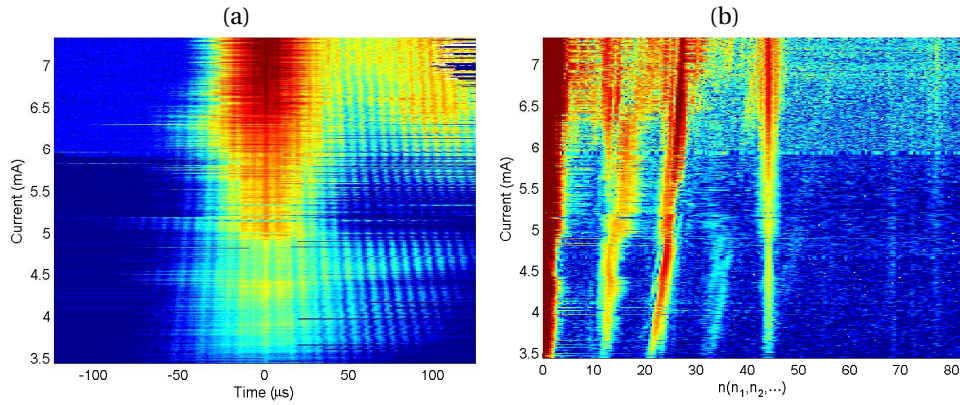


Figure 4.10: (a) Temporal profile of the burst as a function of beam current showing the phase relationship between the oscillatory perturbations and the longer burst of CSR. (b) Corresponding spectral plot showing the coupling of multiple modes at higher currents. The current independent mode 44 corresponds to a wavelength of 2.7 mm (110 GHz). Measurements at various f_s and at different beam currents all show the same mode. The detector appears to be responding to radiation with wavelengths shorter than its lower limit of 2.7 mm, corresponding to mode number 44. The synchrotron frequency is $f_s = 6070$ Hz, $\eta_x = -0.80$ and $\alpha_0 = 0.33 \times 10^{-3}$.

in the mode number being excited is clearly seen in the narrowing of the periodicity of the oscillations. The fact that the perturbations are symmetric about the peak of the burst and the pattern is repeatable suggests that the longitudinal modes giving rise to the perturbations are being coherently excited.

The mechanism that gives rise to the long burst of CSR is not clear from the data collected. However, we believe that the burst of CSR arises from longitudinal quadrupole-like oscillations driven by phase space asymmetries. The potential well distortion causes the Gaussian distribution to be skewed in the forward direction and has the effect of enhancing the intensity of radiation at shorter wavelengths due to the steeper edge. A small proportion of the electrons on the side of the steep edge will coherently radiate over a time interval of approximately one synchrotron period and collectively

move in phase space. This collective motion of electrons can be treated as a “bunchlet” moving in phase space. It is the behaviour of this bunchlet that gives rise to the long burst of CSR, in which the sum of the bunchlet and the main group of electrons create oscillations in the charge distribution. This is illustrated in Figure 4.11(a).

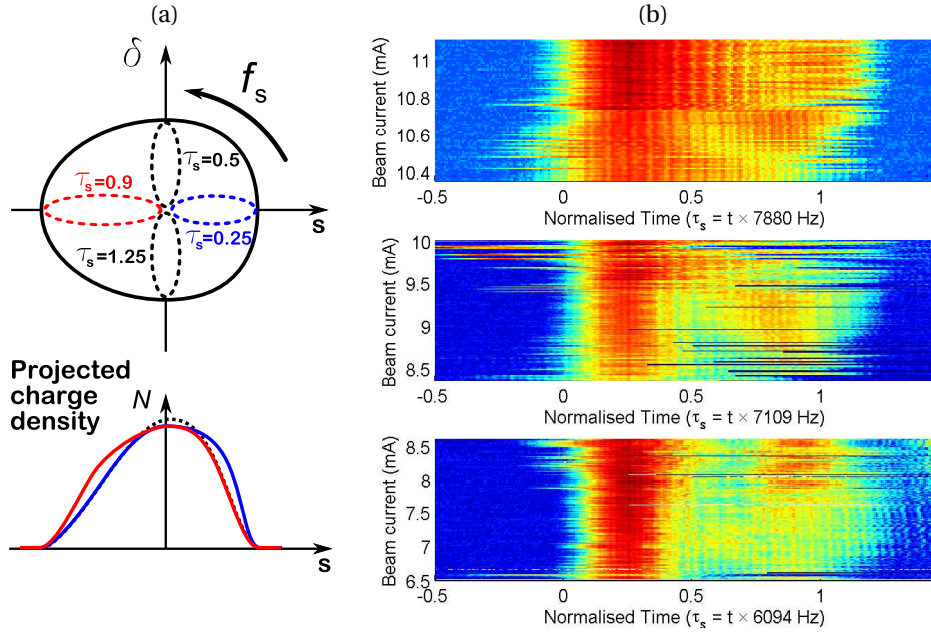


Figure 4.11: (a) Coherent motion of groups of electrons within the larger bunch of electrons. The coherent motion is described in normalised time, τ_s , in units of the synchrotron period $\tau_s = t f_s$. The coherent mode is like a dipole longitudinal mode with a frequency of $0.8 f_s$. (b) Measured bursts of CSR plotted in normalised time, τ_s , for three different configurations show similar characteristics in which the initial burst of CSR occurs at $\tau_s \approx 0.25$, followed by a second smaller burst at $\tau_s \approx 0.9$. The parameters for the three configurations are: (top) $\eta_x = -0.71$ m, $\alpha_0 = 0.60 \times 10^{-3}$, $\alpha_1 = 8.7 \times 10^{-3}$; (centre) $\eta_x = -0.75$ m, $\alpha_0 = 0.48 \times 10^{-3}$, $\alpha_1 = 8.0 \times 10^{-3}$; (bottom) $\eta_x = -0.80$ m, $\alpha_0 = 0.35 \times 10^{-3}$, $\alpha_1 = 6.2 \times 10^{-3}$.

Figure 4.11(b) shows measurements of the burst for three different configurations. The measurements are plotted in normalised time, $\tau_s = t f_s$, and show similar characteristics. In all three measurements, the first burst of CSR occurs within half a synchrotron period and is associated with the coherent motion of electrons to the front the electron bunch creating a steeper edge at $\tau_s = 0.25$. It is the steeper edge that gives rise to an increase in the enhancement in the radiation intensity. The coherent motion of the electrons continues along the bunch and at $\tau_s \approx 0.9$ it affects the tail of the bunch. The enhancement is reduced because the spectral content of the bunch density distribution does not change by very much at the tail. This dipole-like

coherent motion appears to occur at a frequency of $0.8f_s$. The shift of the dipole frequency from f_s can arise due to coherent frequency shifts of the longitudinal modes [55, 89, 92]. An analysis of the frequency shift based on an analytical model is not considered in this thesis and constitutes the basis for future investigations (see Chapter 6).

4.2 Beam Current Dependent Burst Frequencies

In the above analysis we observed that the burst of the CSR can arise from longitudinal asymmetries due to the potential well distortion (PWD). There is also another asymmetry that occurs along the δ axis, which is determined by the ratio of α_1 to α_0 . An analysis of measured data shows that the temporal profile of the burst of CSR, like those shown in Figure 4.11(b), is not significantly affected by the value of α_1 . Rather the value of both α_1 and the beam current, affects the frequency of the bursts.

The frequency of the bursts was measured using a spectrum analyser connected to a single stripline (see Appendix B.2 for details). An experiment measuring the burst frequency using a diode detector showed a direct correlation with measurements made with the spectrum analyser. Measuring the burst frequency with the spectrum analyser is a useful tool as access to synchrotron light for the diode detector is limited⁶.

The change in the burst frequency with beam current was measured. In this case the storage ring was configured with a synchrotron frequency of $f_s = 8.05$ kHz ($\eta_x = -0.70$ m) and chromaticities of 3 in the horizontal and 9 in the vertical. The measured values of $\alpha_{0,1}$ were $0.62 \times 10^{-3} \pm 0.04 \times 10^{-3}$ and $9.7 \times 10^{-3} \pm 0.9 \times 10^{-3}$, respectively. The results in Figure 4.12 show a non-linear dependence of the burst frequency with current and two distinct discontinuities in the burst frequency⁷. The first discontinuity at 9.5 mA appears where the 4th harmonic of the burst frequency resonates with the synchrotron frequency. The second discontinuity between 10.5 mA and 11.0 mA shows a change in the dynamics and is correlated with the appearance of a second smaller burst as shown in Figure 4.13. The burst frequency does not show a significant current dependence above 11.0 mA, rather there are further discontinuities in the burst frequency as the bursts change. Analysis

⁶Only two ports are available at the ASLS. One port is the optical diagnostic beamline, which is a poor transmitter of radiation and the second is the IR beamline. Both beamlines are dedicated for other uses and intercepting the synchrotron light for the IR detector affects normal operations.

⁷There was an initial concern that the noise from the amplifier was the cause of the discontinuities in the frequencies. To test this possibility, a spare amplifier with spurious sidebands at different frequencies was used (see Appendix C). The results showed that the frequencies at which the jumps occurred did not change. Therefore the spurious noise from the RF system is not the cause of the discontinuities in the frequencies.

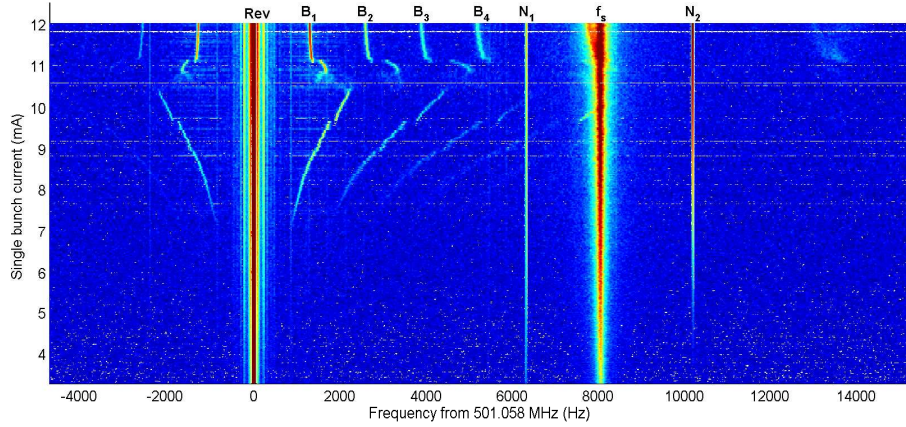


Figure 4.12: Beam motion measured with a real time spectrum analyser (SRA) showing the burst frequencies (B_1 to B_4) changing with current. The burst frequency shows a non-linear dependence on the beam current with a threshold current at 7.2 mA. The 8.05 kHz line (f_s) is the synchrotron frequency and the faint lines at 906, 1359, 1810, 2260, 2719 and 6300 Hz (N_1) are from the amplifier located just after the Master Oscillator. The source of the oscillation at 10.2 kHz (N_2) is unknown. “Rev” is a harmonic of the revolution frequency.

of the data shows that during these changes the burst frequency will jump erratically between two different values. In Figure 4.13 a lower value of α_0 was used because there are operational restrictions⁸ on increasing the single bunch current above 12.0 mA, which limits the capacity to excite the instability. The measurements in Figure 4.13 were made with the storage ring configured for a synchrotron frequency of $f_s = 7.10$ kHz ($\eta_x = -0.75$ m), and chromaticities of 0 in both the horizontal and the vertical. The measured values of $\alpha_{0,1}$ were $0.49 \times 10^{-3} \pm 0.04 \times 10^{-3}$ and $0.2 \times 10^{-3} \pm 0.7 \times 10^{-3}$, respectively. These results show three distinct burst regimes. The first regime at lower intensity is reasonably regular and lasts approximately 3/4 of a synchrotron period. This is just the onset of the quadrupole mode instability. The second regime is distinguished by the appearance of the second burst, which is expected of a quadrupole mode instability, i.e., a $n = 2$ mode. The third regime is distinguished by irregular changes in the temporal burst profile. This is probably due to the CSR-induced microbunching instability. At other values of α_0 , the temporal profile of the CSR bursts exhibit characteristics of the three regimes. The difference is in the bunch current at which the three regimes occur.

Although the intensity of the burst in the third regime is high, the con-

⁸With large single bunch currents the peak voltages generated in pickups on the storage ring, such as the BPM and striplines, can be very high. To protect the sensitive electronics attached to these pickups the peak current is limited to 12.0 mA.

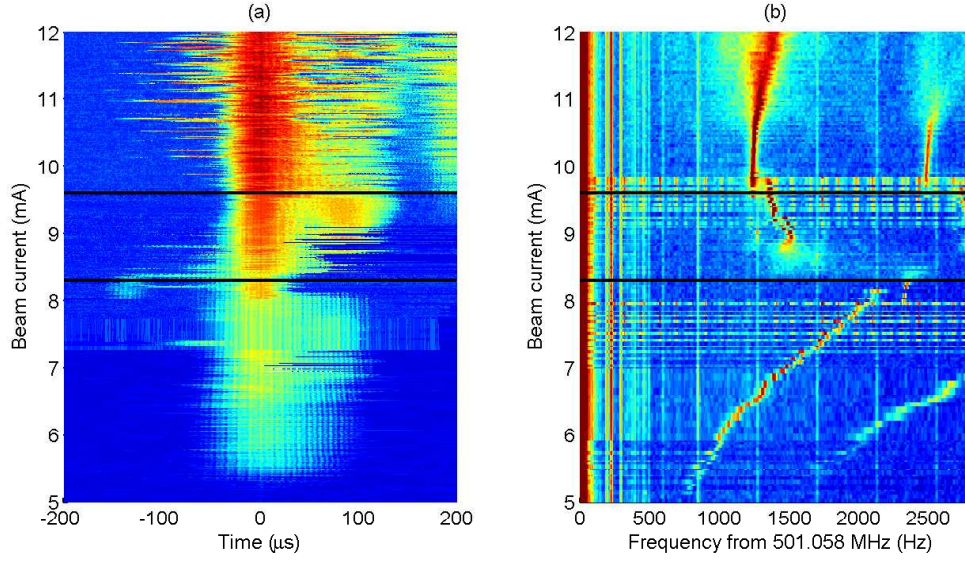


Figure 4.13: Temporal profile of CSR and the corresponding burst frequency as a function of the beam current. The results exhibit three distinct burst regimes. The first regime below 8.3 mA is current dependent and is predominantly driven by a dipole mode. The second regime between 8.3 mA and 9.6 mA transitions to a quadrupole mode, as indicated by the appearance of the second smaller burst. The third regime above 9.6 mA appears to be chaotic.

comitant change in intensity is not suitable for the ASLS IR beamline, which requires a constant intensity. In Chapter 5 we focus on the first and second regimes to identify the operational parameters that can be optimised for the ASLS IR beamline.

4.3 α_1 Dependent Burst Frequencies

The burst frequency is also affected by the value of α_1 , which can be understood in terms of the longitudinal head-tail instability [92]. The longitudinal head-tail instability is driven by asymmetries in phase space caused by a non-zero second order momentum compaction, α_1 . To illustrate this effect a surface plot of the Hamiltonian (Equation 2.25), is reproduced in Figure 4.14, which uses measured values of $\alpha_{0,1}$ and an estimate of ξ from experiments involving the burst frequencies. This plot shows that the phase space around the fixed points distorts as the separation in energy, $\Delta\delta_{fp} \approx \alpha_0/\alpha_1$, decreases.

Assuming that $\alpha_1 > 0$ and $\psi = 2.8$, there is a slightly shorter bunch if $\delta < 0$ and a slightly longer bunch if $\delta > 0$. This is illustrated in Figure 4.14(b), where the black dots highlight the effect. In Section 3.1 we saw that the wakefields, generated by the interaction of the electrons with the vacuum

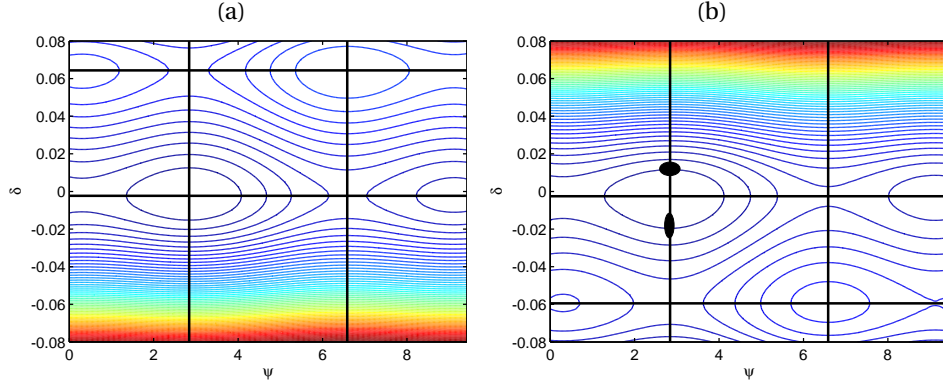


Figure 4.14: Surface plot of the Hamiltonian for $\alpha_0 = 6.2 \times 10^{-4}$ and $\xi = 1.5 \times 10^{-6}$ for two different values of $\alpha_1 = -1 \times 10^{-2}$ (a) and $\alpha_1 = +1 \times 10^{-2}$ (b). The contours represent the same energy values. The black dots in (b) highlight the difference in ψ if a group of electrons were to follow the path of the equipotential surface.

chamber, result in an energy loss due to the finite resistance of the vacuum chamber. Assuming a Gaussian distribution, Equation 3.7 shows that the energy loss is proportional to the inverse of the bunch length, i.e., $\Delta E \propto \sigma_t^{-1}$. Therefore a shorter bunch loses more energy compared to a longer bunch. In this example the bunch will lose energy when $\delta < 0$ and gain energy when $\delta > 0$, relative to the synchronous bunch ($\delta = 0$). This will result in an instability with growing synchrotron oscillations. The growth rate of the dipole mode instability is given by [92]:

$$\tau^{-1} = \frac{16\eta_1 N r_e}{3\eta_0 \gamma L_0 Z_0} \int_{-\infty}^{+\infty} \frac{\text{Re}Z^{\parallel}(\omega)}{a} J_1(a) J_2(a) d\omega, \quad (4.3)$$

where τ^{-1} is the growth/damping rate (positive/negative), $\eta_{0,1}$ is the zeroth and first order phase slip factors, N is the number of electrons, r_e is the classical electron radius, γ is the gamma factor, Z_0 is the free space impedance, $J_{1,2}$ are first and second order Bessel functions, $a = \omega\sigma_t/2$, and σ_t is the bunch length. For the ASLS $\eta_0 \approx -\alpha_0$ and $\eta_1 \approx \alpha_1$ when the electron energy is 3 GeV. Using the relation $\frac{N}{L_0} = \frac{I_b}{qc}$, and rearranging Equation 4.3, we get:

$$\frac{\tau^{-1}}{I_b} = \frac{16}{3} \frac{\alpha_1}{\alpha_0} \frac{r_e}{\gamma qc Z_0} \int_{-\infty}^{+\infty} \frac{\text{Re}Z^{\parallel}(\omega)}{a} J_1(a) J_2(a) d\omega. \quad (4.4)$$

To evaluate the integral in Equation 4.4, we use the SPEAR scaling law [93] to estimate the impedance. The peak impedance of 582 Ω has been measured previously (see Table 3.1) and the vacuum chamber cut-off⁹ frequency is used, $\omega_0 = 2\pi c/\lambda_c$. With these approximations, Equation 4.4 is evaluated

⁹See Equation 1.5.

and plotted in Figure 4.15 along with the measured burst rates normalised to the beam current. The vertical offset has also been removed to highlight the effect α_1 has on the burst frequencies. The results show gradients in the

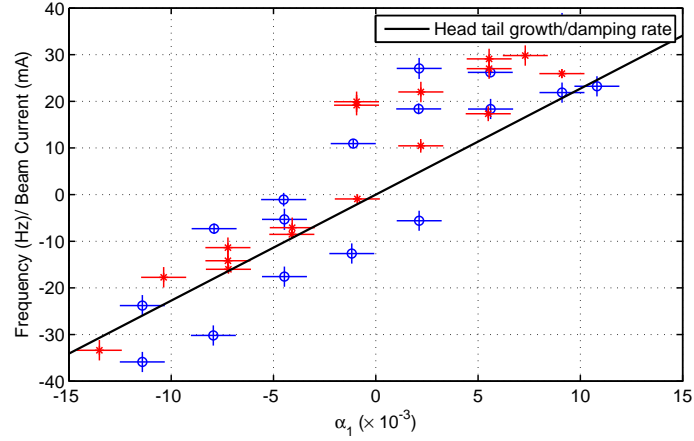


Figure 4.15: Burst frequencies as a function of the measured α_1 for the lattice. There is good qualitative agreement between the measured data and Equation 4.4, except for $\alpha_1 > 0$. In this configuration the burst frequency resonated with the synchrotron frequency causing a shift in the burst frequency. With different beam currents and different burst frequencies, the shift was not observed. Six different datasets were taken with two different transverse chromaticities of $\xi_{x,y} = (0, 0)$ (red '*' markers) and $\xi_{x,y} = (3, 9)$ (blue 'o' markers). The change in the transverse chromaticity was not seen to affect the burst frequency. Data were measured with beam currents of 8.9 mA, 9.0 mA, 10.6 mA, 11.0 mA and 11.1 mA, and $\alpha_0 = 0.62 \times 10^{-3}$.

measured data that are in good qualitative agreement with Equation 4.4, except for $\alpha_1 > 0$ which is possibly due to a harmonic of the burst frequency resonating with the synchrotron frequency, thereby causing a shift in the burst frequency. Subsequent measurements at different beam currents at different burst frequencies do not appear to show such shifts.

Positive values of α_1 with positive growth rates are unstable, while negative values of α_1 with negative growth rates are inherently stable. Despite the positive growth rates observed in Figure 4.15, the beam is still stable for positive values up to $\alpha_1 = 0.011$ because of radiation damping. For the ASLS lattice, the radiation damping rate is $\tau_{rad}^{-1} = 340$ Hz. During the measurements large horizontal synchrotron oscillations were observed for $\alpha_1 > 0.012$ at a beam current of 11.0 mA. At the threshold of $\alpha_1 = 0.011$ and $I_b = 11.0$ mA, the growth rate of the longitudinal head-tail instability is expected to be $\tau^{-1} = 25 \times 11 = 275$ Hz. Increasing the growth rate to values that exceed the radiation damping results in the appearance of the head-tail instability. This instability is characterised by the large synchrotron oscillations that were observed.

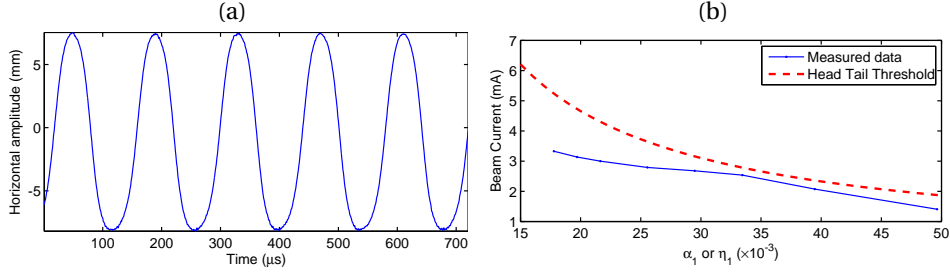


Figure 4.16: (a) As η_1 increases the beam current decreases because of the increasing strength of the head-tail instability. The stronger instability creates larger synchrotron oscillations that cause electrons to be removed as they encounter apertures in the vacuum chamber. (b) Current threshold created by the head-tail instability as a function of α_1 for measured data and the model prediction based on Equation 4.4. The data were measured for $\alpha_0 = 0.48 \times 10^{-3}$; we have assumed a bunch length of $\sigma_t = 12$ ps based on the current dependent bunch length data in Figure 3.6.

These large synchrotron oscillations, shown in Figure 4.16(a), cause the electrons at the periphery of the bunch to be intercepted by the vacuum chamber, thereby reducing the beam current. When the beam current decreases, the growth rate of the head-tail instability also decreases. This occurs until an equilibrium is reached where the growth rate equals the radiation damping. The threshold based on Equation 4.4 is shown in Figure 4.16(b) and compared to the measured current thresholds for increasing values of α_1 . The measured thresholds are in reasonable agreement with in that the measured values below the theoretically calculated threshold. The discrepancy is due to a sudden change in the value of α_1 that caused a large portion of the beam to be lost. It is plausible that if α_1 changes smoothly, the measured results would better follow the calculated thresholds.

We have shown that $\alpha_1 \neq 0$ only changes the frequency of the bursts by contributing to the growth or damping of the dipole mode instability. Therefore if α_1 is negative the dipole mode contribution to the overall instability will be damped, while a positive value of α_1 will reinforce the dipole mode. What this does to the burst rates is shown in Figure 4.17.

Previous measurements have shown that a well defined narrow peak in the burst frequency means there is a regular burst frequency and temporal profile. A broader peak in the burst frequency indicates either an irregular burst frequency or temporal profile. The results in Figure 4.17 show that α_1 has a direct effect on the current thresholds and burst frequency. If CSR is generated in the first and second burst regimes, a positive value of α_1 is preferred because of the lower beam current requirements and regular burst frequency (in the second regime). Negative value of α_1 results in more regular

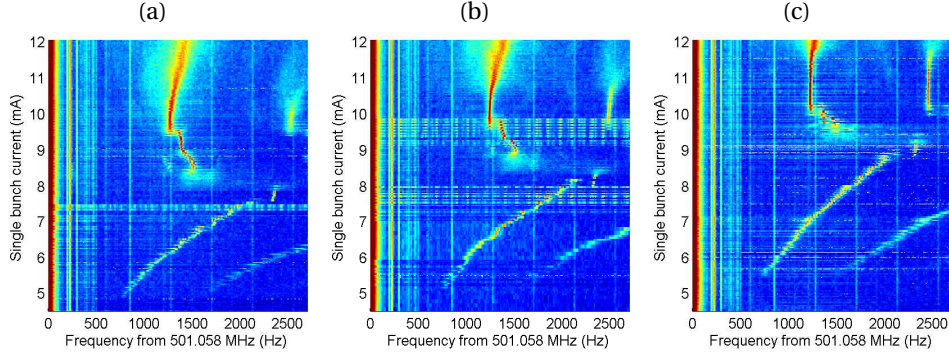


Figure 4.17: Comparison of the burst frequency with beam current for three different values of α_1 . (a) $\alpha_1 = 8.0$, (b) $\alpha_1 = 0.2$, and (c) $\alpha_1 = -15.6$. An increase in the damping of the dipole mode increases the current threshold. The storage ring parameters are: $f_s = 7100$ Hz, $\alpha_0 = 0.49 \times 10^{-3}$, $\eta_x = -0.75$ m, with chromaticities of 0 in both the horizontal and vertical planes.

bursts of CSR generated in the third regime. In Chapter 5 our investigation will focus on the bursts in the first and second regime, therefore only positive values of α_1 will be considered.

4.4 Summary

The temporal analysis of the data collected from the diode detector has given insight into the dynamics of the electron beam above the microwave instability threshold. This analysis provides evidence for the excitation of multiple longitudinal modes initiated by a burst of CSR. The analysis of the change in the burst frequency with bunch current identified three distinct regimes for the bursts of CSR. The first and second regimes predominantly involve the quadrupole mode ($n = 2$) that drives the emission of CSR. In these regimes a positive value of α_1 is preferable to reduce the current threshold. The third regime is characterised by an irregular burst of CSR and may indicate the onset of the microbunching instability. In the third regime a negative value of α_1 is preferred, since it improves the regularity of the burst of CSR. Studies relating to the third regime will be discussed in Chapter 6.

The choices of α_1 for the bursting emission of CSR is different to operating at very low values of α_0 for stable emission of CSR, where α_1 needs to be kept close to zero. In the next Chapter a method of determining an optimal configuration for the ASLS IR beamline will be described and the results of measurements on the IR beamline will be presented.

Optimising Bursts of CSR for the IR Beamline

Exploiting bursts of CSR as an enhanced source of Far-IR radiation for spectroscopy requires the frequency and integrated intensity of the bursts to be constant over a period of minutes. The stability of the burst frequency and integrated intensity was investigated in Chapter 4, where a diode detector and spectrum analyser was used to measure the temporal and spectral profile. In this chapter we use such temporal and spectral information to find an optimal working configuration for the stable generation of enhanced Far-IR radiation. The focus will be on finding a working configuration in the first and second burst regimes, where the frequency of the bursts of CSR is constant.

Measurements of the temporal profile were recorded for a storage ring with a synchrotron frequency of $f_s = 8.05$ kHz, $\eta_x = -0.7$ m and horizontal and vertical chromaticities of 3 and 9, respectively. The measured values of $\alpha_{0,1}$ were 0.62×10^{-3} and 3.6×10^{-3} . The results in Figure 5.1 show only the first and second burst regimes. It is clear from the temporal profile that at 9.2 mA and at 9.9 mA there is an overall increase in the damping rate. At these beam currents a harmonic of the burst frequency is resonant with the synchrotron frequency, creating additional damping through synchrotron oscillations. By fitting an exponential function to the temporal data, we can determine the change in the growth and damping rates (see Figure 5.2(a)).

A plot of the change in the integrated intensity in Figure 5.2(b) shows that the most stable emission region is between 9.3 mA and 10.6 mA. This region spans the region where the burst frequency couples with the synchrotron frequency. The intensity is doubled at a higher current (i.e., 12.0 mA) where the measured signal-to-noise ratio (SNR¹) is 26. This is nearly half the value at 10.0 mA, where the SNR is 43.9. The ASLS IR beamline requires that both the burst frequency and intensity be constant over longer periods of

¹The SNR is defined as: $A_{int}/\text{std}(A_{int})$, where A_{int} is the integrated amplitude of the signal from the IR detector measured at different times. 20 samples are used to calculate the mean and standard deviation at each beam current.

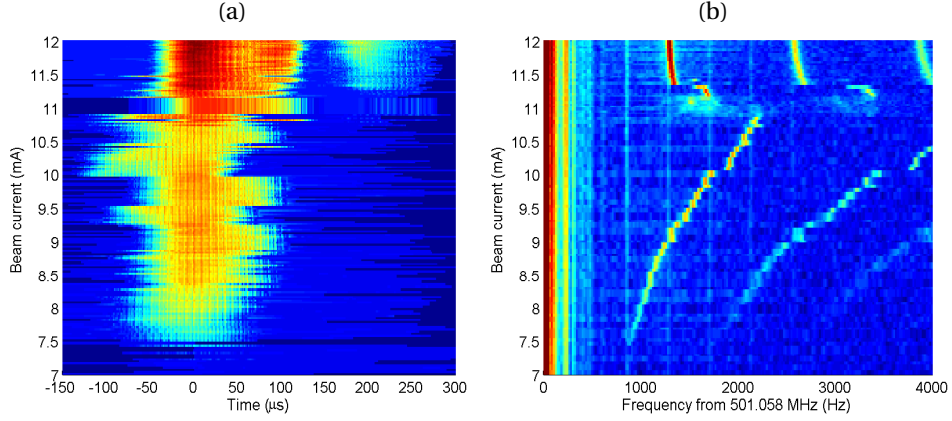


Figure 5.1: Changes in the burst profile are observed when the current in the single bunch is altered. There is a marked change in the profile at the discontinuities in the burst frequency, e.g., at 9.2 mA and 9.9 mA, where the 5th and 4th harmonics of the burst frequency resonate with the synchrotron frequency. Above 11.3 mA the profile has twice the power compared to 10.0 mA.

time because of the slow response time of the bolometer. Therefore our optimisation focuses on maximising the SNR rather than the value of the integrated radiation intensity.

One factor that might drive the SNR is the non-linearity of the RF bucket, which arises when $\alpha_1 \neq 0$. To ascertain whether this is the case, profiles were measured for different α_1 at two different chromaticities, i.e., $\xi_{x,y} = 3, 9$ and $\xi_{x,y} = 0, 0$. Measurements were taken with a single bunch at 9.0 mA. Analysis of the data in Figure 5.3 does not show a strong correlation between the burst rates and SNR with α_1 . When the data in Figure 5.3 are analysed against the burst frequency, the SNR peak occurs when the burst frequency is 1.53 ± 0.01 kHz and 1.50 ± 0.01 kHz (see Figures 5.3 (a) and (b), respectively).

To investigate the relationship between the SNR and the burst frequency, profiles for $\xi_{x,y} = 3, 9$ ($\alpha_1 = 9.7 \times 10^{-3}$) and $\xi_{x,y} = 0, 0$ ($\alpha_1 = 8.7 \times 10^{-3}$) were collected. The plot of the SNR as a function of the burst frequency is shown in Figure 5.4. These plots show that the SNR increases with increasing burst frequency. At the points where a harmonic of the burst frequency overlaps with the synchrotron frequency there is a drop in the SNR. A more significant observation occurs above the transition at around 2200 Hz. Although the current and integrated intensity continues to increase, the burst rate drops to 1300 Hz and the SNR drops to 30. This is the same SNR value as measured when the burst frequency is 1300 Hz at a lower beam current. These results indicate that there is a relationship between the SNR and the burst frequency.

Measurements of the SNR were also performed using the IR beamline's

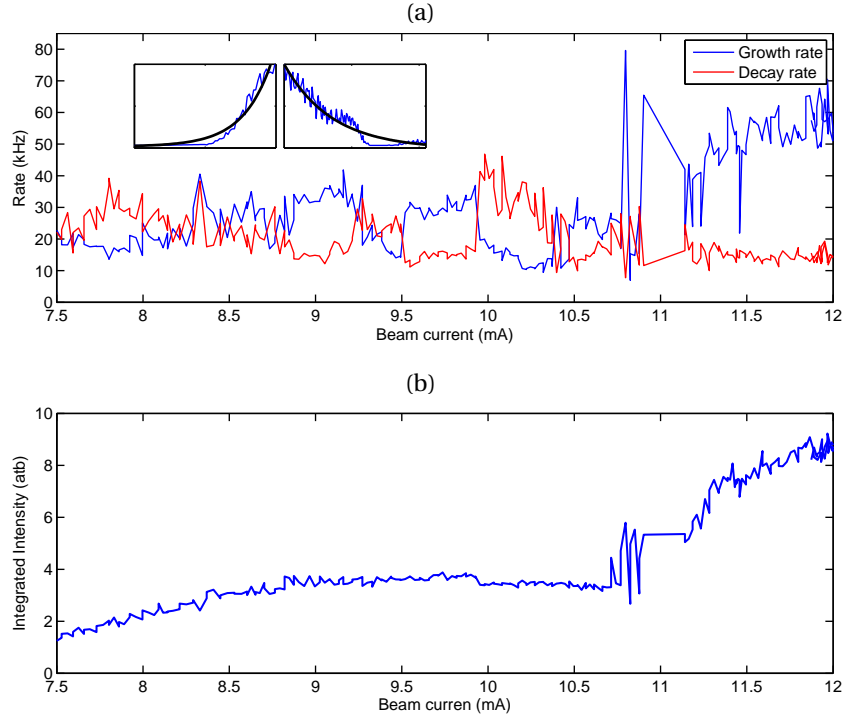


Figure 5.2: Growth and decay rates determined from fitting exponential functions to the profile data (as shown in the insets). At 9.2 mA and 9.9 mA, where the burst frequencies couple to the synchrotron frequency, an increase in the decay rate is matched by approximately the same decrease in the growth rate. Growth dominated bursts do not correlate with stable integrated intensities as seen in (b), where at 10.0 mA the SNR ≈ 44 and above 12.0 mA the SNR ≈ 26 .

bolometer to compare with data collected with the diode detector. This data is shown in red in Figure 5.4(a) and uses three spectra per data point². The SNR measured with the bolometer is determined from the average divided by the maximum spread³ of the spectral intensity of the three spectra at 13.0 cm^{-1} . The results from the bolometer are in general agreement with those obtained using the diode detector, providing evidence of a direct correlation between measurements made with the diode detector and the bolometer.

Before this detailed study of the stability of the burst frequency and integrated intensity, the configuration for the storage ring was determined by a “trial and error” approach. This operational configuration satisfied the requirements of the IR beamline for the bursts to be sufficiently consistent, with a good SNR and intensity enhancement greater than 100. The configuration used had chromaticities of $\xi_{x,y} = 3$ and 9 , $\alpha_0 = 6.4 \times 10^{-4}$ ($f_s = 8200 \text{ Hz}$), $\alpha_1 = 9.1 \times 10^{-3}$, and 10.5 mA in a single bunch. The current of 10.5 mA was

²Each spectra is calculated using 10 scans.

³The spread is determined from the maximum minus the minimum intensity.

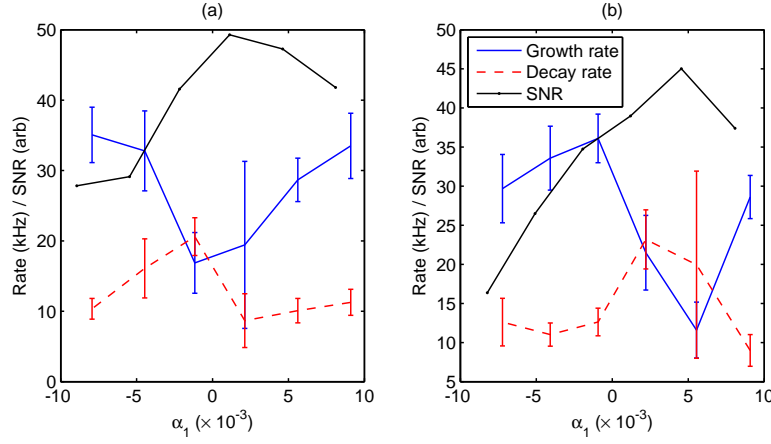


Figure 5.3: Burst rates and SNR as a function of α_1 for chromaticities $\xi_{x,y} = 3, 9$ (a) and $\xi_{x,y} = 0, 0$ (b). There is no obvious correlation between SNR and α_1 . However, the peaks correlate with burst frequency, so that the peak in (a) occurs at 1.53 ± 0.01 kHz and in (b) at 1.50 ± 0.01 kHz.

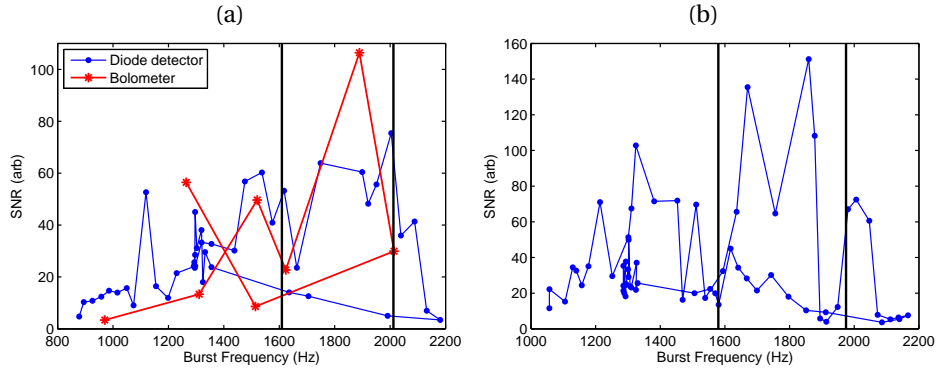


Figure 5.4: SNR calculated from profile measurements for different burst frequencies. (a) $\xi_{x,y} = 3, 9$ and $\alpha_1 = 9.7 \times 10^{-3}$. (b) $\xi_{x,y} = 0, 0$ and $\alpha_1 = 8.7 \times 10^{-3}$. Vertical lines represent $f_s/4$ and $f_s/5$. A trend to higher SNR values is observed when the 4th and 5th harmonics of the burst frequency resonate with the synchrotron frequency. Above the transition at 2200 Hz there is a step change to a lower frequency of 1300 Hz (see Figure 5.1). The SNR above and below the threshold is the same at the corresponding burst frequency. In (a), measurements were also carried out with the IR beamline's bolometer, which showed qualitative agreement with the diode detector measurements.

selected since it is at the threshold of the first of the burst regimes and has the most consistent burst frequency. The integrated intensity as a function of current in Figures 5.2 shows no current dependence, which is useful for longer term measurements on the beamline (i.e., up to 30 minutes for the acquisition of a single spectrum). During these scans the burst rate should not exhibit transitions in the burst regimes or changes in the burst intensity.

A series of measurements were made as the beam current decayed from 10.7 mA down to 10.0 mA. These results, plotted in Figure 5.5, show more noise between 10.2 mA and 10.7 mA, than between 10.0 mA and 10.2 mA. If we

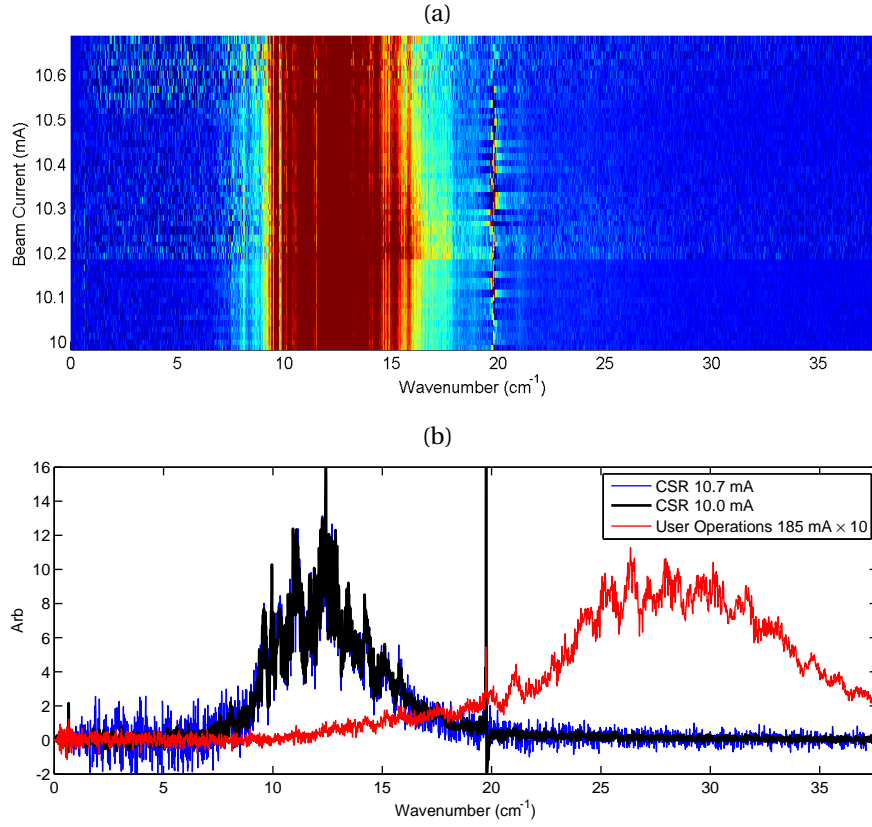


Figure 5.5: (a) Spectral plot showing the change in noise as a function of beam current. (b) A comparison of the emission from CSR at two different currents and the spectrum for normal operation with 185 mA in the storage ring. The spectrum corresponding to normal operation has been scaled by a factor 10 for comparison. The vertical lines at 19 cm^{-1} are caused by 50 Hz motion of the electron beam, which modulates the intensity of the photon beam and appears as spectral lines. The spectral resolution is 0.01 cm^{-1} .

refer to Figure 5.1 and Figure 5.4(a) we see that beam currents between 10.2 mA and 10.7 mA straddle the point where the burst frequency changes to a much lower frequency. This is where one would expect the intensity to be the most irregular. From 10.2 mA to 10.0 mA the burst frequency changes from 2100 Hz to 2000 Hz. In this region the burst frequency is stable with a SNR of 50.

A comparison between the spectra at 10.7 mA and 10.0 mA is shown in Figure 5.5(b), which clearly indicates the difference in the noise floor. At 10.7 mA the noise is double that at 10.0 mA, indicating that a tolerance on the beam current is needed if the noise is to be kept to a minimum. To

maintain the beam current to ± 0.2 mA over a 30 minute scan the lifetime of the electron beam, τ_b , will have to be at greater than 12 hours. The lifetime is defined as:

$$I(t) = I(0)e^{-\frac{t}{\tau_b}}, \quad (5.1)$$

where $I(0)$ is the initial beam current. With the low alpha configuration the lifetime is 17 hours and therefore the beam current will decay by 0.3 mA in 30 minutes, starting from an initial current of 10.0 mA. To maintain the burst frequency and ensure it stays in the optimal range, electrons will have to be injected every 30 minutes.

A plot of the peak intensity at 12.4 cm^{-1} is shown in Figure 5.6. This indicates that a harmonic of the burst frequency, resonant with the synchrotron frequency at 10.2 mA produces a spike in the intensity. Otherwise the data shows a flat response as a function of current. This agrees with measurements made with the diode detector (see Figure 5.2).

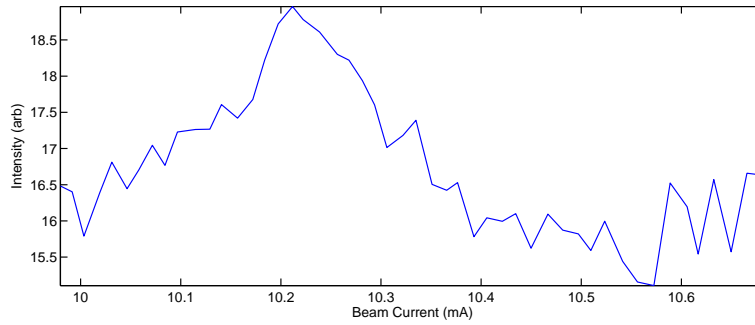


Figure 5.6: Spectral intensity at 12.4 cm^{-1} shows a peak at 10.2 mA but otherwise does not exhibit a positive gradient in the current. This qualitatively agrees with the results shown in Figure 5.2.

From these measurements we conclude that as long as the beam current is maintained at 10.0 ± 0.2 mA it will maximise the SNR. Enhancement from bursts of CSR in this configuration is around a factor of 100, compared to some previous observations, which showed gains of order 10^3 to 10^4 . At the initial stages it was possible to get the large enhancements; however, the noise and fluctuations in the intensity from one spectrum to the next were too great (low SNR). With lower SNR values, more measurements have to be made and averaged, leading to greater acquisition times. Thus a decision was made to sacrifice gain for stability and less noise. This configuration was used for the acquisition of absorption spectra for a sample of nitrous oxide (N_2O).

5.1 Absorption Spectra for N₂O

Nitrous oxide (N₂O) has a well defined molecular model that predicts the spectral lines [94, 95]. In our experiments 25 data sets were taken with and without nitrous oxide in the sample cell at a frequency resolution of 0.025 cm⁻¹. The average spectrum with and without N₂O is shown in Figure 5.7(a). The peak at 19.7 cm⁻¹ corresponds to 50 Hz beam motion (see Figure 2.7).

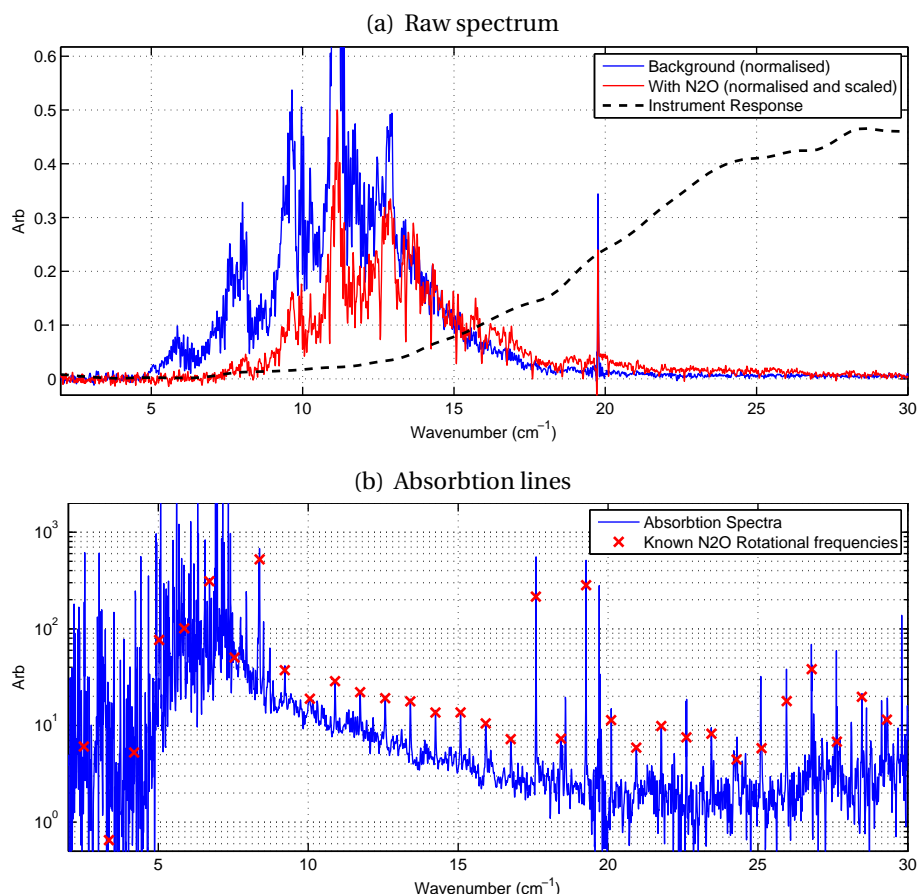


Figure 5.7: (a) Spectra using bursts of CSR with and without N₂O. The instrument's response is also plotted to highlight the region where enhancement occurs. The absorption lines seen in (b) are compared against known absorption lines for N₂O. A total of 25 spectra were collected and averaged. The spectral resolution is 0.025 cm⁻¹, with N₂O at a pressure of 0.4 Torr.

The observed exponential attenuation of the lower frequencies below 13 cm⁻¹ is due to an aperture restriction cutting off the longer wavelengths. During normal operation, either using synchrotron radiation or with an internal mercury lamp, the spectrum is hard to measure below 20 cm⁻¹. CSR has the benefit of extending the wavelength range, but more importantly the increased flux increases the detector sensitivity, thereby requiring a lower

sample densities. For example, to get equivalent spectra with an internal Hg source, the N₂O gas pressure was set to 2.0 Torr.

The absorption spectra in Figure 5.7(a) still shows some signal above 18 cm⁻¹ as a result of the incoherent radiation from the 10.0 mA bunch. This suggests that one can utilise incoherent radiation from multiple bunches that are below the instability threshold of 7.0 mA. This can be achieved by filling the storage ring with 300 bunches⁴, each with 0.6 mA and a single bunch with 10.0 mA. The 300 bunches with a sum current of 190.0 mA will radiate incoherently and assist in collecting spectra above 20 cm⁻¹, while the 10.0 mA bunch will be unstable and generate bursts of CSR that allow the acquisition of spectra below 20 cm⁻¹.

5.2 Optimising Bursts of CSR with Lower α_0 Values

The methods employed thus far to find a suitable configuration can also be used to explore the stability of the bursts of CSR at different values of α_0 . Here we present preliminary results aimed at improving the low alpha configuration.

The burst frequency as a function of bunch current was measured for $\alpha_0 = 0.46 \times 10^{-3}$ ($\eta_x = -0.75$) and $\alpha_0 = 0.36 \times 10^{-3}$ ($\eta_x = -0.80$). A plot of the burst frequencies is shown in Figure 5.8. Note the current thresholds at which the bursts are first observed are 7.2 mA ($\eta_x = -0.70$ m), 5.0 mA ($\eta_x = -0.75$ m) and 2.9 mA ($\eta_x = -0.80$ m). These agree reasonably well with the current threshold for the onset of non-equilibrium solutions to the Haissinski equation in Table 3.1 (i.e., 8.0 mA, 4.8 mA and 2.4 mA, respectively). These results show that by fitting R and L to measured results at low currents, it is possible to model the impedance of the storage ring and predict the threshold currents for the instability.

In all three cases above a threshold of around 2200 Hz there is a change in state in which the burst frequencies exhibit little or no current dependence. This state corresponds to the second and third burst regimes discussed in Chapter 4. This suggests that the threshold depends on the instability reaching a given growth rate. The burst rates also show jumps in the frequencies as the harmonic approaches f_s . This is observed in Figure 5.9 at 7.5 mA and 8.2 mA, which indicates that emission for $\alpha_0 = 0.62 \times 10^{-3}$ ($\eta_x = -0.70$) is the same at other α_0 values, and that similar islands of stable emission can be found. If this is true then the methods used in this thesis can be exploited to search for configurations that give the most stable emission of CSR, while simultaneously maximising the output.

⁴A total of 360 bunches can be stored in the storage ring.

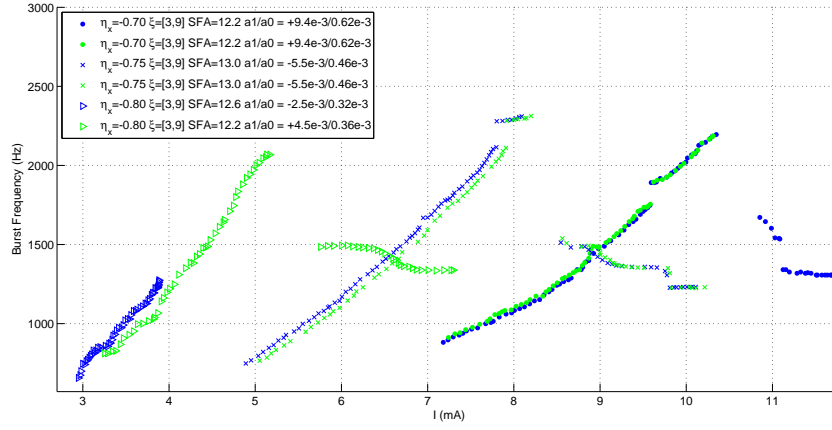


Figure 5.8: Increase in the burst frequency with single bunch current at lower α_0 values.

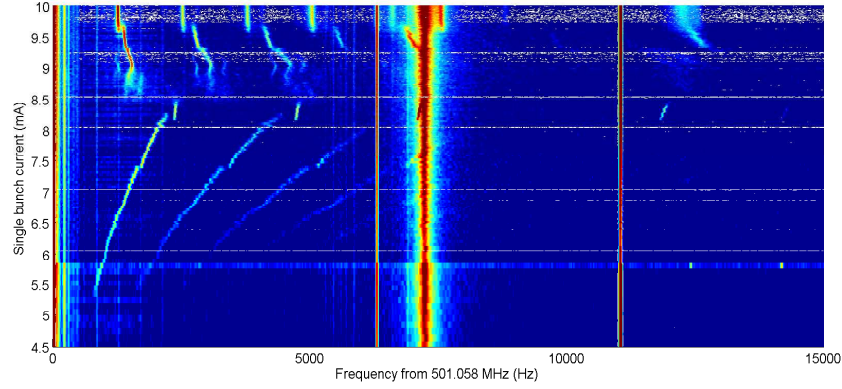


Figure 5.9: Burst frequency as a function of current from the spectrum analyser for $\alpha_0 = 0.46 \times 10^{-3}$ and $\eta_x = -0.75$ m.

The SNR analysis was also carried out on data collected for $\alpha_0 = 0.46 \times 10^{-3}$ ($\eta_x = -0.75$), along with measurements performed on the IR beamline. The purpose was to confirm the correlation between the output of the diode detector and the bolometer. These measurements were made at different beam currents and were achieved by using the injection fast kicker magnets to reduce the beam current slowly. To verify that the kicker magnets do not affect the results, additional measurements were carried out at points where all injection elements were turned off. The resulting data from the beamline consists of 5 samples measured at different beam currents. Each sample is an integrated value of the intensity from the detector over the period of the burst. The average of the samples is then divided by the spread of values in the samples to give the SNR. The results in Figure 5.10 show qualitative agreement with previous observations, indicating that the maximum SNR occurs when the burst rate is between 1700 Hz and 2000 Hz. Although not

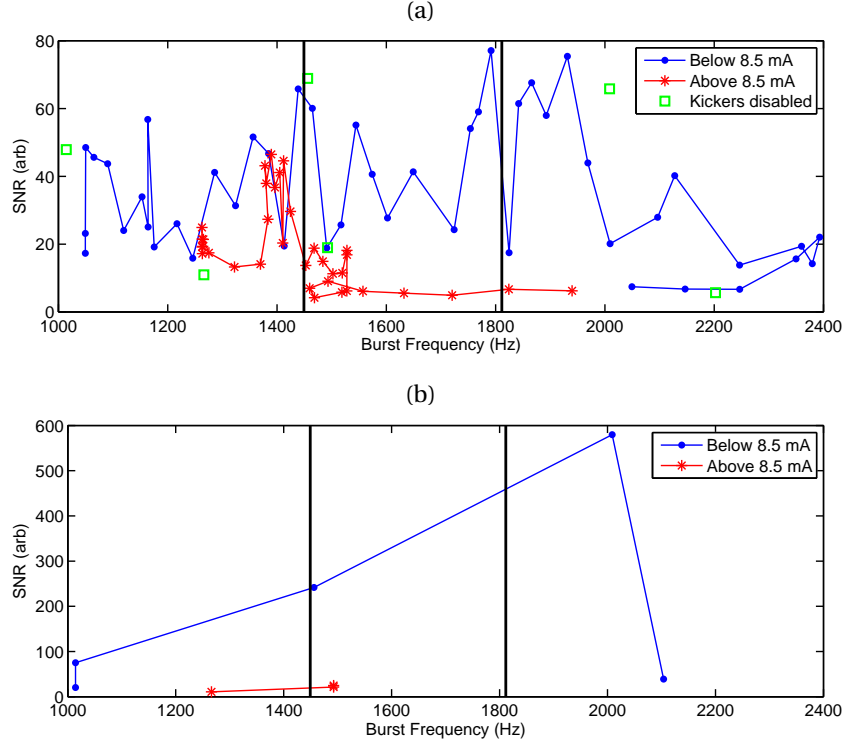


Figure 5.10: (a) SNR calculated using burst profile data measured by the IR detector at different beam currents. The storage ring injection kicker magnets were used to reduce the beam current slowly. To ensure the kickers do not distort the data, several measurements were made with the kickers disabled (square markers). (b) Measurements on the IR beamline were conducted at the same time, with 10 scans used to calculate the SNR. These measurements utilised the following parameters: $\alpha_0 = 0.46 \times 10^{-3}$ ($\eta_x = -0.75$ m), $\alpha_1 = 6.1 \times 10^{-3}$, chromaticity of $\xi_{x,y} = 4.2$ and 10.5 , and sextupole strengths of SFA = 12.2 m^{-3} and SDA = -14.0 m^{-3} .

shown here, the growth of the integrated intensity with beam current also displays similar behaviour, i.e., a plateau in the middle and rapid growth at higher currents. The only difference is in the threshold current and the rate of change with current. Measurements at other values of α_0 may allow a scaling relationship to be established, relating the functional form of the burst frequencies at different currents.

5.3 Summary

Before the methods in this thesis were developed, a trial and error approach was adopted to optimise the configuration of the lattice for the IR beamline. In this thesis we have evaluated various configurations in a systematic way and confirmed what had previously been determined in an ad hoc heuristic

manner. It is clear from the methodology developed in this thesis that the beam current needs to be maintained within a fixed range to maximise the SNR for measurements on the IR beamline. Configurations at different α_0 values can be exploited to optimise the CSR; however, we have only conducted preliminary investigations at $\alpha_0 = 0.46 \times 10^{-3}$ ($\eta_x = -0.75$ m), and much further work awaits completion.

Discussion and Future Directions

The creation of short electron bunches in a storage ring can be exploited to generate CSR in the Far-IR and to produce x-ray pulses that are ≈ 1 ps in duration. There are two methods that can be used to reduce the bunch length in Chasman-Green type lattices - negative dispersion and localised negative dispersion within the dipole magnet. For the generation of short x-ray pulses, localised negative dispersion is a more suitable method because the impact on the emittance is minimised. Therefore one can have a short electron bunch while maintaining a small transverse emittance and beam size. These are the optimal conditions for beamlines that require short x-ray pulses to measure temporal responses of objects on an atomic scale.

For the generation of CSR, it is not as clear which method would be more suitable. In both cases the reduction of α_0 makes the lattice inherently more sensitive to perturbations from the accelerator systems. For example, we have seen perturbations from the RF system appearing in the spectrum of the beam motion and large oscillations from the AC line frequency. It is probable that perturbations from the accelerator systems will restrict the achievable resolution of and control of α_0 , thereby limiting the creation of electron bunches that stably emit CSR in the Far-IR. One way to overcome this is to create a low alpha configuration at a beam energy of 1.5 GeV. To achieve a zero current bunch length of 1 ps at 3 GeV requires $\alpha_0 = 5 \times 10^{-6}$, which can only be achieved if the magnet power supplies and RF system are stable to 3×10^{-5} . This should be possible with the magnets; however, noise on the RF system can exceed these values. At 1.5 GeV a bunch length of 1 ps requires $\alpha_0 = 5 \times 10^{-5}$, which is an order of magnitude greater. The required stability of the magnet power supply and RF system are also an order of magnitude greater at 1×10^{-4} . The more relaxed constraints on the parameters at 1.5 GeV means the electron beam will be less sensitive to perturbations from the accelerator systems. It is expected that the next step in establishing a user configuration for the generation of CSR is to exploit a

low alpha mode at 1.5 GeV.

Keeping the electron bunch stable at relatively high bunch currents is difficult. Getting the bunch to excite an instability and emit bursts of CSR is in some sense relatively easy. In this thesis we wanted to investigate possible ways of utilising the bursts effectively. For this reason methods were developed to characterise the bursts of CSR and elucidate how the radiation depends on lattice parameters, such as $\alpha_{0,1}$ and the beam current. This was only made possible with the use of a fast detector. How the beamline reacts to the bursts of CSR depends on the operation of the IR beamline's instrumentation. For example, if the instrument can be made to operate in a stop-scan mode, where the detector can pause and integrate, the results will be less noisy. This is because it can integrate across many bursts of CSR and through averaging minimise the effect of the variation in burst frequency and intensity. Although it will take longer, this method of operation will give better results. Another method is to use some form of normalisation by using a second detector to measure the incoming radiation intensity. The incoming beam may be split into two branches, one through the sample and the other to a second detector. It should then be possible to normalise against the incoming radiation intensity fluctuations to minimise the effect of a fluctuating source intensity. Such a system would require a major redesign of the FT spectroscopy instrumentation used on the beamline and will require two detectors to be calibrated against each other.

Without modification to the beamline it was found that there are configurations where the bursts of CSR are reasonably stable. The measured SNR values with these configurations is only a factor of 2 below the SNR during normal operation. The trade off is in a reduction in the overall enhancement from a factor of 10,000 to a factor of 100. We have identified three different regimes that occur for the bursts of CSR. Only the first two regimes have been studied in this thesis and these are predominantly driven by dipole and quadrupole longitudinal modes. The third regime appears to be due to the onset of a microbunching instability, which is characterised by the chaotic nature of the bursts. The mathematical framework for describing the behaviour in the different regimes is an important next step and the subject of ongoing work.

The temporal data shows that the bursts of CSR in the first and second regimes excite longitudinal modes that have wavelengths shorter than the vacuum chamber cut-off. These excited modes appear as a modulation in the intensity of the CSR measured by the detector. Our analysis indicates some doubt about whether the bandwidth of the detector affects the results. Therefore additional detectors with different radiation responses are required and the measurements must be re-done to confirm the role of

the detector bandwidth. Another approach is to change the electron beam energy to alter the cut-off wavelength. If the wavelength of the lowest longitudinal mode changes with different beam energies, we can infer that the lowest longitudinal mode is correlated with the cut-off wavelength and is not an artefact of the detector bandwidth.

For many of the calculations reported in this thesis a measurement of the bunch length is required. Rather than relying on the synchrotron frequency to give the theoretical zero current bunch length, it would be useful to measure the bunch lengths in the three bursting regimes. These measurements can be used to demonstrate a relationship between the bunch lengths and the three bursting regimes, thereby elucidating the particular characteristics that define the bursting regimes. When the streak camera is operational (following repair) the bunch lengths will be measured as a function of bunch current for different values of α_0 .

In this thesis we have identified some general principles that are used to create bursts of CSR, which are stable in frequency and intensity. For example, when operating in the first or second regime, α_1 needs to be maximised without exciting the longitudinal instability. This is because the large dipole mode excited by the non-zero value of α_1 contributes to the emission of CSR. Furthermore, it is important to operate at a current that is not at a discontinuity in the burst frequency. These are a number of useful investigations that are the subject of future work. An immediate objective is to explore the third burst regime, which requires a negative value of α_1 to create a stable region to operate within. It is possible that negative values of α_0 will have a positive impact on the SNR.

In summary this thesis has demonstrated the feasibility of creating coherent synchrotron radiation by exciting single bunch instabilities. The work has shown that CSR can be usefully employed for IR spectroscopy and the outcomes have the potential to extend the utility of the IR beamline at the ASLS.

Appendices

Synchrotron Light Sources with Low- α Configurations



Low- α configurations have been used by light sources such as BESSY II and ANKA to reduce the bunch length for the generation of CSR. In Table A.1 the parameters of four light sources that operate in this mode are shown. This is only a small subset of light sources that offer users the option of operating in the low alpha configuration.

Table A.1: Parameters of light sources operating with Low Alpha configurations.

Parameter	MLS	BESSY II	DLS (Low Emitt.)	ANKA
E_0 [GeV]	0.63	1.70	3.00	1.30
L_0 [m]	48	240	562	110.4
f [MHz]	500	500	500	500
V_0 [kV]	< 500	1500	2000-3000	4×150 / 4×400
ν (H/V)	3.2 / 2.2	14.72 / 6.22	29.39 / 8.28	6.89 / 2.79 ($\alpha_0 = 4.6 \times 10^{-4}$)
ξ (H/V)	0 / 0	0 / 0	0.6 / -0.8	3.7 / 5.1 ($\alpha_0 = 4.6 \times 10^{-4}$)
ϵ [nmrad]	200	30	4.4	300 (130 - 400)
α_0	4×10^{-5}	3.5×10^{-5}	-1×10^{-5}	1.0×10^{-5} ($8.5 - 2.4 \times 10^{-4}$)
α_1	0	0	-2×10^{-5}	-2.7
α_2	0	< 0	4×10^{-3}	-190
Max $ \eta_x $ [m]	1.6	0.75	0.28	1.7
σ_t (normal) [ps]	13	13	10.0	43
σ_t (short) [ps]	2	2	2.4	3.8 (16 - 1)
τ_b [h]	12	30	10-20	8 (20-2)
Allocated time [days/year]	40	4 × 3	4	12
Far-IR CSR				
ρ	1.53	4.36	7.127	5.559
b [mm]	42	50	36.5	32
IR source	main	main	N/A	Edge
Burst/Stable CSR	both	both	N/A	both
Enhancement range [cm ⁻¹]	2-50	5-50	N/A	4-40

Storage Ring Beam Diagnostics

B.1 Beam Position Monitor (BPM)

A BPM consists of four capacitor probes arranged as shown in Figure B.1. There are 98 BPMs installed around the storage ring and these are the primary diagnostics for measuring the transverse position of the electron beam. The probes are connected to acquisition electronics [96] that digitises the RF signals and calculates the transverse position and intensity of the electron beam. The maximum sampling rate of the acquisition system is the revolution frequency of the storage ring at 1.39 MHz. Data sampled at the revolution frequency are commonly referred to as turn-by-turn data. Decimated data at rates of 22 kHz, 10 kHz and 10 Hz are also available.

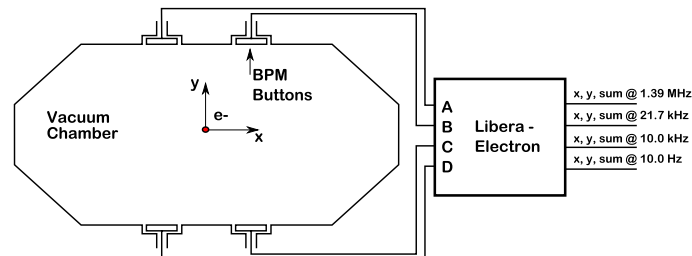


Figure B.1: Diagnostic setup used to digitize the signals from the BPM to calculate the transverse position and intensity of the electron beam. The position is sampled at a maximum rate of 1.39 MHz, with data also available at lower sampling rates.

B.2 Stripline BPM and a Real-time Spectrum Analyser

Another diagnostic was the Tektronix Real-Time Spectrum Analyser (RSA) RSA3308A, with a bandwidth from DC to 8 GHz, connected to a stripline

BPM. The stripline BPM consists of four metallic strips designed to have a length that is one quarter of the wavelength corresponding to the frequency of the RF system. At the ASLS the strips are 0.15 m long. The arrangement of the striplines are similar to the standard BPMs (see Appendix B.1).

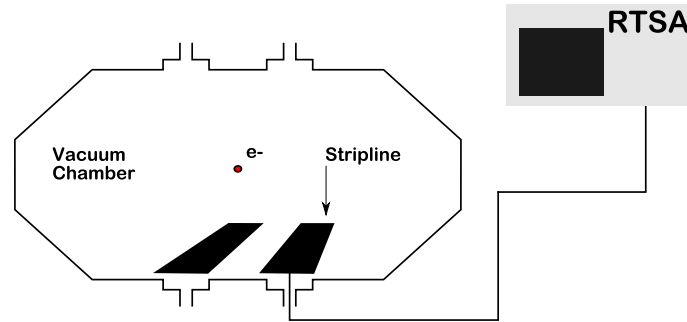


Figure B.2: Diagnostic setup used to measure the synchrotron oscillations on the electron beam. The stripline is a transmission line that couples to the beam and transmits the signal to a Tektronix Real-Time Spectrum Analyser (RSA).

B.3 Streak Camera: Chromatic Aberration

The streak camera uses refractive optics to focus the light from the storage ring onto a photocathode. The refractive optics introduces dispersive effects, such as chromatic aberrations, that increase the measured bunch length. An illustration of how chromatic aberrations contribute to the an increase in the measured bunch length is shown in Figure B.3.

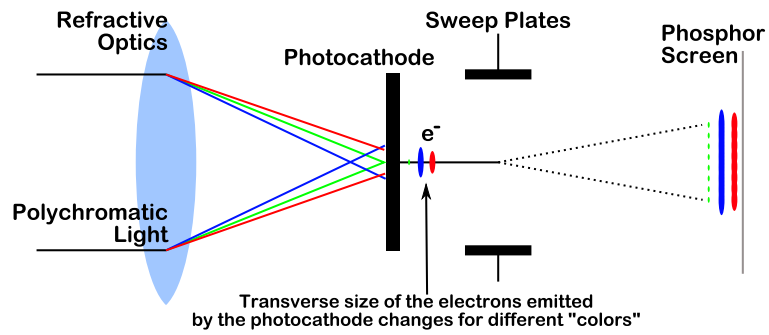


Figure B.3: Polychromatic light entering the input optics of the streak camera have a blurred focus due to chromatic aberrations. This is a result of differences in the refractive index for different frequencies of light. The ideal is a point-like source of electrons created by the photocathode that is “smeared” across the screen. The finite transverse size of the electrons created by the photocathode artificially elongates the “smeared” image on the screen. As a consequence the measured pulse duration appears to increase depending on the severity of the chromatic aberration.

Spurious Sidebands of Two Pre-amplifiers

C

To test if the spurious sidebands from the RF system were causing the “jumps” in the burst frequencies, a spare pre-amplifier was used, which has spurious sidebands at frequencies that are slightly different to the initial pre-amplifier. If the bursts are affected by noise from the pre-amplifier then changing over to the spare amplifier with different noise characteristics should have a noticeable effect on the behaviour of the burst frequencies. A comparison of the spurious sideband frequencies are shown in Figure C.1.

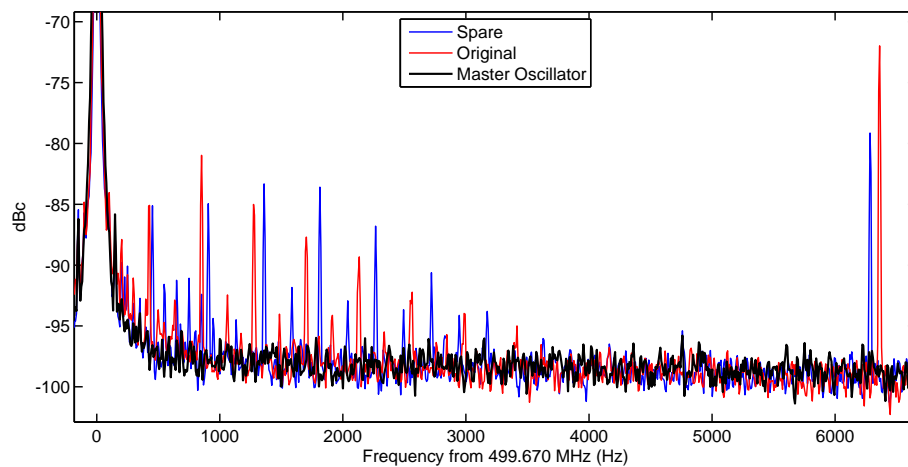


Figure C.1: A Master Oscillator signal is connected to two pre-amplifiers. The spectrum shows differences in the frequencies of the spurious sidebands of the original and second amplifier. The change in the frequency is at least 20 Hz, which is well above the resolution of the measurement at 8 Hz. Therefore, changes to the burst frequency that depend on the spurious sidebands will be measurable.

Conference Paper

D

LOW ALPHA CONFIGURATION FOR GENERATING SHORT BUNCHES

Y.-R. E. Tan, R. Dowd, M. Boland, D. Appadoo
Australian Synchrotron, Clayton, Australia

Abstract

Generating short bunches for time resolved studies or the generation of Coherent Synchrotron Radiation (CSR) has been done at many other light sources and is of increasing interest in the user community. Some light sources not designed with ps bunches can usually tune the lattice to reduce the bunch length without much difficulty, sometimes referred to as a Low Alpha mode. At the Australian light source a low alpha configuration has been investigated. The results looking into the “shaping” of the momentum compaction factor, beam stability and current limitations will be presented.

INTRODUCTION

A number of light sources, ANKA [1], BESSY [2], ELETTRA [3] and SPEAR3 [4], have reported CSR generation in the storage ring. As part of future developments at the AS we have started some investigations into the feasibility and stability of running the storage ring in a low- α configuration for the Far Infra-Red user community and beamlines that would like to do finely tuned time resolved experiments. This note will report on some of the initial results of our studies into a low- α configuration at the Australian Synchrotron (AS).

The AS storage ring is a 3 GeV Chassman-Green type lattice with three families of quadrupoles to control the two tunes and the dispersion. In such a lattice it is possible to control the momentum compaction factor, α_c , by adjusting the dispersion in the straights (to negative values) to reduce the integral, $\int \eta(s)/\rho(s)ds$, where η is the horizontal dispersion and ρ the bending radius. Table 1 below shows some of the relevant parameters for the different configurations.

Table 1: Lattice parameters for different configurations. The dispersion in the straight sections, η , controls α_1 . Further reductions are achieved by reducing the dispersion.

Parameter	$\eta = 0.1$ m	$\eta = -0.75$ m
α_c	2.11×10^{-3}	0.50×10^{-3}
f_s (kHz)	14.9	7.2
σ (ps/mm)	23 / 6.9	10 / 3.1

The machine was calibrated using LOCO [6] in Matlab. Further reduction of α_1 through the manipulation of the dispersion is achieved by using a model calculated inverted Jacobian with three families of quadrupoles and three parameters (two tunes and dispersion).

CSR is emitted when the length scale of the longitudinal bunch density is comparable to the critical length,

$\sigma_c = \lambda_c/2\pi = \sqrt{4b^3/\rho}/2\pi = 0.66$ mm, where $\rho = 7.7$ m is the bending radius and $b = 32$ mm the full vertical aperture of the AS storage ring vacuum chamber. CSR can be detected for bunch lengths up to $\sigma_s = \sigma_c \sqrt{\ln(N)} = 3.1$ mm [3]. Thus for dispersions less than -0.75 m CSR should be detectable. This however is only a rough guide and as observed at other light sources significant bursts of CSR can occur in longer bunches due to local density modulations. At the AS a sawtooth like pattern of emission was observed beginning around $\sigma = 4$ mm with 14 mA in a single bunch. The following sections will show some results from the Far-IR beamline, bunch length measurements as well as addressing some optimisation issues such as the manipulation of α_2 and orbit stability.

OBSERVATION OF CSR

Measurements were taken on the Far-IR & High Resolution beamline using a Bruker IFS125HR with a Si-B helium cooled bolometer. The measurements in Figure 1 show that the emission appears only between 10 and 20 wavenumbers at 9 mA in single bunch mode and is an increase in intensity of 5×10^4 at its peak. This was only with a modest decrease in α_1 to 5.8×10^{-4} (a factor of only 3.8). When we look at the raw data from the interfer-

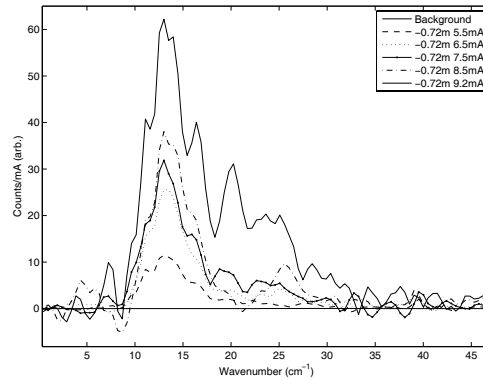


Figure 1: IR spectra showing emission between 10 and 20 wavenumbers with a lattice at a dispersion of -0.72 m instead of -0.75 m because of difficulties with injection at that time.

ometer a sawtooth pattern is observed and appears to grow with increasing current density. This is most likely the same phenomena observed at other light sources called the sawtooth instability and is associated with the quadrupole bunch phase oscillation mode [7]. The onset appears to be

>5.5 mA (see right pane of Figure 2) and correlates with the point at which the bunch length deviates from the potential well model in the top line in Figure 4.

To verify the time structure, the interferometer mirror was put in a static position and essentially used the bolometer as an IR intensity detector. The raw output from the Bolometer was put into a scope and the sawtooth pattern was observed to have a period of just over 2 ms as shown in the left pane in Figure 2. This is close to the damping time of the storage ring. It is believed that this instability causes longitudinal perturbations that give rise to burst of CSR (burst mode). Attempts to detect the quadrupole mode with the spectrum analyser, $2f_s$, were not successful, probably due to the current setup. As observed at other light

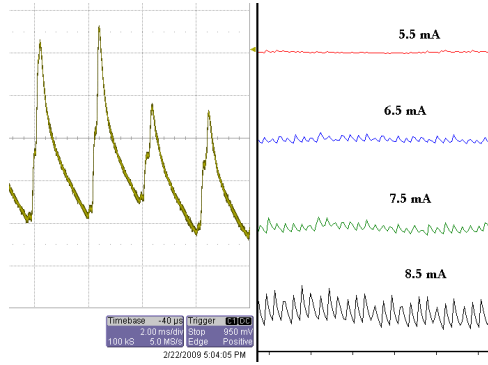


Figure 2: (Right) Data from the interferometer showing the sawtooth instability growing as the current is increased. (Left) IR mirror in a static position and we observed intensity fluctuations with a period of ≈ 2 ms in a sawtooth pattern.

sources the burst-mode CSR emission causes large intensity fluctuation that are not readily controllable/repeatable and is thus not useful for the beamline.

BUNCH LENGTH MEASUREMENTS

An Optronis streak camera was used to measure the longitudinal fluctuations and to confirm the sawtooth instability observed on the IR interferometer. The streak tube has dual sweeping plates allowing for a fast sweep to measure the ps bunch length and a slow sweep to monitor the bunch length over ms time scales. The primary sweep unit is a 250 MHz synchroscan unit that can sweep at 50, 25 and 15 ps per mm, so each sweep can separate adjacent bunches in the 500 MHz bunch train in the storage ring. The secondary sweep unit can sweep at 5 ms per mm in the perpendicular direction to the primary sweep unit, resulting in a time-time plot of the bunch length with time. The secondary sweep is triggered at 1 Hz and the full scale is 35.7 ms. The sawtooth instability was observed with streak camera, showing a semi-periodic 2ms bunch length fluctuations as shown in

Figure 3.

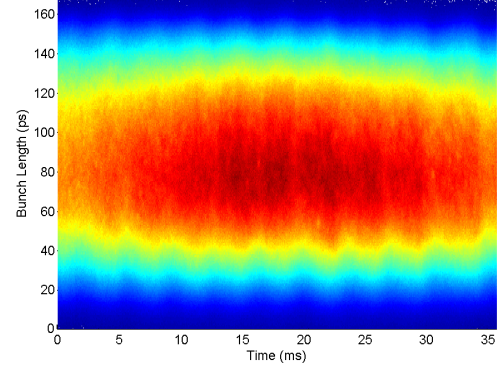


Figure 3: Streak camera measurements show bunch length oscillations with the same period as the sawtooth instability seen on the IR interferometer. $\eta = -0.75$ m with a single bunch current of 9.2 mA.

Bunch length measurements were made for different single bunch currents and for $\alpha_1 = 11.6 \times 10^{-4}$, 6.4×10^{-4} , 3.5×10^{-4} . The line plot in Figure 4 refer to the calculated and fitted theoretical bunch length dependence on the current, I , given by the Hassinski equation that describes the lengthening due to potential well distortions [8][9]. As expected Figure 4 show that at larger current densities the bunch starts to elongate and deviate from the potential well model as it approaches or exceeds the microwave threshold. In fitting the curves it seems that the ring inductances is much lower than expected at 25 nH (top line) and 15 nH (middle and bottom line) with the fixed resistance, R , set to 1600Ω (based on previous measurements as it is not expected to change with smaller bunches). The expected that the ring inductance was 70 nH given previous measurements in [8]. More points at lower currents are required to do proper fits, so further study would be required to understand these results.

MINIMISING α_2

Significant reduction in the bunch length also requires the reduction of second order momentum compaction factor, α_2 . This can be minimised by optimising the sextupoles. The AS storage ring has 4 families of sextupoles of which two are for chromatic correction and the remainder can be used to optimise α_2 . Experimental measurement of α_2 is determined by measuring the change in the synchrotron tune, f_s , as a function of the change in the RF frequency, f_{rf} according to the equation ([5],[4]),

$$\nu_s = \sqrt{\frac{hV_{rf} \cos \phi_s}{2\pi E/e}} \left(\alpha_1^2 - 4\alpha_2 \frac{\Delta f_{rf}}{f_{rf}} \right)^{1/4} \quad (1)$$

Figure 5 would indicate that the optimal setting for SFA

Beam Dynamics and Electromagnetic Fields

D01 - Beam Optics - Lattices, Correction Schemes, Transport

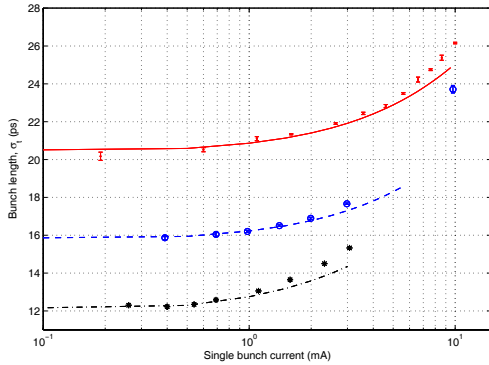


Figure 4: The line plots show the lengthening due to potential well distortions for a given fixed resistive, R , and inductive, L , value of the storage ring and different α .

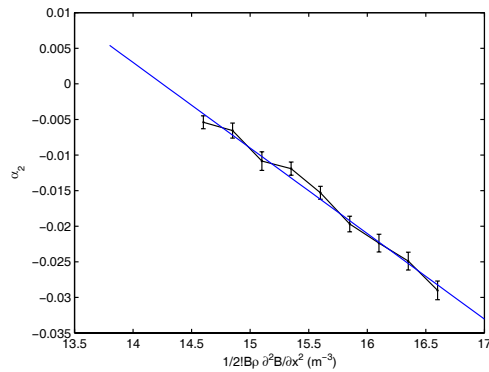


Figure 5: Measure of the change in the second order momentum compaction factor as a function of sextupole settings by measuring the change in Δf_s with $\Delta f/f_{rf}$. There are four families of sextupoles, one of which was varied, two others adjusted to keep the chromaticity constant around $\xi_x = 2$ and $\xi_y = 4$ and the last family kept constant.

that was varied is between 13.5 and 14.5 Amps. The smallest bunch length achieved so far was with $\eta = -0.92$ m with a measured $f_s = 1.3$ kHz which gives a theoretical $\alpha_1 \approx 2.11 \times 10^{-5}$ which is a 100 fold decrease from nominal. At the time we could not verify CSR emission as the beamline was not available. A problem at this configuration is that the machine's orbit stability is very sensitive to small energy fluctuations (from magnets) or phase shifts in the RF system.

ORBIT STABILITY

At very small values of α_1 and large absolute dispersions the lattice is very sensitive to changes in the beam energy. The smallest measured synchrotron frequency dur-

ing a test was around 1.3 kHz with $\alpha_1 \approx 2.11 \times 10^{-5}$.

The difference orbits show distinct dispersion orbits with peaks of $220 \mu\text{m}$ in the center of the arcs. With dispersions around 1.7 m this corresponds to peak to peak variations of $\Delta p/p = \delta_e = 1.3 \times 10^{-4}$. In RF terms this would only be changes of a few hertz which is certainly possible however noise in the RF system is harder to determine. A more likely source is from the dipole power supply whose DCCT readback also show a six sigma fluctuation of around 2.5×10^{-4} . The dominant noise is a clearly seen to be 50 Hz from the BPMs. The AS currently do not have a fast global orbit feedback system to correct for such orbit fluctuations, however even with such a system it would be unlikely that it could cope with such large deviations.

DISCUSSION

Some work has been done to understand the properties of the ring with smaller and smaller values of α_1 . More study would be required to understand the instabilities seen here. However it is clear from work done at other light sources that we would need to achieve steady state emission from sub-mm length bunches for the CSR to be usable. This can only be achieved at low bunch current densities and very small values of α_1 . To deal with the issue of noise another option would be to reduce the energy of the electron beam as there is a strong dependence of the bunch length with energy (approximately $\sigma \propto E^{3/2}$ [2]). By reducing the energy to 2 GeV it is possible to reduce σ by a factor of 2 and keep larger values of α so the ring is less sensitive to noise. This will be investigated.

ACKNOWLEDGMENTS

Discussions with Erhard Huttler from ANKA was very helpful and thanks for the assistance from the AS operators.

REFERENCES

- [1] A.-S. Muller, et. al., Far Infrared Coherent Synchrotron Edge Radiation At ANKA, PAC (2005)
- [2] G. Wustefeld, Short Bunches In Electron Storage Rings and Coherent Synchrotron Radiation, EPAC (2008)
- [3] E. Karantzoulis, et. al., Coherent THZ Radiation at ELETTRA, EPAC (2008)
- [4] X. Huang, J. Safranek, et. al., A. Low Alpha Mode for SPEAR3, PAC (2007)
- [5] A. Nadji, et. al., Quasi-Isochronous Experiments With The Super-ACO Storage Ring, NIM A, 378, 376-382 (1996)
- [6] J. Safranek, et. al., Matlab-based LOCO, EPAC (2002)
- [7] U. Arp, et. al., Spontaneous Coherent Microwave Emission and the Sawtooth Instability in a Compact Storage Ring, Phys. Rev. STAB, 4, 054401 (2001)
- [8] R. Dowd, et. al., Single Bunch Studies at the Australian Synchrotron, EPAC (2008)
- [9] J. Hassinski, Nuovo Cimento B, 18 (1973)

Beam Dynamics and Electromagnetic Fields

D01 - Beam Optics - Lattices, Correction Schemes, Transport

3713

Bibliography

- [1] M. Venturini, R. Warnock, R. Ruth, and J.A. Ellison. Coherent synchrotron radiation and bunch stability in a compact storage ring. *Phys. Rev. ST Accel. Beams*, 8:014202, 2005.
- [2] M. Venturini and R. Warnock. Bursts of coherent synchrotron radiation in electron storage rings: A dynamical model. *Phys. Rev. Lett.*, 89(22):224802, 2002.
- [3] F.R. Elder, A. M. Gurewitsch, R. V. Langmuir, and H. C. Pollock. Radiation from electrons in a synchrotron. *Phys. Rev.*, 71:829–830, 1947.
- [4] J.W. Boldeman and D. Einfeld. The physics design of the Australian synchrotron storage ring. *Nucl. Instrum. Meth. A*, 521(2-3):306 – 317, 2004.
- [5] R. Chasman, G. K. Green, and E. M. Rowe. Preliminary design of a dedicated synchrotron radiation facility. In *IEEE Trans. Nucl. Sci. (USA)*, volume ns-22, pages 1765 – 1767, 1975.
- [6] H. Wiedermann. *Particle Accelerator Physics*. Springer, 2007.
- [7] W. A. Barletta, J. Bisognano, J. N. Corlett, P. Emma, Z. Huang, K.-J. Kim, R. Lindberg, J. B. Murphy, G. R. Neil, D. C. Nguyen, C. Pellegrini, R. A. Rimmer, F. Sannibale, G. Stupakov, R. P. Walker, and A. A. Zholents. Free electron lasers: Present status and future challenges. *Nucl. Instrum. Meth. A*, 618(1-3):69 – 96, 2010.
- [8] P. G. O’Shea and H. P. Freund. Free-electron lasers: status and applications. *Science*, 292:1853 – 1858, 2001.
- [9] H.-D. Nuhn. From storage rings to free electron lasers for hard x-rays. *J. Phys.-Condens. Mat.*, 16(33):S3413, 2004.
- [10] J. S. Nodvick and D. S. Saxon. Suppression of coherent radiation by electrons in a synchrotron. *Phys. Rev.*, 96(1):180, 1954.
- [11] H. Wiedermann. *Particle Accelerator Physics I*, chapter 9.2, page 319. Springer, Berlin, 2nd edition, 2003.

- [12] R. A. Bosch. Shielding of infrared edge and synchrotron radiation. *Nucl. Instrum. Meth. A*, 482(3):789 – 798, 2002.
- [13] R. Warnock. Shielded Coherent Synchrotron Radiation and its Effect on Very Short Bunches. Technical Report SLAC-PUB-5375, SLAC, 1990.
- [14] Y. Cai. Theory of Microwave Instability and Coherent Synchrotron Radiation in Electron Storage Rings. In *Proceedings of the Int. Part. Accel. Conf.*, pages 3774–3778, 2011.
- [15] W. D. Duncan and G. P. Williams. Infrared synchrotron radiation from electron storage rings. *Appl. Opt.*, 22(18):2914–2923, 1983.
- [16] G. P. Williams. The initial scientific program at the NSLS infrared beamline. *Nucl. Instrum. Meth. A*, 291(1-2):8 – 12, 1990.
- [17] P. Dumas, G. D. Sockalingum, and J. Sul-Suso. Adding synchrotron radiation to infrared microspectroscopy: what's new in biomedical applications? *Trends in Biotechnology*, 25(1):40 – 44, 2007.
- [18] G. L. Carr. High-resolution microspectroscopy and sub-nanosecond time-resolved spectroscopy with the synchrotron infrared source. *Vib. Spectrosc.*, 19(1):53 – 60, 1999.
- [19] J. M. Chamberlain. Where optics meets electronics: recent progress in decreasing the terahertz gap. *Philos. T. Roy. Soc. A*, 362(1815):199–213, 2004.
- [20] M. Tonouchi. Cutting-edge terahertz technology. *Nature Photonics*, 1(2):97–105, 2007.
- [21] B. Ferguson and X.-C. Zhang. Materials for terahertz science and technology. *Nature Materials*, 1(1):26–33, 2002.
- [22] S. Biedron G. P. Gallerano. Overview of Terahertz Radiation Sources. In *Proceedings of the FEL Conference*, pages 216–221, 2004.
- [23] G. P. Williams. Filling the THz gap: high power sources and applications. *Rep. Prog. Phys.*, 69(2):301, 2006.
- [24] J. Yarwood, T. Shuttleworth, J.B. Hasted, and T. Nanba. A new radiation source for the infrared region. *Nature*, 312(5996):742 – 4, 1984.
- [25] E. Schweizer, J. Nagel, W. Braun, E. Lippert, and A.M. Bradshaw. Electron storage ring as a source of infrared radiation. *Nucl. Instrum. Meth.*, A246(1-3):163 – 164, 1985.

- [26] M. Abo-Bakr, J. Feikes, K. Holldack, P. Kuske, W. B. Peatman, U. Schade, G. Wüstefeld, and H.-W. Hübers. Brilliant, coherent Far-Infrared (THz) synchrotron radiation. *Phys. Rev. Lett.*, 90(9):094801, 2003.
- [27] J. Feikes, K. Holldack, P. Kuske, and G. Wüstefeld. Compressed electron bunches for THz Generation - Operating BESSY II in a dedicated low alpha mode. In *Proceedings of the Euro. Part. Accel. Conf.*, pages 2290–2292, 2004.
- [28] R. Müller, A. Hoehl, A. Serdyukov, G. Ulm, J. Feikes, M. Ries, and G. Wüstefeld. THz studies at a dedicated beamline at the MLS. In *Proceedings of the Int. Part. Accel. Conf.*, pages 2933–2935, 2011.
- [29] J. M. Byrd, Michael C. Martin, W. R. McKinney, D. V. Munson, H. Nishimura, D. S. Robin, F. Sannibale, R. D. Schlueter, W. G. Thur, J. Y. Jung, and W. Wan. Circe: a dedicated storage ring for coherent THz synchrotron radiation. *Infrared Phys. Techn.*, 45(5-6):325 – 330, 2004.
- [30] H. Bruck, J. P. Bardin, J. F. Gournay, J. L. Laclare, and G. Leleux. Limitation in short bunches production within electron storage rings. *Nuclear Science, IEEE Transactions on*, 20(3):822–824, 1973.
- [31] P. Kuske, A. Gaupp, G. Mühaupt, H.G. Hoberg, and W.D. Klotz. Isochronous operation of the electron storage ring BESSY. *Nucl. Instrum. Meth. A*, 237(1-2):289–290, 1985.
- [32] T. Nakazato, M. Oyamada, N. Niimura, S. Urasawa, O. Konno, A. Kagaya, R. Kato, T. Kamiyama, Y. Torizuka, T. Nanba, Y. Kondo, Y. Shibata, K. Ishi, T. Ohsaka, and M. Ikezawa. Observation of coherent synchrotron radiation. *Phys. Rev. Lett.*, 63(12):1245, 1989.
- [33] C. Pellegrini and D. Robin. Quasi-isochronous storage ring. *Nucl. Instrum. Meth. A*, 301(1):27–36, 1991.
- [34] D. Robin, E. Forest, C. Pellegrini, and A. Amiry. Quasi-isochronous storage rings. *Phys. Rev. E*, 48(3):2149, 1993.
- [35] L. Lin and C. E.T. Goncalves da Silva. Second order single particle dynamics in quasi-isochronous storage rings and its application to the LNLS-UVX ring. *Nucl. Instrum. Meth. A*, 329(1-2):9–15, 1993.
- [36] H. Hama, S. Takano, and G. Isoyama. Control of the bunch length on an electron storage ring. *Nucl. Instrum. Meth. A*, 329(1-2):29–36, 1993.

- [37] D. Robin, H. Hama, and A. Nadji. Experimental results on low alpha electron-storage rings. Technical Report LBL-37758, Lawrence Berkeley National Lab, September 1995.
- [38] A. Nadji, P. Brunelle, G. Flynn, M. P. Level, M. Sommer, and H. Zyngier. Quasi-isochronous experiments with the Super-ACO storage ring. *Nucl. Instrum. Meth. A*, 378(3):376–382, 1996.
- [39] A. S. Mueller, Y. L. Mathis, I. Birkel, B. Gasharova, C. J. Hirschmugl, E. Huttel, D. A. Moss, R. Rossmanith, and P. Wesolowski. Far infrared coherent synchrotron edge radiation at ANKA. *Synchrotron Radiation News*, 19(3):18–24, 2006.
- [40] X. Huang, J. Safranek, J. Corbett, Y. Nosochkov, J. Sebek, and A. Terebilo. Low alpha mode for SPEAR3. In *Proceedings of the Part. Accel. Conf.*, pages 1308–1310, 2007.
- [41] T.E. May, J.C. Bergstrom, L.O. Dallin, and D. Appadoo. Coherent synchrotron radiation measurements in the THz region at the CLS far infrared beamline. In *Infrared, Millimeter and Terahertz Waves, 2008. IRMMW-THz 2008. 33rd International Conference on*, pages 1–3, 2008.
- [42] R. Muller, A. Hoehl, R. Klein, G. Ulm, M. Abo-Bakr, J. Feikes, M.V. Hartrott, and G. Wüstefeld. First commissioning results in the IR/THz range at the electron storage ring metrology light source. In *Infrared, Millimeter and Terahertz Waves, 2008. IRMMW-THz 2008. 33rd International Conference on*, pages 1–2, 2008.
- [43] R. Müller, A. Hoehl, R. Klein, G. Ulm, M. Abo-Bakr, K. Bürkmann-Gehrlein, J. Feikes, M. Hartrott, J. S. Lee, J. Rahn, et al. Coherent synchrotron radiation at the metrology light source. In *Proceedings of the Euro. Part. Accel. Conf.*, pages 2058–2060, 2008.
- [44] I. P. S. Martin, G. Rehm, C. Thomas, and R. Bartolini. Experience with low-alpha lattices at the diamond light source. *Phys. Rev. ST Accel. Beams*, 14(4):040705, 2011.
- [45] Y. R. E. Tan, R. Dowd, M. Boland, and D. Appadoo. Low alpha configuration for generating short bunches. In *PAC*, pages 3711 – 3713, 2009.
- [46] J. Haissinski. Exact longitudinal equilibrium distribution of stored electrons in the presence of self-fields. *Nuovo Cimento B*, 18:72–82, 1973.

- [47] D. Boussard. Observation of microwave longitudinal instabilities in the CPS. Technical Report CERN-LAB-II-RF-INT-75-2, CERN, 1975.
- [48] S. Hansen and A. Hofmann. Blow-up of the bunch area. Technical Report ISR-GS-RF-AH-amb, CERN, 1976.
- [49] S. Asaoka, G. Isoyama, H. Mikuni, Y. Miyahara, and H. Nishimura. Slow fluctuation of synchrotron radiation and bunch lengthening in sor. *Nucl. Instrum. Meth.*, 215(3):493 – 500, 1983.
- [50] G. Rakowsky. Coherent synchrotron relaxation oscillation in an electron storage ring. In *Proceedings of the Part. Accel. Conf.*, pages 2377–2379, 1985.
- [51] U. Arp, G. T. Fraser, A. R. Hight Walker, T. B. Lucatorto, K. K. Lehmann, K. Harkay, N. Sereno, and K.-J. Kim. Spontaneous coherent microwave emission and the sawtooth instability in a compact storage ring. *Phys. Rev. ST Accel. Beams*, 4(5):054401, 2001.
- [52] B. Podobedov, G.L. Carr, S.L. Kramer, and J.B. Murphy. Origin of Longitudinal Density Modulation of Unstable Bunches in the NSLS VUV Ring. In *Proceedings of the Euro. Part. Accel. Conf.*, pages 1553–1555, 2002.
- [53] G. L. Carr, S. L. Kramer, J. B. Murphy, R. P. S. M. Lobo, and D. B. Tanner. Observation of coherent synchrotron radiation from the nsls vuv ring. *Nucl. Instrum. Meth. A*, 463(1-2):387 – 392, 2001.
- [54] Y. Shoji. Measurement of the time structure of a coherent synchrotron radiation burst in newsbar. *Infrared Phys. Tech.*, 51(5):367 – 370, 2008.
- [55] F. J. Sacherer. Bunch Lengthening and Microwave Instability. In *Proceedings of the Part. Accel. Conf.*, 1977.
- [56] K. Oide. A mechanism of longitudinal single-bunch instability in storage rings. In *Proceedings of the Part. Accel. Conf.*, pages 43 – 52, 1995.
- [57] K.L.F. Bane and K. Oide. Simulations of the the longitudinal instability in the new slc damping rings. In *Proceedings of the Part. Accel. Conf.*, volume 5, pages 3105 – 8, 1995.
- [58] A. Chao, B. Chen, and K. Oide. Weak microwave instability with potential well distortion and radial mode coupling. In *Proceedings of the Part. Accel. Conf.*, volume 5, pages 3040 – 3042, 1995.
- [59] A. Mosnier. Microwave instability in electron storage rings. *Nucl. Instrum. Meth. A*, 438(2):225 – 245, 1999.

- [60] G. Stupakov and S. Heifets. Beam instability and microbunching due to coherent synchrotron radiation. *Phys. Rev. ST Accel. Beams*, 5(5):054402, 2002.
- [61] R. Warnock and J. Ellison. A general method for propagation of the phase space distribution, with application to the saw-tooth instability. In *Proceedings of the 2nd ICFA Advanced Accelerator Workshop*, page 322, 2000.
- [62] M. Venturini and R. Warnock. Bursts of coherent synchrotron radiation in electron storage rings: A dynamical model. *Phys. Rev. Lett.*, 89:224802, 2002.
- [63] R. Warnock. Study of bunch instabilities by the nonlinear vlasov-fokker-planck equation. *Nucl. Instrum. Meth. A*, 561(2):186 – 194, 2006.
- [64] J. M. Byrd, W. P. Leemans, A. Loftsdottir, B. Marcellis, Michael C. Martin, W. R. McKinney, F. Sannibale, T. Scarvie, and C. Steier. Observation of broadband Self-Amplified spontaneous coherent terahertz synchrotron radiation in a storage ring. *Phys. Rev. Lett.*, 89(22):224801, 2002.
- [65] F. Sannibale, J. M. Byrd, Á. Loftsdóttir, M. Venturini, M. Abo-Bakr, J. Feikes, K. Holldack, P. Kuske, G. Wüstefeld, H.-W. Hübers, and R. Warnock. A model describing stable coherent synchrotron radiation in storage rings. *Phys. Rev. Lett.*, 93:094801, 2004.
- [66] J. Feikes, P. Kuske, R. Müller, and G. Wüstefeld. Orbit Stability in the Low Alpha Optics of the BESSY Light Source. In *Proceedings of EPAC*, pages 3308–3310, 2006.
- [67] G. Wüstefeld. Short Bunches in Electron Storage Rings and Coherent Synchrotron Radiation. In *Proceedings of the Euro. Part. Accel. Conf.*, pages 26–30, 2008.
- [68] H. Wiedermann. *Synchrotron Radiation in Storage Rings*, chapter 3.1.4, pages 187–190. World Scientific, Singapore, 2002.
- [69] H. Wiedermann. *Particle Accelerator Physics II*. Springer, Berlin, 2nd edition, 2003.
- [70] D. A. G. Deacon. Basic theory of the isochronous storage ring laser. *Phys Rep.*, 76(5):349 – 391, 1981.
- [71] J. B. Murphy and S. L. Kramer. First observation of simultaneous alpha buckets in a Quasi-Isochronous storage ring. *Phys. Rev. Lett.*, 84(24):5516–5519, 2000.

- [72] S. Heifets and A. Novokhatski. Coherent beam stability in the low momentum compaction lattice. *Phys. Rev. ST Accel. Beams*, 9(4), 2006.
- [73] A. Terebilo. Accelerator Modelling with Matlab Accelerator Toolbox. In *Proceedings of the 2001 Particle Accelerator Conference, Chicago*, pages 3203–3205, 2001.
- [74] E. Forest and R. D. Ruth. Fourth-order symplectic integration. *Physica D: Nonlinear Phenomena*, 43(1):105 – 117, 1990.
- [75] K. Y. Ng. *Head-Tail Instabilities*, chapter 12. World Scientific, Singapore, 1 edition, 2006.
- [76] J. Safranek. Experimental determination of storage ring optics using orbit response measurements. *Nucl. Instrum. Meth. A*, 388(1-2):27–36, 1997.
- [77] T. Obina and T. Mitsuhashi. Measurement Of Bunch Lengthening Effects Using A Streak Camera With Reflective Optics. In *Proceedings of DIPAC*, pages 256–258, 2007.
- [78] S. X. Fang, K. Oide, K. Yokoya, B. Chen, and J. Q. Wang. Microwave instabilities in electron rings with negative momentum compaction factor. In *Proceedings of the Part. Accel. Conf.*, volume 51, 1995.
- [79] H.P. Panopoulos, K.P. Wootton, M.J. Boland, and R.P. Rassool. Electron Beam Energy Measurement At The Australian Synchrotron Storage Ring. In *Proceedings of the Int. Part. Accel. Conf.*, pages 1138–1140, 2011.
- [80] F.-J. Decker. The Physical Way of Standardizing Magnets. Internal publication, SLAC-PUB-5483, 1991.
- [81] G. Wüstefeld, J. Feikes, M. v. Hatrott, M. Ries, A. Hoehl, R. Klein, R. Müller, A. Serdyukov, and G. Ulm. Coherent THz Measurements at the Metrology Light Source. In *Proceedings of the Int. Part. Accel. Conf.*, pages 2508–2510, 2010.
- [82] R. Dowd, M. J. Boland, G. S. LeBlanc, M. J. Spencer, and Y. R. E. Tan. Single bunch studies at the australian synchrotron. In *Proceedings of the Euro. Part. Accel. Conf.*, pages 1062–1064, 2008.
- [83] D. Creagh, J. McKinlay, and P. Dumas. The design of the infrared beam-line at the australian synchrotron. *Vibrational Spectroscopy*, 41(2):213 – 220, 2006. 6th Australian Conference on Vibrational Spectroscopy.

- [84] G. Eppeldauer, A. L. Migdall, and C. L. Cromer. Characterization of a high sensitivity composite silicon bolometer. *Metrologia*, 30:317 – 320, 1993.
- [85] G. Rehm, A. F. Morgan, R. Bartolini, I. P. Martin, and P. Karataev. Ultra-fast mm-wave detectors for observation of microbunching instabilities in the diamond storage ring. In *DIPAC 2009*, pages 369–371, 2009.
- [86] V. Judin, S. Hillenbrand, N. Hiller, A. Hofmann, E. Huttler, M. Klein, S. Marsching, A.S. Muller, N. Smale, K.G. Sonnad, P.F. Tavares, and H.W. Hubers. Observation of Bursting Behaviour Using Multiturn Measurements at ANKA. In *Proceedings of the Int. Part. Accel. Conf.*, pages 2526–2528, 2010.
- [87] G. Stupakov and S. Heifets. Beam instability and microbunching due to coherent synchrotron radiation. *Phys. Rev. ST Accel. Beams*, 5(5):054402, 2002.
- [88] J.B. Murphy, S. Krinsky, and R.L. Gluckstern. Longitudinal Wakefield for Synchrotron Radiation. In *Proceedings of the Part. Accel. Conf.*, pages 2980–2982, 1995.
- [89] Yunhai Cai. Linear theory of microwave instability in electron storage rings. *Phys. Rev. ST Accel. Beams*, 14:061002, 2011.
- [90] S. Heifets and G. Stupakov. Single-mode coherent synchrotron radiation instability. *Phys. Rev. ST Accel. Beams*, 6:064401, 2003.
- [91] S.L. Kramer and B. Podobedov. Coherent Microwave Synchrotron Radiation in the VUV Ring. In *Proceedings of the Euro. Part. Accel. Conf.*, pages 1523–1525, 2002.
- [92] B. Chen. *The longitudinal collective instabilities of nonlinear Hamiltonian systems in a circular accelerator*. PhD thesis, The University of Texas at Austin, 1995.
- [93] P. B. Wilson, R. Servranckx, A.P. Sabersky, J. Gareyte, G.E. Fischer, A. W. Chao, and M. H. R. Donald. Bunch Lengthening and Related Effects in SPEAR II. In *Proceedings of the Part. Accel. Conf.*, pages 1211–1214, 1977.
- [94] B.A. Andreev, A.V. Burenin, E.N. Karyakin, A.F. Krupnov, and S.M. Shapin. Submillimeter wave spectrum and molecular constants of N₂O. *J. Mol. Spectrosc.*, 62(2):125 – 148, 1976.

- [95] B. J. Drouin and F. W. Maiwald. Extended THz measurements of nitrous oxide, N₂O. *Journal of Molecular Spectroscopy*, 236(2):260 – 262, 2006.
- [96] A. Kosicek. Libera Electron Beam Position Processor. In *PAC*, page 4284, 2005.